SUPERCONDUCTING COPLANAR DELAY LINES

by

YI WANG

A thesis submitted to
The University of Birmingham
for the degree of
DOCTOR OF PHILOSOPHY

Electronic, Electrical and Computer Engineering
School of Engineering
The University of Birmingham

February 2005

Chapters 1 to 6 of

SUPERCONDUCTING COPLANAR DELAY LINES

by

YI WANG

A thesis submitted to
The University of Birmingham
for the degree of
DOCTOR OF PHILOSOPHY

Electronic, Electrical and Computer Engineering
School of Engineering
The University of Birmingham
February 2005

Abstract

Two 25 ns wideband HTS delay lines with a novel double-spiral meander line (DSML) structure are designed, fabricated and measured. One is based on the conventional coplanar waveguide (CPW), and the other based on a conductor-backed coplanar waveguide (CBCPW).

Systematic design work is presented in this thesis on the calculations of transmission-line parameters, the selection and optimisation of delay line patterns, and the modelling of the transitions and connections at the input/output. Simulations show that the DSML structure has better transmission efficiency over a wide frequency range than the conventional double-spiral line (DSL). The bandwidth and dispersion of such a meander structure are investigated.

The fabricated delay lines are first characterised as resonators with a fundamental mode at ~20 MHz. The surface resistances of the superconductors and the temperature- and power-dependent properties are investigated by measuring the Q-values of more than 1000 harmonics from 20 MHz to 20 GHz. Then, the delay lines are fully connected as they would be used in the application and measured thoroughly in both the frequency and time domain. The performance of the CBCPW delay line is the best ever demonstrated in terms of the widest resonance-free band (2 to 18 GHz), low insertion loss (0.06 dB/ns at 60 K and 10 GHz), small ripple (<1 dB up until 16 GHz), and small dispersion (< 2 ns in the variation of group delay between 2 and 18 GHz). This is the first coplanar delay line successfully demonstrated without using bonding-wires to join the in-plane grounds. The spurious reflecting elements in the DSML structure are identified by the time domain analyses. The results from this measurement are compared comprehensively with those from both resonance measurement and simulations.

to my mother because she never asked…

Acknowledgements

I would like to express my sincere gratitude to my supervisors, Prof. Mike Lancaster and Dr. Frederick Huang for their enlightening ideas, patient guidance, constant encouragement and support during the work toward my PhD. I benefit so much from the effective and efficient team work in the HTS delay-line project. Especially, my co-operation with Dr. H. T. Su has been so enjoyable and helpful.

It has been a great honor to work together with all my colleagues in Emerging Device Technology Research Centre. Particularly, I would like to thank Dr. D. Huish for his assistance in the programming of computer-controlled measurements, D. Holdom and C. Ansell for their technical support in device fabrication, and Dr. T. Jackson for his help in equipment and measurement skills. I am also grateful for my friends and colleagues, Dr. W. F. Hu, Dr. J. F. Zhou, G. Y. Zhang, Q. Xu, and Y. Koutsonas for kindly sharing the thoughts and experiences in both research activities and life in UK. I also thank Dr. A. V. Velichko, Dr. H. T. Su, and Dr. Phe Suherman for their comments and corrections on this thesis.

My acknowledgement also goes to Prof. R. G. Humphreys in QINETIQ for the helpful discussions in the project, and Mr. Simon Pyatt of Particle Physics Silicon Laboratory in Birmingham University for his generous help in wire-bonding.

I appreciate the financial support from the UK Overseas Research Student (ORS) scholarship and the Engineering School scholarship of the University of Birmingham.

My special thanks go to my wife, Zhen Wang, for her love and encouragement. Her companion makes my time worthwhile. Last but not the least, I must thank my family and friends for the invaluable help and endless support.

Table of contents

List of symbols and abbreviations

Symbols:

C: capacitance
c_0: light velocity
d_c: centre-to-centre distance between two juxtaposed meander lines
h: substrate thickness
$\boldsymbol{J}$: current density
$K(k)$: complete elliptic integral of the first kind
L: inductance
l_c: coupled length in a pair of parallel lines
l_x: inter-line distance between parallel coupled lines
Q, Q_L, Q_0: quality factor, loaded Q, unloaded Q
R_f: surface resistance of a thin film
R_s: surface resistance of an infinitely thick material
s: slot width in a coplanar line
t: film/conductor thickness
$tan(\delta)$: dielectric loss tangent
w: strip width in a coplanar line
Z_0: characteristic impedance
α_c: attenuation due to the conductor loss
α_d: attenuation due to the dielectric loss
ε_{eff}: effective permittivity
ε_r: relative permittivity
λ_p: penetration depth
σ: conductivity
v_g: group velocity
v_p: phase velocity

Abbreviations:

BW: bandwidth
CPW: coplanar waveguide
CBCPW: conductor-backed coplanar waveguide
DSL: double-spiral line
DSML: double-spiral meander line
GF: geometric factor
HTS: high-temperature superconductor
LAO: $LaAlO_3$
YBCO: $YBa_2Cu_3O_{7-\delta}$

Chapter 1 Introduction

1.1 Delay line

In an electronic circuit, a delay line is used to delay an electromagnetic wave or signal by a specific time. Ideally, the output from a delay line should be a replica of the input.

Loss is one of the most important criteria for a delay line. It is mainly caused by the attenuation of the conducting and dielectric materials used in the transmission media. For a coaxial delay line (commonly adopted in current systems), in order to produce a long delay time of the order of a hundred nanoseconds and overcome the unacceptable insertion loss, low-noise amplifiers have to be inserted to compensate the transmission loss at regular intervals. These active components, however, unavoidably compromise the overall dynamic range of the delay line.

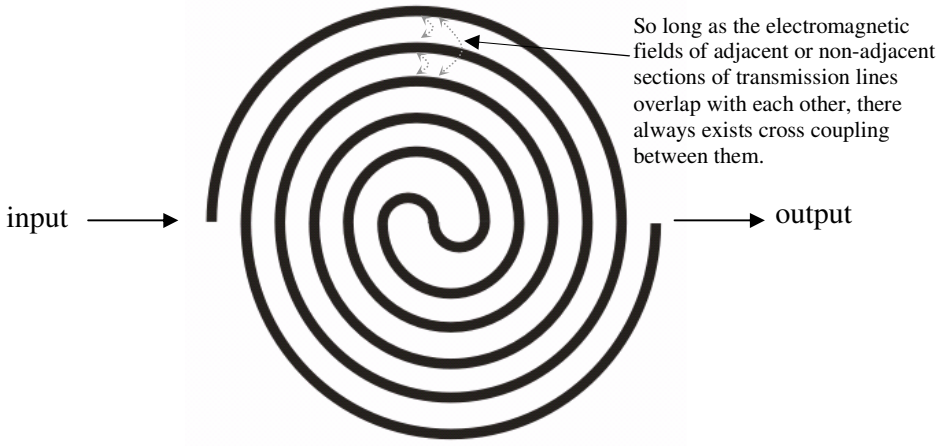

Figure 1.1 A microstrip double-spiral structure used in many delay lines.

Cross coupling occurs when different sections of a delay line are in close proximity and there exists field overlapping between them, such as in a microstrip double-spiral delay line shown in Figure 1.1. Cross coupling transfers interfering energy between adjacent or even non-adjacent transmission lines, which may induce spurious signals (crosstalk), preceding or lagging behind the original transmitted signal. Crosstalk at too high a level may result in an incorrect trigger or response before or after the intended signal.

Loss and coupling are the main problems in the design of delay lines and we will focus on these later. Size and weight are also a concern, and it is often a trade-off against the performance of delay lines. To minimise the package size, the cross-section dimension of the transmission media can be decreased or the separation between different parts of the delay line reduced. However, a smaller cross-section usually means increased current density and therefore higher conductor loss. Also, a closer proximity is often accompanied by increased cross coupling.

1.2 Superconducting delay lines

The discovery of superconductors offers the possibility to achieve miniaturised delay lines with a wideband performance. After 1986 when high-temperature superconductors (HTSs) were discovered, a lot of serious work was carried out to look into the application of HTS in delay lines substituting for the normal conductors dominant in conventional technologies.

Compared with good normal conductors, superconductors are superior in providing extremely low insertion loss when used as a delay line. This is due to their low surface resistance below the transition temperature. The low surface resistance also allows a superconducting circuit to form a compact structure without compromising the electromagnetic performance, and to operate over a wider frequency band. At such a low loss level, few or no amplifiers are needed to boost the signal, therefore the dynamic range can be improved significantly. In addition, the low operation temperature further lowers the noise figure of the device.

Comparisons between competing superconducting delay lines and conventional coaxial delay lines have been made[1]. Superconducting delay lines are very attractive for system designers to include into applications in electronic warfare and radar systems, such as cueing receivers[2], instantaneous frequency measurement subsystems[3], Electronic-warfare Support Measures (ESM) channelisers[4] and frequency modulated continuous wave (FMCW) radars[5]. Superconducting delay lines are also potentially employed in other signal storage devices and signal processing systems[6].

1.3 Challenges of this project

In this project, HTS delay lines with a novel routing structure are designed to operate from 2 to 18 GHz. This bandwidth has never been realised before by a superconducting delay line. The delay lines discussed in this work are made of thin film $YBa_2Cu_3O_{7-\delta}$ (YBCO) on a $LaAlO_3$ substrate. The miniaturization issue is one of the main challenges in the design, with a long time delay (25 ns or more) confined to a small area (2 inches in diameter).

Almost every aspect of the electromagnetic performances has something to do with the size. The loss of the HTS line depends on the current density in the conductors, which is largely determined by the line width and film thickness. The usable bandwidth is partly limited by the insertion loss, but mainly by the spurious resonances inherent to the circuit itself. These could be any parasitic propagating modes, resonances from certain parts of the circuit, or modes due to the package. The cross coupling present in the delay line may degrade the signal quality. It mainly depends on the separation between adjacent lines carrying signals, and also varies among different routing structures occupying the substrate area. Therefore, the geometric structures of the HTS delay line need to be carefully optimised in order to reach the best acceptable performance within a restricted wafer area.

A compact routing structure also requires precise fabrication capability for the film/substrate materials and for the patterned circuits. In superconducting thin-film devices, the narrowest strip and slot widths are on the order of micrometers to tens of micrometers. High resolution masks and accurate photolithography are needed. Specifically, a 25 ns HTS delay involves a 2 m or even longer transmission line, squeezed in an area with a 2-inch diameter. This requires a clean and defect-free substrate with uniform dielectric properties and a large-area, high-quality superconducting film. A single defect in either the substrate or film could significantly increase the return loss or even short the entire circuit.

To take full advantage of the low material loss of superconductors, proper packaging is required and the loss incurred from the transition/connection between the superconducting circuit and external connector should be minimised, as it may significantly affect or even dominate the transmission performance. This is especially critical for a wideband application. At low frequencies, the reflection loss due to the interconnections at the input/output may readily surpass the total loss of several meters of superconducting transmission line. As the

frequency goes higher, the surface resistance increases in proportion to the square of the frequency, and the return loss from the feed-line areas also becomes larger due to mismatches.

This thesis reports the attempts and outcomes made on tackling these challenges.

1.4 Organisation of the thesis

Chapter 2 gives an introduction to the applications of high-temperature superconductors (HTSs) in microwave devices and a literature review of HTS delay lines. A comparison of these delay lines demonstrated to date is listed in Table 2-1. Some comparative studies between HTS delay lines and other conventional technologies are also reviewed. The last section of this chapter is a brief introduction to delay line filters and some of their implementation examples.

Chapter 3 discusses the phenomenological theory of superconductivity as related to the work in this thesis. The two-fluid model and the surface resistance of the superconductors are explained in detail. The most used HTS materials and substrates for microwave applications are summarised. The characterisation methods of surface resistance are discussed as a background for the experimental work in Chapter 8.

The following three chapters give the design considerations, for the coplanar waveguides in Chapter 4, for the coplanar delay lines in Chapter 5, and for the transitions/connections between coplanar delay lines and external coaxial connectors in Chapter 6.

Chapter 4 mainly employs the quasi-TEM theory of transmission lines to derive the characteristic impedance, loss, and coupling for both the conventional coplanar waveguide (CPW) and the conductor-backed coplanar waveguide (CBCPW). Dimensions of the 50 Ω coplanar delay lines are defined. The variations of the loss and coupling between adjacent transmission lines with geometric configurations and frequencies are estimated. This will be the basis for the design, which takes both the size and the electromagnetic performance into account. The conductor loss of CBCPW is formulated based on the incremental-inductance method to look at the loss increment due to the presence of the conductor backing. The parasitic modes in the coplanar structures are discussed.

Chapter 5 gives the design considerations of the delay line, starting with the initial design concept and specifications for a *novel* delay line structure with *reduced impact of crosstalk*. A meander line with very short meander section is selected as the basic structure by comparing several routing layouts using full-wave simulations. To fill the round substrate area with the meander unit cells, the meander line is wound into a double-spiral structure, forming a double-spiral meander line (DSML), which is adopted as the layout of the experimental devices. With such a structure, the transmission line spirals in and then spirals out, so both input and output are on the edges of the wafer. The bandwidth and dispersion of the coplanar meander line are investigated. The DSML structure is compared with the conventional double-spiral line (DSL) by computation-intensive simulations. The admittance-matrix method is also introduced to calculate the S parameters of a meander line and help understand the coupling effect in the meander line.

Chapter 6 considers the design of the transitions from narrow coplanar waveguide to three types of wider transmission lines in order to facilitate the connections with the coaxial connectors. A CPW taper transition, a transition from narrow CBCPW to wide microstrip line, and a novel transition configuration from narrow CBCPW to tapered CPW are all modelled using 3D simulator-HFSS. The CPW taper transition and the CBCPW-to-CPW transition are finally implemented in the experimental devices.

Chapter 7 describes the fabrication, packaging and some general issues in the measurement set-up of the HTS delay lines.

The next two chapters present the experimental results and discussions.

Chapter 8 contains the detailed characterisation of the delay lines using resonator techniques. The quality factors and resonant frequencies of more than 1000 harmonics are measured over a wideband from 20 MHz to 20 GHz. The attenuation is estimated and the surface resistance of the superconductor is extracted based on TEM transmission line model. From this resonance measurement, useful information is also gained on the loss of the superconducting delay lines excluding the effect of connections. Temperature- and power-dependence measurements are presented. The sources of the measurement errors are addressed.

Chapter 9 gives the measurement results of fully connected delay lines as used in the application. The results are interpreted in both frequency and time domains. The effects of box modes and radiation are discussed. The measurement uncertainty is analysed. The results from this measurement are compared comprehensively with those from both resonance measurement and simulations. The power dependence of the measured transmission losses is shown.

Chapter 10 concludes the thesis. The application prospect of the reported delay line is addressed. The main findings of this work are summarised. The contributions to the design of microwave HTS delay lines and the knowledge in physical properties of HTS materials are evaluated. The limitations of this work are pointed out and some suggestions for the future research are given.

---

[1] S. H. Talisa, M. A. Janocko, D. J. Meier, C. Moskowitz, R. L. Grassel, J. Talvacchio, P. LePage, D. C. Buck, R. S. Nye, S. J. Pieseski, G. R. Wagner, "High-temperature superconducting wide band delay lines", *IEEE Trans. Appl. Supercond.,* vol. 5, no. 2, pp. 2291-2294, 1995.

[2] T. C. L. G. Sollner, W. G. Lyons, D. R. Arsenault, A. C. Anderson, M. M. Seaver, R. R. Boisvert, R. L. Slattery, "Superconducting cueing receiver for space experiment", *IEEE Trans. Appl. Supercond.*, vol. 5, no. 2, pp. 2071-2074, Jun. 1995.

[3] G. C. Liang, C. F. Shih, R. S. Withers, B. F. Cole, M. E. Johansson, "Space-qualified superconductive digital instantaneous frequency-measurement subsystem", *IEEE Trans. Microwave Theory Tech.*, vol. 44, no. 7, pp.1289-1299, Jul. 1996.

[4] R. F. Jeffries, R. B. Greed, D. C. Voyce, G. N. Nudd, R. G. Humphreys, S. W. Goodyear, "Further development of a future ESM channeliser with high temperature superconducting filters", *IEEE Trans. Appl. Supercond.*, vol. 11, no. 1, pp. 410-413, Mar. 2001.

[5] D. J. Kapolnek, D. L. Aidnik, G. Hey-Shipton, T. W. James, N. O. Fenzi, D. L. Skoglund, B. J. L. Nilsson, "Integral FMCW radar incorporating an HTSC delay line with user-transparent cryogenic cooling and packaging", *IEEE Trans. Appl. Supercond.*, vol. 3, no. 1, pp. 2820-2823, Mar. 1993.

[6] W. Hattori, T. Yoshitake, S. Tahar, "A re-entrant delay-line memory using a $YBa_2Cu_3O_{7-\delta}$ coplanar delay-line", *IEEE Trans. Appl. Supercond.*, vol. 9, no. 2, pp. 3829-3832, Jun. 1999.

Chapter 2 Literature review

2.1 HTS and its microwave applications

Superconductor is a material, which may not even be a good conductor at room temperature, the resistance of which disappears when it is cooled down to a certain temperature. Below this superconducting transition temperature, it has zero D.C. resistance and perfect diamagnetism[1]. Even at microwave frequencies (~1GHz), superconductors have 1000 times lower surface resistance than copper at room temperature. A comparison of the surface resistances between copper and superconductors is shown in Figure 2.1. Since the surface resistance of normal conductors and superconductors follow different frequency dependences ($f^{0.5}$ for normal conductors and f^2 for superconductors), an intercept point is expected where the superconductors lose the advantage of low surface resistance. But it was found, and can be seen from Figure 2.1, that this occurs at around 100 GHz. Most of the interesting applications are well below this frequency.

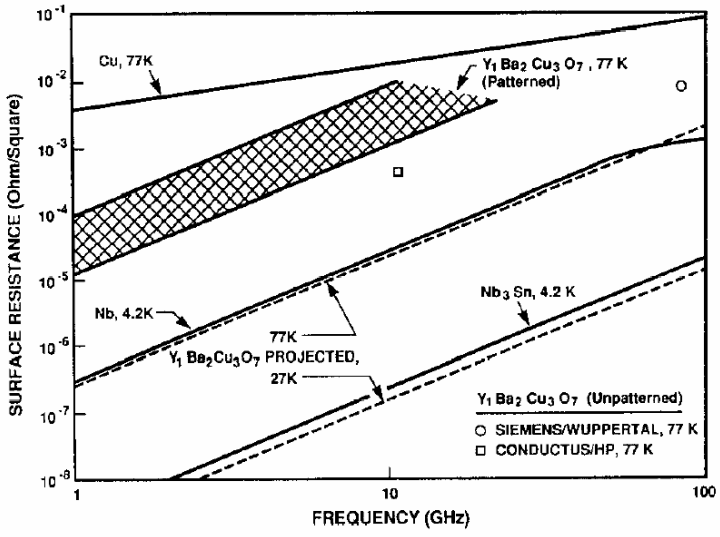

Figure 2.1 Surface resistance as a function of frequency for cooled copper and for superconducting Nb, Nb_3Sn, and $YBa_2Cu_3O_7$ (YBCO). Measured values for both patterned and unpatterned YBCO films are shown. The theory curves for YBCO were generated based on the two-fluid model. The parameters used were λ_p=150nm, T_c=93K and $\sigma_1=2\times10^6$S/m. ©IEEE [2]

Since it was discovered by H. K. Onnes early in 1911, superconductivity has attracted enormous and continuous interest in the sciences and technologies. At that time, application

prospects were poor because of the very low superconducting temperatures. Only after 1986 when high-temperature superconductors (HTSs) were discovered, being able to superconduct in liquid nitrogen (77K)[3], did the potential towards commercial usage attract huge amount of exploration from laboratories to industry. The applications range from magnetic-levitation for transportation, bio-magnetism in the life sciences, energy storage and transmission in power systems, to electronics in telecommunications.[4]

Particularly for the electronics application, a variety of HTS microwave components and systems have been successfully demonstrated[5] and some have been industrialised on a small scale[6] just a decade after the first HTS materials. In this field, electronic devices mainly take advantage of the low surface resistance and negligible phase dispersion of the HTS and try to avoid its nonlinearity. A delay line is the most direct vehicle to demonstrate these good properties, which will be reviewed in detail in the next section. First, some of the other applications of HTS in communications must be mentioned, as this is the most promising market place for superconducting products.

- High-Q resonators

Due to the low surface resistance of HTS, extremely high-Q can be achieved for HTS resonators. A quality factor of 3.9×10^6 was reported for a 3-dimensional HTS-sapphire-HTS resonator at 80K and 5.5 GHz.[7] The power handling of this resonator is also impressive, from kilowatts at 80K to hundreds of kilowatts at 4.2K. This high-Q resonator can be used to design high-performance filters and low phase-noise oscillators.[8] The achievable Q-values of planar HTS resonators[9] such as transmission-line resonators or disk resonators are relatively low due to the current crowding and radiation, but still much higher than planar copper resonators with the same dimensions. A J-shaped hairpin resonator claimed the highest Q among transmission-line resonators, which is 1.2×10^5 at 70K and 1.93 GHz.[10] Other more compact resonators in the form of meander lines[11] or spiral lines[12] usually have lower quality factors than this.

- Filters

Using high-Q resonators, a range of filters with nearly ideal passbands have been developed for mobile base stations[13], satellite communications[14], and radio astronomy front ends[15]. The

selectivity and insertion loss of passband filters benefit most from superconductivity. Selectivity depends on the number of resonators (poles). As the frequency resources become so crowded nowadays with the booming telecommunication services, sharp filtering selectivity is in high demand. However, for normal-conductor resonators, the *Q*-values are only on the order of tens to hundreds. The rapidly increasing insertion loss with the number of resonators severely restricts the number of poles and therefore limits the achievable selectivity. To fill this demanding gap, HTS filters appear to be a promising choice. Without sacrificing the acceptable insertion loss, the achievable poles of superconducting filters can outnumber the conventional filters. A 32-pole highly-selective HTS filter was realised with a maximum insertion loss of only 1.15 dB in the passband. [10]

While maintaining low insertion losses, HTS filters can be miniaturised to a size mainly prohibited by the capability of the patterning process. Such kinds of filters can be realised by lumped elements[16], which may be physically much smaller than the wavelength at their operating frequency. A 1.78 GHz HTS bandpass filter has been fit in a 1 cm^2 area.[17] Because the lumped-element filters usually employ interdigital capacitors and meander/spiral inductors, their losses are relatively high, compared with transmission-line filters. Lumped elements made of copper usually have unacceptable passband insertion loss for high performance applications.

- Antennas

Some antennas can also benefit from the extremely low resistive loss of superconductors. For those antennas with much larger loss resistance than their radiation resistance, the improvement of radiation efficiency by introducing HTS is impressive. This is the case for the antenna with dimensions smaller than the wavelength.[18] In addition, for a phased array antenna with many radiation elements, a superconducting feed network can help to increase the gain. A 64-element, 30-GHz HTS microstrip antenna on a 2-inch $LaAlO_3$ was reported to demonstrate this capability.[19]

- Switches and filterbanks

The superconducting-to-normal transition of HTS can be used to design switches. This transition can be driven by increasing the temperature or current density in the

superconductor. So, the switching control can be a separate heater near the superconducting element (thermal switch), or a bias current through the element. A filter-bank using thermal switches was fulfilled for the application in channelised receivers[20]. Based on the current-control concept, a switchable band-stop filter was realised with a step-wise change of bandwidth by increasing the current and gradually driving a series of superconducting inductors to their normal states.[21]

- Receiver front-ends

On the system levels, superconducting passive components can be hybridised with semiconductor active components in receiver front-ends[8]. The passive components in the front-ends can be realised solely with HTS, such as power dividers and different types of filters. Others have to be hybrid, such as amplifiers/oscillators (embedded with superconducting resonators) and mixers.

- Others

Using the Josephson effects of superconductors[8], there are a series of all-superconductor active devices available. The advantage of these devices is their low noise level. However, they only function for low-power applications. Moreover, these devices are difficult to fabricate.

A problem worrying the HTS applications is the poor power handling. This obstructs the use of HTS in devices with high-power capability.[22] At high power levels, the nonlinearity of superconductors becomes important. This usually generates unwanted harmonics and intermodulation, which is a major concern in many communication systems.

2.2 HTS Delay lines

2.2.1 Why HTS delay lines

The major advantages of HTS delay lines are the low insertion loss, small dispersion and wide bandwidth. Key factors that determine the figures-of-merit for delay lines are the attenuation, bandwidth, signal quality, and phase tracking.

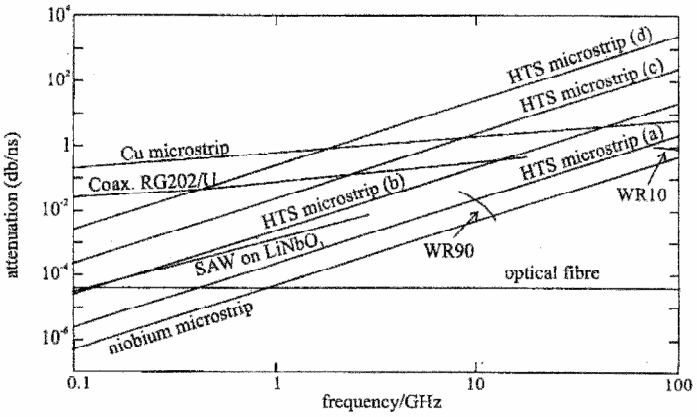

Figure 2.2 The attenuation per nanosecond as a function of frequency for various transmission media. The HTS is for a wide microstrip at 77K with R_s=100μΩ at 10 GHz and is 10μm thick, except for (d) which is 0.35 μm thick; all are on an MgO substrate. The thickness of the substrate is (a) 1mm, (b) 0.1mm, (c) 0.01mm and (d) 1μm. The copper microstrip is on the same substrate with a thickness of 1mm, and is at 77K with a surface resistance at 10 GHz of 8.7mΩ. The niobium microstrip is the same size as the copper, with a surface resistance of 20μΩ at 10 GHz and 4.2K. WR 90 and WR 10 are two waveguides and SAW is surface acoustic wave device. © Cambridge University Press [9] (The notation "Coax. RG202/U" in the graph should be "Coax. RG402/U".)

- Attenuation

Attenuation per unit delay is one of the figures-of-merit for delay lines. Various values of attenuation for different transmission media are shown in Figure 2.2. Among these, the superconducting delay lines have one of the lowest attenuations. The optical fibre and surface acoustic wave (SAW) delay line also provide extremely low loss and have been widely used. The waveguides have low loss but they are not practical for long delays because of the big size. The coaxial cable delay line is lossier at low frequencies than other good delay lines. To extend the operation frequency range of coaxial lines, dimensions of the conductors have to be reduced, which may further increase the attenuation. This is also unfavourable as far as the size is concerned, because thinner cables usually allow a larger minimal-bending-radius, which increases the package volume.

- Bandwidth

Bandwidth is another figure-of-merit of delay lines. The time-bandwidth (TB) products in Figure 2.3 allow to assess both the potential bandwidth and the delay capability of various technologies. The superconductor technology can achieve the largest bandwidth within 1000 ns delay capability, which is sufficient for most of the applications in electronic warfare and

radar systems. SAW and AO (acousto-optic) technologies, which could offer very low loss, have smaller bandwidth. They are best operating below 1 GHz. A sophisticated comparison of these technologies can be found in [9].

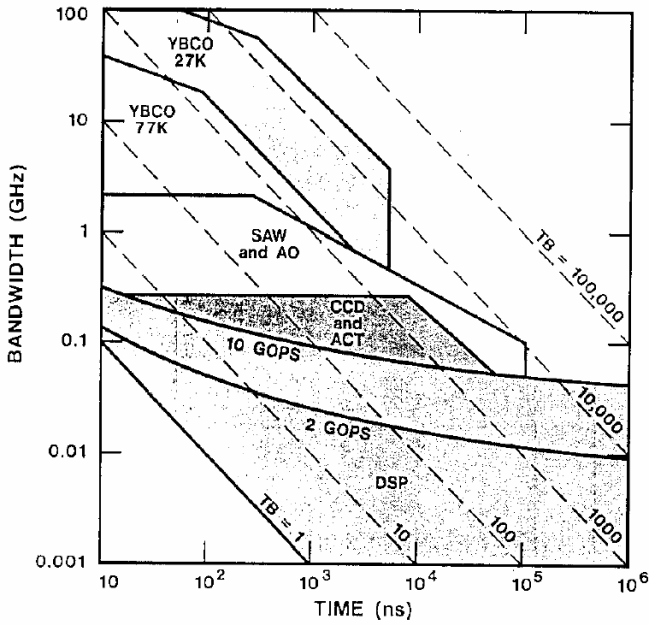

Figure 2.3 Near-term projections of signal processing capabilities for various technologies (1990). ©Microwave Journal [23] (CCD: charge coupled device; ACT: acoustic charge transport; GOPS: giga operations per second)

By comparing the attenuation and bandwidth of different technologies, one can see that superconducting delay lines are very promising to achieve both at the same time. Besides, superconducting delay lines are also ready to be miniaturised, because they can be made very narrow while still maintaining the loss on an acceptable level.

- Signal quality

Minimal signal distortion is another indication of good delay lines. As mentioned in Chapter 1, this is mainly affected by the crosstalk, which is one of the most detrimental effects in the operation of delay lines. In this aspect, a coaxial cable is advantageous because its outer conductor provides good shielding for the signals. Potentially, crosstalk in the delay lines patterned on HTS thin films can also be reduced, as the signal lines can be very narrow and well separated, but this needs to be carefully considered in the design stage. For normal conductors, the dispersion of the materials also has some effect on the signal quality. But for

HTS, this is no longer a problem because HTS intrinsically has no phase dispersion due to the frequency-independent penetration depth (to be discussed in Chapter 3).

- Phase tracking

Phase tracking is the ability of multiple delay lines to reproduce their phases relative to each other. Good phase tracking is required on the system level, where a number of delay lines are used. As pointed out by Ryan[24],

> "Insertion loss greater than 50 dB and phase tracking worse than 20 degree in the 2-6 GHz range are typical values for a 100 ns coaxial delay line. Amplifiers must be used to compensate for insertion loss which compounds the phase tracking problems between the numerous delay lines in a system. Phase compensation circuitry is often required to correct for this dispersion which can add significant size and complexity to the system…"

Active devices often have poor phase tracking due to the thermal effect. As HTS delay lines can do without active compensation components, they can provide better phase tracking than conventional delay lines.

2.2.2 Review of Superconducting delay lines

A superconducting meander line was investigated early in 1968.[25] Although it was designed as a slow-wave element, the authors already saw it as "a promising solution to the problem of providing low-loss linear and dispersive delay". After that, studies of superconducting delay lines had been quiet for many years until the discovery of HTS in 1986. Thereafter, a few HTS delay lines were demonstrated in 1990s, mainly encouraged by the USA High Temperature Superconductivity Space Experiment-II (HTSSE-II) project[26]. Most of them adopted conventional meander[27,28,29,30] or double-spiral[31,32,33,34,35,36] structures. Only Fenzi *et al.*[37] presented a novel meander structure based on their unit-cell design concept. The most popular transmission-line types for HTS delay lines are stripline[27,33,36] and coplanar line[28,29,31,35,37].

Stripline is attractive because of its uniform dielectric medium and therefore negligible forward coupling. But the implementations of HTS delay lines with stripline always

experience the problem with air gaps between the upper and lower wafers when clamped together. This makes it difficult for stripline delay lines to achieve resonance-free passband.

Coplanar line features a low level of cross coupling. But a big challenge is to suppress the parasitic slotline modes caused by unequal potentials on the in-plane grounds. All the coplanar delay lines demonstrated earlier had many crossover wires bonded in order to achieve a resonance-free bandwidth. However, wire-bonding is a difficult and troublesome process. Too many crossover wires may increase the loss and reflections, while too few may fail to reduce the slotline modes.

Although microstrip is not a favourable structure due to its relatively strong cross coupling between adjacent lines, quite a few delay lines were patterned with it [30,32,34,38,39,42,43]. To reduce the crosstalk, microstrip delay lines have to be well separated at the cost of the total delay per unit area. The maximum delay achieved on a 2-inch wafer was only 8 ns. However, microstrip delay lines are more likely to hold pure propagation modes and be free of resonance, as compared with striplines and coplanar lines. In parallel with the reported coplanar delay lines in this thesis, investigations of microstrip delay lines are also carried out in the same project[40,41].

In the following, four implementation examples of superconducting delay lines are reviewed and all the published delay-line work is summarised.

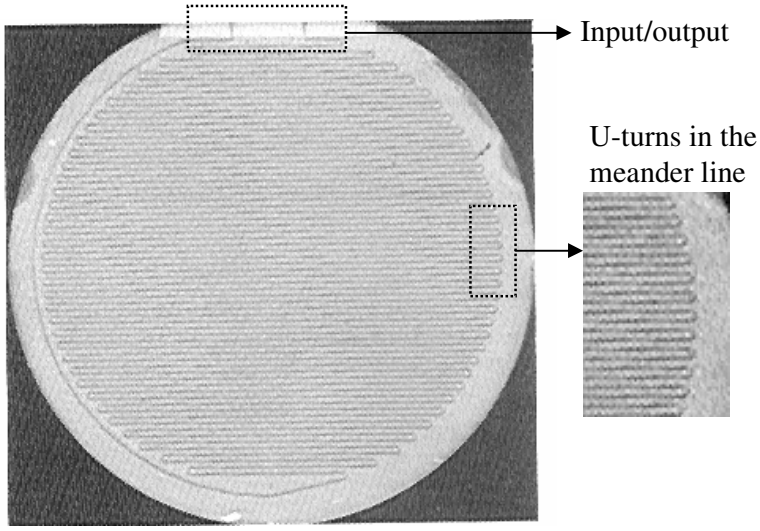

Figure 2.4 45ns NbN CPW delay line on a 3-inch $LaAlO_3$ with a meander structure. ©IEEE [28]

The longest delay achieved on a single wafer is from a 45 ns NbN (low temperature superconductor) coplanar meander delay line, patterned on a 3-inch $LaAlO_3$ (LAO) as shown in Figure 2.4[28]. Only 1.7 GHz resonance-free bandwidth was achieved with the CPW line, which used 136 gold bond-wires. A conductor-backed version of the delay line with the same layout had 1.2 GHz bandwidth. This is the only conductor-backed CPW (CBCPW) delay line demonstrated before the work in this thesis. According to the authors' experience[42], a double-spiral structure yields "small but overlapping resonances throughout the frequency range" whereas a meander line yields "at least one resonance-free band". It is understood that the resonance in the meander structure is very likely due to the reflection from the U-turns as shown in Figure 2.4. Especially for those meander lines with repeated coupled lengths, the first resonance corresponds to the frequency for which the repeated section is half a wavelength.[42] However, the stated "overlapping resonances" in double-spiral structures have never been confirmed by others' work. The same authors also presented a computer-aided design of the meander and spiral delay lines.[43] This is one of the scarce modelling studies published on delay lines. Using the circuit analysis software HP-MDS, an arrangement of coupled-line elements were used to model the coupling between different sections of the delay lines. The layout of the spiral was approximated by a series of coupled lines of decreasing lengths. This is a fast approach to gain information of the complex coupling structures. But it is far less accurate than full-wave simulations, which can take the full coupling effect into account.

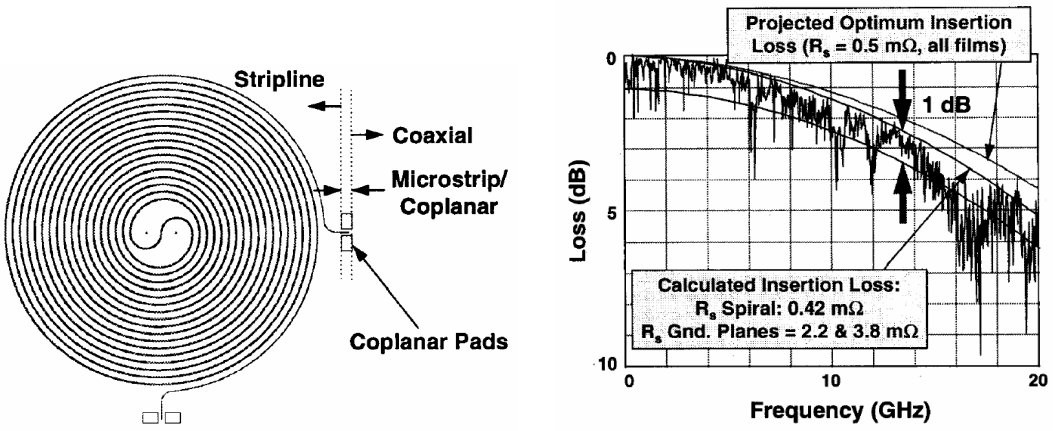

Figure 2.5 The double-spiral pattern for a 22.5 ns stripline delay line and the measured insertion loss at 77K. ©IEEE [36]

In Figure 2.5, the frequency response of a stripline delay line is shown up to 20 GHz. At 77K, the calculated loss (pointed by the lower text box in the graph of the insertion loss) is among the lowest ever shown on HTS delay lines, as will be seen from the comparison in Figure 2.7. However, the resonance-free bandwidth is only limited between 2 and 6 GHz. The ripples also turn large (2 dB) above 14 GHz. The air gaps in the stripline may still account for these ripples and resonances, although new measures[36] were taken to minimise these gaps. This has long been a challenge to the design of stripline circuits. In addition, the transition from the external coaxial connector to the stripline needs to be carefully implemented[36]. A stripline-to-coplanar transition may be required in order to facilitate the connection with coaxial connectors.

Liang *et al.*[33] also tested three HTS stripline delay lines, two of them on $LaAlO_3$ and one on sapphire (single crystal α-Al_2O_3). The $LaAlO_3$ substrate was thinned from 0.508 mm to 0.254 mm for a 27 ns delay and to 0.127 mm for a 44 ns delay. The 44 ns delay line was the most densely routed one ever demonstrated, benefiting from its thinned substrate. Firstly, a thinner substrate may reduce the cross coupling by confining more electrical field in the dielectric between the signal line and grounds rather than spreading horizontally. This reduces the field overlapping between adjacent lines. Secondly, in order to keep certain characteristic impedance on a thinner substrate, the width of the transmission line has to be reduced. This potentially reduces the size of the whole circuit. However, as a trade-off against the attenuation, the lines used in [33] were deliberately widened, resulting in characteristic impedances lower than 50Ω. So, Klopfenstein tapered impedance-transformers[44] were employed there. This is not favourable as far as the bandwidth is concerned. In the fabrication, the substrate was thinned to 0.254 mm by lapping. Further to 0.127 mm, the fragile substrate had to be strengthened using a bonding technique rather than in a free-standing state. Another delay line was produced for the first time on M-plane sapphire. Without the twin-structure as in LAO, sapphire is truly single crystal and can be made into larger wafers (3-inch is standard). It also has one of the lowest loss tangents ($<3\times10^{-8}$ at 77K versus 10^{-5} for LAO) and is physically stronger than LAO. Therefore, sapphire is a good candidate in making high-performance microwave devices. However, sapphire is anisotropic in its dielectric properties. Although the hexagonal (0001) plane has a uniform dielectric constant, it is not suitable to grow epitaxial HTS film due to the mismatched symmetry with the growth plane of HTS. The HTS can only be prepared on

$(1\bar{1}02)$ plane (R-plane) or $(10\bar{1}0)$ plane (M-plane) by using buffer layers. The anisotropic dielectric constant means the HTS circuit can not be randomly oriented on these planes. A non-uniform transmission line was designed to compensate for the anisotropy while keeping a constant characteristic impedance.[33]

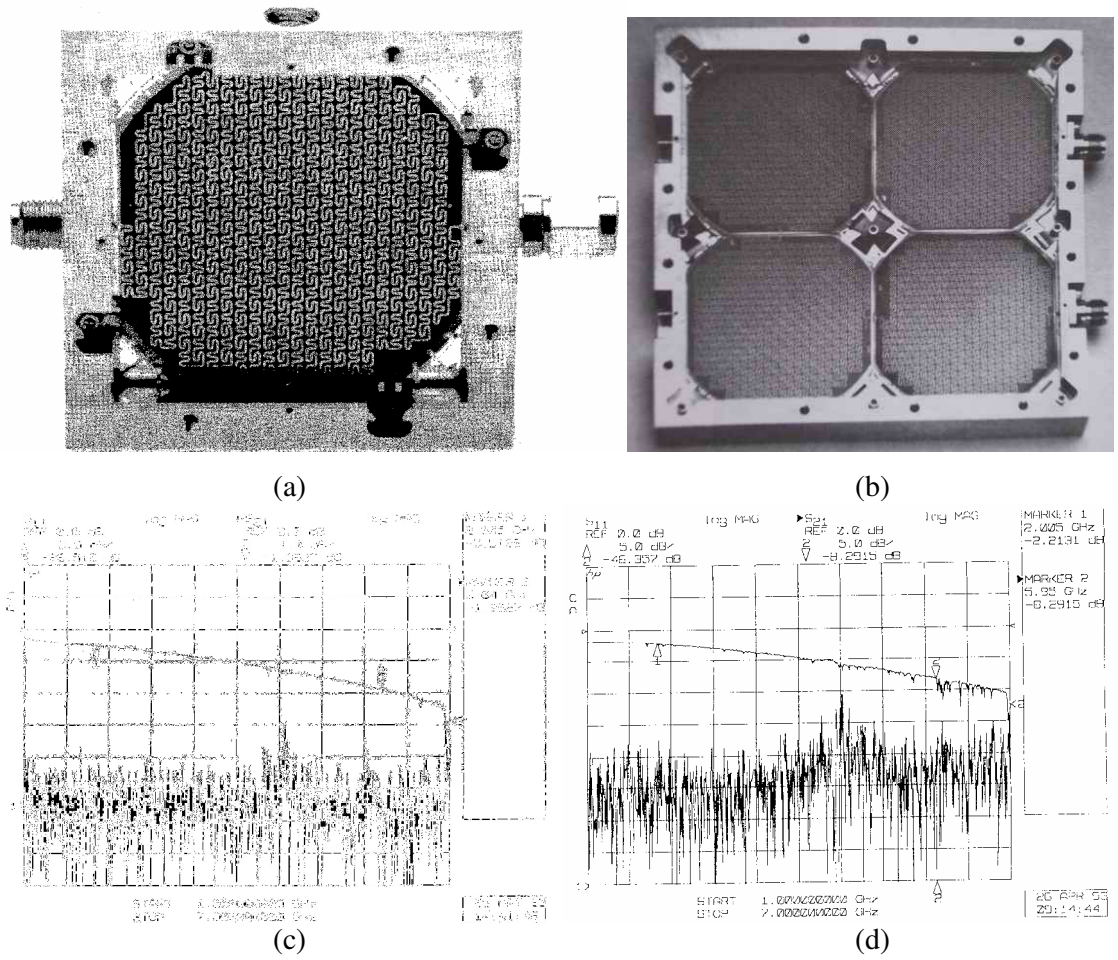

Figure 2.6 (a) A 25 ns coplanar delay line based on the unit-cell structure. (b) A package of a 100 ns delay line. (c) Measured S_{21} and S_{11} of (a). (d) Measured S_{21} and S_{11} of (b). ©SPIE [37]

The maximum total delay demonstrated on HTS is 100 ns with a cascade of four 25 ns delay lines as shown in Figure 2.6(a,b)[37]. The transmission medium is coplanar waveguide. Crossover bond-wires were used periodically to impose equal potentials on the in-plane grounds. The routing structure is composed of many meandered unit cells. The coupling within each cell and the interaction between cells were modelled. This design concept may significantly reduce the computation efforts by not modelling the structure as a whole. The bandwidth of this delay line was limited by a resonance at around 7 GHz. This may be a reflective resonance due to the variously oriented bend structures. Interconnections between

the four 25 ns delay lines had been successfully implemented to have a 100 ns total delay without degrading the performance achieved on a single wafer. Planar connections with gold ribbons were used without resorting to the coaxial male/female connections. Excellent phase tracking (less than 10 degree over 2-6 GHz) was shown by two 100 ns delay lines, much better than that of conventional coaxial delay lines, which is typically more than 20 degree over the same frequency range.[24]

Table 2-1 summarises the published superconducting delay lines, including the CBCPW delay line to be reported in this thesis. The listed "bandwidth (BW)" of the delay lines corresponds to the resonance-free passband ending with the first obvious resonance. To compare their performances in terms of insertion loss, some of the data are compiled and plotted in Figure 2.7. Included is also an attenuation curve of RG402 coaxial cable. In an attempt to follow the same criteria, the data are either taken directly from the S_{21}-responses in publications or estimated from relevant information, so they are not necessarily consistent with what was claimed by the authors. The values of "loss (dB/ns)" in the figure correspond to the lowest possible insertion losses ignoring ripples and resonances. The real insertion losses have to include at least 1-2 dB ripples in most designs, plus the possible resonances at certain frequencies. Admittedly, these data may not precisely represent the performances of the delay lines because most of the demonstrated S_{21} responses (especially for those stripline delay lines) are mixed with transmission notches. This makes it difficult to tell between ripples and resonances. The frequency resolution of the published results and supporting information provided also vary significantly. Some specific notes for each group of data are added in the caption of Figure 2.7.

Table 2-1 Summary of the superconducting delay lines from published literatures. (attached)

Table 2-1 Summary of the superconducting delay lines from published literatures.

Data Source*	Pattern**	Conductor	Substrate, dia.(cm)/thickness(μm)	Line-space (μm) /decoupling (dB)	*w*(μm)/*s*(μm)*** [Z_0(Ω)]	Delay (ns) /length (cm)	*BW* (GHz)	*IL* (dB/ns) [freq.(GHz), temp.(K)]	Ripple (dB) [freq.(GHz)]
Liang93(SP)[33]	D	YBCO	LAO, 5/254	770/45	100 [31.7]	27/170		0.22[6,77]	2[6], 8[10]
			LAO, 5/127	406/52	100 [23.5]	44/270		0.36[6,77]	3[2], 10[6]
			m-plane sapphire, /430	1524	158-172	9		0.11[6,77]	0.5[2], 1.5[6]
Talisa95(SP)[36]	D	YBCO	LAO, 5.08/250	900/50	150 [27]	22.5/150	2-6	0.22[20,77], 0.04[5,77]	1[2], 1[10], 2[20]
Shen91(CP)[35]	D	TBCCO	LAO, 2.54×2.54/504	500/50	30/70	11		<0.25[8,77]	
Hofer93(CP)[31]	D	YBCO	LAO, 1×1/500	200/40	15/10 [36]	3/25.7		"TB=51"	
			LAO, 2×2/1000	800	20/40 [50]	5/43.4		"TB=23"	
Hohen93(CP)[28]	M	NbN	LAO, 7.62/508		60/120(CPW)	45/430	1.7	<0.01[1.7,4.2]	1[1.7]
			LAO, 7.62/508		60/132(CBCPW)		1.2	<0.01[1.2,4.2]	1[1.2]
Fenzi 94(CP)[37]	U	TBCCO	LAO, 5.08/			25	7	0.068[6,77]****	~0[6]
Tsang97(CP)[29]	M	YBCO	LAO, 2×2/500	1250	50/100	5/43	6	<0.2[6,78]	0.5[6]
Wu97(CP)[38]	D	YBCO	LAO, 3.5/500	/50	60/	10/85		0.63[6,77], 1.3[12,77]	2[2], 8[4], 3[6]
Wu97(MS)[38]	D	YBCO	LAO, 3.5/500	1500	160	5/		0.55[5,77], 1.2[10,77]	1[1], 3[5], 5[10]
Hornak89(MS)[32]	D(R)	YBCO	$LaGaO_3$+sapphire	375	125	6/31			
Bourne90(MS)[39]	M	TBCCO	LAO, 1×1/		50	1/13.9			
Lyons91(MS)[34]	D	YBCO	LAO, 5/508	/35	160	7			
Track91(MS)[42]	M	YBCO	LAO, 2.54×2.54/508	400	150	5/60		1.2[4.5,77]	
Track93(MS)[30]	M	NbN	LAO, 5.08/250	2540	80	8/64	6	0.38[20,5]	2[20]
Su04(MS)[41]	DM	YBCO	LAO, 5.08/250	170/9	85	29~73#/433	9##	0.118[10, 77]	2[20]
Wang04(CP)[57]	DM	YBCO	LAO, 5.08/508	390/33	40/74 (CPW)	25/228			
			LAO, 5.08/508	390/33	40/74 (CBCPW)	25/228	2-18	0.041[10, 30], 0.061[10, 60], 0.144[10, 77]	0.1[2], 0.5[8], 0.3[12], 0.9[16], 1.5[18]

* SP: stripline; CP: coplanar; MS: microstrip. ** D: round double-spiral; D(R): rectangular double-spiral; M: meander; U: unit-cell; DM: double-spiral meander line. *** *w* is the width of the signal line and *s* is the slot width of the coplanar waveguide. **** A 100ns total delay is achieved by cascading four 25ns delay lines. The resultant insertion loss is 0.08dB/ns at 6GHz and 77K. # 29ns at 0.05GHz, 73ns at 20 GHz. ## The bandwidth is limited by box resonances.

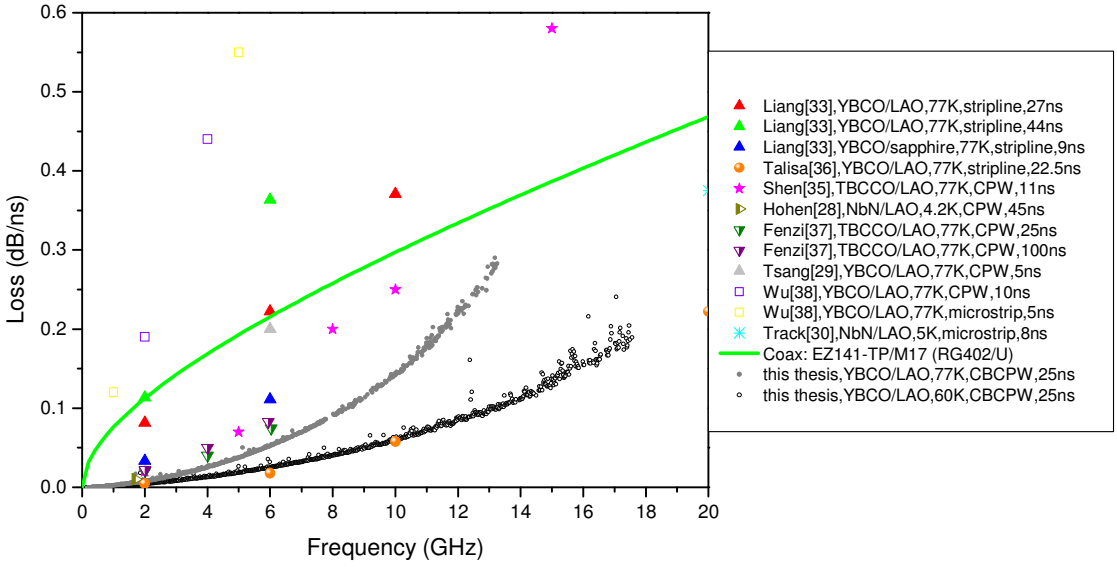

Figure 2.7 Compiled data for the insertion losses of various delay lines. The "loss" corresponds to the lowest possible insertion loss, ignoring ripples and resonances unless otherwise stated. The experimental results of the CBCPW delay line reported in this thesis are also included. (Notes: Talisa[36] – calculated results with R_s of the signal line set as 0.42 mΩ and R_s of ground planes as 2.2 and 3.8 mΩ as pointed by the lower text box in Figure 2.5. Shen[35] - theoretical values based on R_s of 3mΩ at 20 GHz and loss tangent of 5×10^{-5}. Not enough experimental data were given. The measured attenuations were higher than the theoretical values below 10 GHz. Coax - fitted attenuation curve for a coaxial cable equivalent to RG402/U. See Appendix D for details. This thesis – obtained from the measurement of the CBCPW delay line using resonator techniques. See Chapter 8 for details. This is the loss of the superconducting part in the delay line, excluding the loss due to the connections. The measured S_{21} responses of the fully connected delay line are given in Chapter 9.)

In summary, all previous superconducting delay lines have very limited resonance-free bandwidth, which is hardly beyond 7 GHz. The CBCPW delay line to be reported in this thesis has the widest resonance-free band from 2 to 18 GHz.

The stripline YBCO delay line presented by Talisa *et al.*[36] gives the lowest attenuation at 77K if resonances and ripples are ignored. That is 0.2dB/ns at 77K and 20 GHz. However, the overall S_{21} response of this stripline delay line is dominated by many transmission notches.

Fenzi's coplanar delay line[37] is the only one with negligible ripples. This indicates nearly perfect matching at the input and output connections and very low level of cross coupling. The interconnections between the cascaded delay-line units are also very efficient without incurring much return loss.

Compared with the coaxial cable (RG402/U at room temperature), superconducting delay lines have much lower attenuation below 10 GHz. The significant volume reduction of HTS

delay lines, compared with the conventional coaxial delay line, could also be maintained even in the package with cooling systems. This is being substantiated by increasingly compact cooling systems. Quoted from [36], Table 2-2 gives a comparison between a conventional coaxial delay line used at Westinghouse and a projected 200 ns HTS delay line. The reliability and economical issues of HTS devices have also been given serious considerations in [45].

Table 2-2 Comparison between a conventional delay line used at Westinghouse and a projected 200ns HTS delay line operating between 3 and 5 GHz. (1995)[36]

Parameters	Coaxial (amplifiers are used)	HTS
Total insertion loss/gain(dB)	0	-3.6 (max.)
Noise figure (dB)	23	1.3 (max)
Output 3rd-order intercept point (dBm)	27	40
Delay (ns)	200	200
Approximate size (in cm)	48×15×1.5	45×13×13*
Power consumption (W)	9	50

* Estimated using cryocooler from Sunpower, Inc.

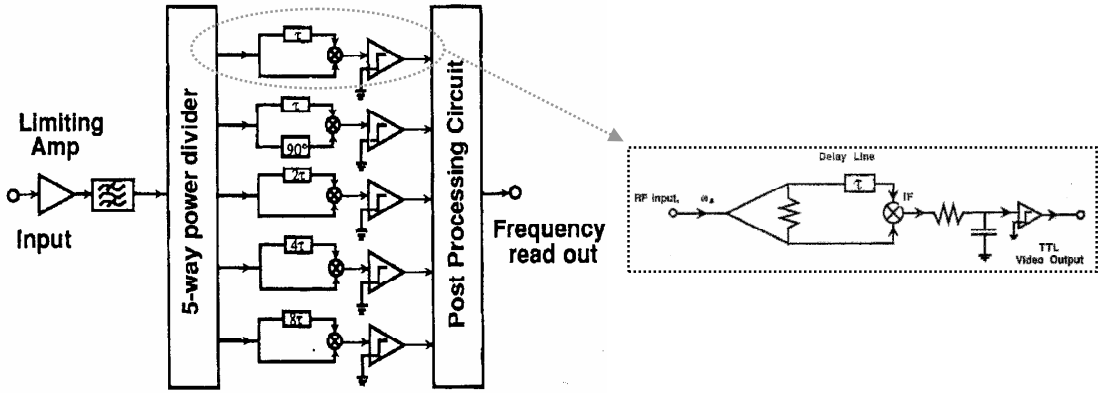

Figure 2.8 Schematic diagram of the DIFM subsystem and one of its phase discriminators. ©IEEE [48]

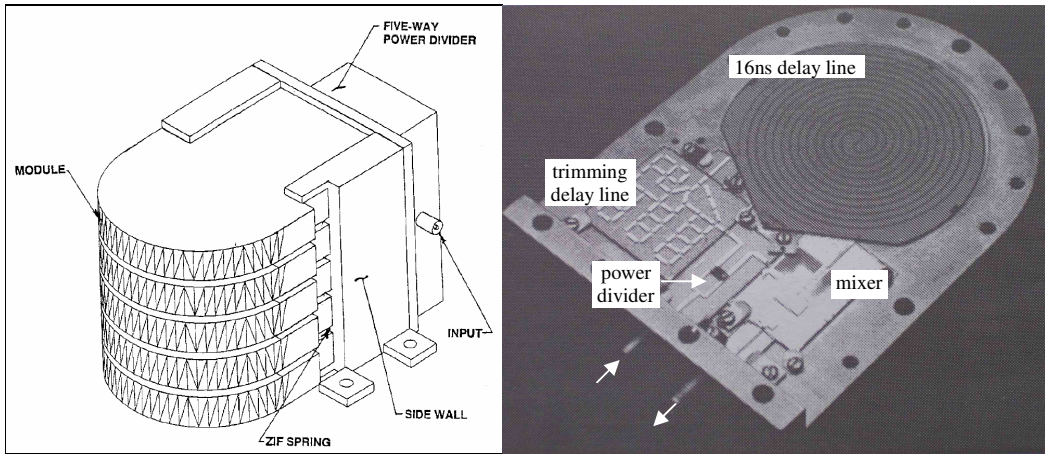

(a) (b)

Figure 2.9 (a) Schematic diagram of the packaged DIFM, consisting of 5 modules with 2-, 4-, 8-, 16-ns delay lines embedded. (b) Picture of the discriminator module with a 16 ns HTS delay line, a trimming delay line, a power divider, and a self-biased mixer. ©IEEE [48]

2.2.3 An application example of HTS delay lines

Some applications have been demonstrated with HTS delay lines included on system levels of electronic warfare and communications [9,45,46,47,48]. A digital instantaneous frequency measurement (DIFM) subsystem is taken here as an example.[48] DIFM is used to determine the frequency of unknown signals over a broad frequency band. As diagrammed in Figure 2.8, all the components marked as "$n\tau$" (n=1,2,4,8) are realised by different lengths of HTS delay lines. The frequency is identified by comparing the phase of the unknown signal with the phase of a time-delayed (by $n\tau$) replica of the same signal.

The subsystem is made of a series of phase discriminators with different delay elements. The frequency resolution of the system is inversely proportional to the maximum delay time. The accuracy of the frequency determination is affected by the deviation from a constant group delay and variation of the line length. Therefore, the delay line used in this subsystem is required to have a long delay, small dispersion, and good phase tracking. As in Figure 2.9, the flight system is a stacked structure, taking full advantage of the ground-signal-ground configuration of the stripline.

2.2.4 Transversal delay-line filters

All aforementioned delay lines are intended to just provide a real time delay over a frequency band as wide as possible. Ideally they should be non-dispersive (linear phase, constant group delay). For some applications of this kind, if the delay line is dispersive, a group-delay equaliser may be required. There is another type of delay line with filtering functions to create a non-linear phase, which is called transversal delay-line filter or tapped delay line.[49] Delay-line filters have the control over both phase and magnitude, which is not easily achieved for resonator-type filters. One example is the quadratic-phase (linear group delay) chirp filter, the time-frequency response of which is shown in Figure 2.10(b). It can be used in pulse compressive receivers[50].

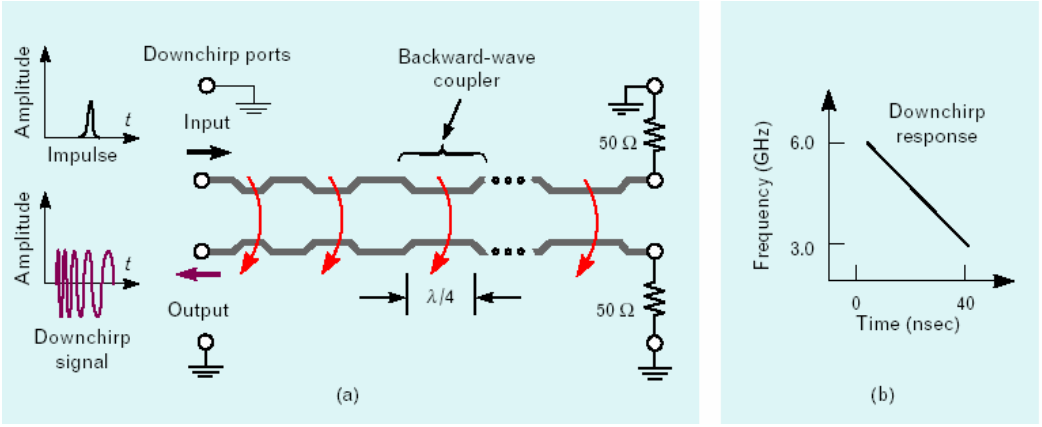

Figure 2.10 A structure of the backward-coupling delay-line filter and its time domain amplitude response. The linear relation between the delay time and frequency is shown on the right. © The Lincoln Laboratory Journal [50]

The chirp filter can be constructed in either a backward-coupling-type[51] (Figure 2.10(a) and Figure 2.11(a)) or a reflective-type[52] (Figure 2.11(b)).

The backward-coupling-type consists of a series of backward couplers, with different lengths and separations. Each coupler has the maximum backward coupling towards the output port at the frequency for which its coupled length is a quarter of a wavelength. By changing the distance from the input port and the inter-line separation of the coupler, the amplitude and phase of the backward coupling can be changed. The superposition of all these coupled signals can be designed to produce certain phase response. For instance, if the coupled length increases with the distance down the line, *lower*-frequency components in the input pulse will be coupled back to the output *later* than higher-frequency components because of the

longer path length. As shown by the amplitude-time response in Figure 2.10(a), a single pulse is therefore spread into a train of signals with different frequency components. If the train of signals is sent back in from the opposite end of the delay line, it can be compressed into the single pulse in a reversed way. The backward-coupling-type delay-line filter is a double-line, 4-port structure. The input and output are on the same side, while two ports on the other side are connected with matched loads.

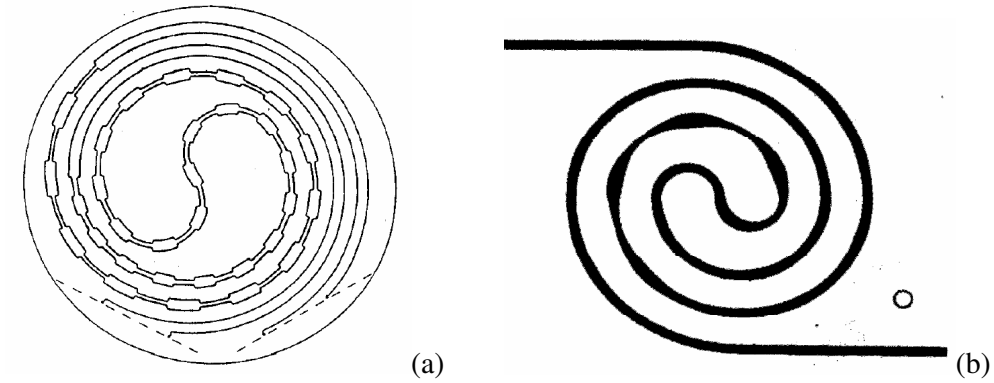

Figure 2.11 (a) A delay-line filter with cascaded backward-coupling couplers[34]; (b) a reflective delay-line filter with a series of impedance steps forming a non-uniform double-spiral line[52]. ©IEEE

Unlike the four-port coupled-line transversal filters, the reflective delay-line filter is a two-port device, with the input and output at the same port. So a directional coupler is required to separate them. The bandwidth of this coupler is the main limit of the achievable bandwidth of the device. This filter works in a similar way as the coupled-line version except that the output is the superposition of the reflections from each impedance steps rather than the backward couplings. The layout of such a filter is shown in Figure 2.11(b).

The synthesis of the delay-line filter is an inverse problem to seek the geometric configurations from the complex transmission coefficients, with both magnitude and phase specified. This usually involves an iterative procedure[53,54]. But Huang[55] developed a time-domain synthesis technique, which is non-iterative. Synthesised using this technique, the delay-line filter consists of cascaded couplers or impedance steps, without having to be quarter-wavelength long for each coupler or step. This eliminates the 3rd-order harmonic of the $\lambda/4$ coupler, and could increase the bandwidth to more than 100%[56]. The length of the coupler or impedance step is actually determined by the time domain resolution. Therefore, a

smooth transmission line can be formed as in Figure 2.11(b). Another advantage of this synthesis technique is that it can take the multiple reflections into account.

To offset a dispersive delay line in order to have a constant group delay, the equaliser with a compensating phase response can also be designed using this technique.

2.3 Summary

HTS delay lines have demonstrated many applications either using their long time delay or filtering function. Both make the best use of the low surface resistance of superconductors. However, the design of delay lines is not purely a material issue. The performance of the delay line greatly depends on the structure design. Although some HTS delay lines have been successfully included into demo systems, the bandwidth is still a problem. This obstructs the delay line from achieving the time-bandwidth product it potentially can. More investigations are needed to tackle this problem from the point of structure designs.

---

[1] T. P. Orlando, K. A. Delin, *Foundations of applied superconductivity*, Addison-Wesley, 1990.
[2] W. G. Lyons, R. S. Withers, J. M. Hamm, A. C. Anderson, P. M. Mankiewich, M. L. O'Malley, R. E. Howard, R. R. Bonetti, A. E. Williams, N. Newman, "High-temperature superconductive passive microwave devices", in *1991 IEEE MTT-S Int. Microwave Symp.*, pp. 1227-1230, 1991.
[3] J. G. Bednorz, K. A. Müller, "Possible high T_c superconductivity in the Ba-La-Cu-O system", *Z. Phys.*, B64, pp. 189, 1986.
[4] http://superconductors.org
[5] R. R. Mansour, "Microwave superconductivity", *IEEE Trans. Microwave Theory Tech.*, vol. 50, no. 3, pp. 750-759, Mar. 2002.
[6] B. A. Willemsen, "HTS filters subsystems for wireless telecommunications", *IEEE Trans. Appl. Supercond.*, vol. 11, no. 1, pp. 60-67, Mar. 2003.
[7] Z.-Y. Shen, C. Wilker, P. Pang, W. L. Holstein, D. W. Face, D. J. Kountz, "High T_c superconductor-sapphire resonator with extremely high Q-values up to 90K", *IEEE Trans. Microwave Theory Tech.*, vol. 40, pp. 2424-2432, 1992.
[8] Z.-Y. Shen, *High-temperature superconducting microwave circuits*, Artech, 1994.
[9] M. J. Lancaster, *Passive microwave device applications of high-temperature superconductors*, Cambridge University Press, Cambridge, UK, 1997.
[10] G. Tsuzuki, M. Suzuki, N. Sakakibara, "Superconducting filter for IMT-2000 band", *IEEE Trans. Microwave Theory Tech.*, vol. 48, no. 12, pp. 2519-2525, Dec. 2000.
[11] H. R. Yi, S. K. Remillard, "A superconducting thin film filter of very high wide-band rejection", in 2003 *IEEE MTT-S Int. Microwave Symp*, pp. 1893-1896, 2003.
[12] F. Huang, "Ultra-compact superconducting narrow-band filters using single- and twin-spiral resonators", *IEEE Trans. Microwave Theory Tech.*, vol. 51, no. 2, pp. 487-491, Feb. 2003.
[13] M. J. Lancaster, J. S. Hong, D. Jedamzik, R. B. Greed, "Superconducting passive microwave components for mobile communications", in *Conference on the Physics and Engineering of Millimeter Wave and Submillimeter Waves*, vol. 1, pp. 82-87, Sept. 1998.
[14] R. R. Mansour, S. Ye, V. Dokas, B. Jolley, G. Thomson, W. C. Tang, C. M. Kudsia, "Design considerations of superconductive input multiplexers for satellite applications", *IEEE Trans. Microwave Theory Tech.*, vol. 44, no. 7, pp. 1213-1228, Jul. 1996.
[15] Y. Z. Li, M. J. Lancaster, F. Huang, N. Roddis, "Superconducting microstrip wide band filter for radio astronomy", in *2003 IEEE MTT-S Int. Microwave Symp.*, vol. 1, pp. 551-554, Jun. 2003.

[16] M. J. Lancaster, F. Huang, A. Porch, B. Avenhaus, J. S. Hong, D. Hung, "Miniature superconducting filters", *IEEE Trans. Microwave Theory Tech*., vol. 44, no. 7, pp. 1339-1346, Jul. 1996.
[17] H. T. Su, F. Huang, M. J. Lancaster, "Compact quasi-lumped element HTS Microwave Filters", in *2001 IEEE MTT-S Int. Microwave Symp.*, pp. 1985-1988, 2001.
[18] R. J. Dinger, D. R. Bowling, A. M. Martin, "A survey of possible passive antenna applications of high-temperature superconductors", *IEEE Trans. Microwave Theory Tech.*, vol. 39, no. 9, pp. 1498-1507, 1991
[19] L. L. Lewis, G. Koepf, K. B. Bhasin, M. A. Richard, "Performance of TlCaBaCuO 30GHz 64 element antenna array", *IEEE Trans. Appl. Supercond.*, vol. 3, pp. 2844-2847, 1993.
[20] J. S. Martens, V. M. Hietala, D. S. Ginley, C. P. Tigges, T. A. Plut, J. K. Truman, E. K. Track, K. H. Young, R. T. Young, "HTS-based switched filter banks and delay lines", *IEEE Trans. Appl. Supercond.*, vol. 3, no. 1, pp. 2824-2827, Mar. 1993.
[21] F. Huang, B. Avenhaus, M. J. Lancaster, "Lumped-element switchable superconducting filters". *IEE-Proc. Microw. Antennas Propag*., vol. 146, no. 3, pp. 229-233, Jun. 1999.
[22] F. S. Thomson, R. R. Mansour, S. Ye, W. Jolley, "Current density and power handling of high-temperature superconductive thin film resonators and filters", *IEEE Trans. Appl. Supercond.*, vol. 8, no. 2, pp. 84-93, Jun. 1998.
[23] W. G. Lyons, R. S. Withers, "Passive microwave device applications of high T_c superconducting thin films", *Microwave Journal*, pp. 85-102, Nov. 1990.
[24] P. A. Ryan, "High-temperature superconductivity for avionic electronic warfare and radar systems", in *High-T_c microwave superconductors and applications*, Robert B. Hammond, Richard S. Withers, Editors, Proc. SPIE 2156, pp. 2-12, 1994.
[25] D. A. Gandolfo, A. Boornard, L. C. Morris, "Superconductive microwave meander lines", *J. Appl. Phys.*, vol. 39, no. 6, pp. 2657-2660, May 1968.
[26] C. L. Lichtenberg, W. J. Meyers, T. G. Kawecki, A. R. Peltzer, M. S. Johnson, M. Nisenoff, G. E. Price, "The high temperature superconductivity space experiment (HTSSE)", *Applied Superconductivity*, vol. 1, no. 7-9, pp. 1313-1331, 1993.
[27] Y. Nagai, N. Suzuki, Y. Kimachi, O. Michikami, "Novel superconductive delay line process using High-Tc superconducting films", *Jpn. J. Appl. Phys.*, V31, Part 2, No. 3A, pp. L242-L245, 1992.
[28] G. K. G. Hohenwarter, E. K. Track, R. E. Drake, R. Patt, "Forty five nanoseconds superconducting delay lines", *IEEE Trans. Appl. Supercond.*, Vol. 3(1), Part 4, pp. 2804-2807, 1993
[29] K. F. Tsang, W. S. Chan, D. Jing, "High T_c superconductor CPW delay line", *Electronics Letters*, vol. 33, no. 16, pp. 1393-1395, Jul. 1997.
[30] E. K. Track, R. E. Drake, G. K. G. Hohenwarter, "Optically modulated superconducting delay lines", *IEEE Trans. Appl. Supercond*., vol.3, no. 1, pp. 2899-2902, 1993.
[31] G. J. Hofer, H. A. Kratz, G. Schultz, J. Sollner, V. Windte, "High temperature superconductor coplanar delay lines", *IEEE Trans. Appl. Supercond.*, vol. 3, no. 1, pp. 2800-2803, 1993.
[32] L. A. Hornak, M. Hatamian, S. K. Tewksbury, E. G. Burkhardt, R. E. Howard, P. M. Mankiewich, B. L. Straughn, C. D. Brandle, "Experiments with a 31-cm high T_c superconducting thin film transmission line", in *1989 IEEE MTT-S Int. Microwave Sym.*, vol.2, pp. 623-626, 1989.
[33] G. C. Liang, R. S. Wither, B. F. Cole, S. M. Garrison, M. E. Johansson, W. S. Ruby, W. G Lyons, "High-temperature superconducting delay lines and filters on sapphire and thinned $LaAlO_3$ substrates", *IEEE Trans. Appl. Supercond.*, vol. 3, no. 3, pp. 3037-3041, 1993.
[34] W. G. Lyons, R. S. Withers, J. M. Hamm, A. C. Anderson, P. M. Mankiewich, M. L. O'Malley, R. E. Howard, "High Tc superconductive delay line structures, and signal conditioning networks", *IEEE Trans. Mag.*, vol. 27, no. 2, pp. 2932 -2935, Mar. 1991.
[35] Z.-Y. Shen, P. S. W. Pang, W. L. Holstein, C. Wilder, S. Dunn, D. W. Face, D. B. Laubacher, "High Tc superconducting coplanar delay line with long delay and low insertion loss", in *1991 IEEE MTT-S Int. Microwave Sym.*, vol.3, pp. 1235-238, 1991.
[36] S. H. Talisa, M. A. Janocko, D. J. Meier, C. Moskowitz, R. L. Grassel, J. Talvacchio, P. LePage, D. C. Buck, R. S. Nye, S. J. Pieseski, G. R. Wagner, "High-temperature superconducting wide band delay lines", *IEEE Trans. Appl. Supercond.,* vol. 5, no. 2, pp. 2291-2294, 1995.
[37] N. Fenzi, D. Aidnik, D. Skoglund, S. Rohlfing, "Development of high temperature superconducting 100 nanosecond delay line", in *High-T_c microwave superconductors and applications*, Robert B. Hammond, Richard S. Withers, Editors, Proc. SPIE 2156, pp. 143-151, 1994.
[38] D. S. Wu, H. Y Wang, L. P. Hu, C. X. Zhang, B. C. Yang, X. P. Wang, "High-temperature superconducting microwave delay lines", *Physica C*, vol. 282-287, pp. 2525-2526, 1997.
[39] L. C. Bourne, R. B. Hammond, McD. Robinson, M. M. Eddy, W. L. Olson, T. W. James, "Low-loss microstrip delay line in $Tl_2Ba_2CaCu_2O_8$", *Appl. Phys. Lett.*, vol. 56, no. 23, pp. 2333-2335, Jun. 1990.

[40] H. T. Su, Y. Wang, F. Huang, M. J. Lancaster, "Characterizing a Double-Spiralled Meander Superconducting Microstrip Delay Line using a Resonator Technique", in 2004 *IEEE MTT-S International Microwave Symposium*, pp. 135-138, 2004.
[41] H. T. Su, Y. Wang, F. Huang, M. J. Lancaster, "Wideband superconducting microstrip delay line", *IEEE Trans. Microwave Theory Tech.*, vol. 52, no. 11, pp. 2482-2487, Nov. 2004
[42] E. K. Track, G. K. G. Hohenwarter, L. R. Madhavrao, R. Patt, R. E. Drake, M. Radparvar, "Fabrication and characterization of YBCO microstrip delay lines", *IEEE Trans. Magn.*, vol. 27, no. 2, 2936-2939, Mar. 1991.
[43] G. K. G. Hohenwarter, E. K. Track, R. E. Drake, R. Patt, M. Radparvar, "Design and properties of fabricated superconducting microstrip delay lines made with Nb, NbN and YBCO", *Microwave and optical technology letters*, vol. 4, no. 11, pp. 510-516, 1991.
[44] R. W. Klopfenstein, "A transmission line taper of improved design", *Proc. IRE*, pp. 31-35, Jan. 1956.
[45] D. J. Kapolnek, D. L. Aidnik, G. Hey-Shipton, T. W. James, N. O. Fenzi, D. L. Skoglund, B. J. L. Nilsson, "Integral FMCW radar incorporating an HTSC delay line with user-transparent cryogenic cooling and packaging", *IEEE Trans. Appl. Supercond*., vol. 3, no. 1, pp. 2820-2823, Mar. 1993.
[46] T. C. L. G. Sollner, W. G. Lyons, D. R. Arsenault, A. C. Anderson, M. M. Seaver, R. R. Boisvert, R. L. Slattery, "Superconducting cueing receiver for space experiment", *IEEE Trans. Appl. Supercond.*, vol. 5, no. 2, pp. 2071-2074, Jun. 1995.
[47] W. Hattori, T. Yoshitake, S. Tahar, "A re-entrant delay-line memory using a $YBa_2Cu_3O_{7-\delta}$ coplanar delay-line", *IEEE Trans. Appl. Supercond.*, vol. 9, no. 2, pp. 3829-3832, Jun. 1999.
[48] G. C. Liang, C. F. Shih, R. S. Withers, B. F. Cole, M. E. Johansson, "Space-qualified superconductive digital instantaneous frequency-measurement subsystem", *IEEE Trans. Microwave Theory Tech.*, vol. 44, no. 7, pp.1289-1299, Jul. 1996
[49] F. Huang, "Thin film HTS delay line filters", *Cryogenics*, vol. 37, no. 10, pp. 671-679, 1997.
[50] W. G. Lyons, D. R. Arsenault, A. C. Anderson, T. C. L. Gerhard Sollner, P. G. Murphy, M. M. Seaver, R. R. Boisvert, R. L. Slattery, R. W. Ralston, "High-T_c superconductive wideband compressive receivers", *The Lincoln Laboratory Journal*, vol. 9, no. 1, pp. 33-64, 1996.
[51] R. S. Withers, A. C. Anderson, J. B. Green, S. A. Reible, "Superconductive delay-line technology and applications", *IEEE Trans. Magn.*, vol. 21, no. 2, pp. 186-192, Mar. 1985.
[52] H. C. H. Cheung, F. Huang, M. J. Lancaster, R. G. Humphreys, N. G. Chew, "Improvements in superconducting linear phase microwave delay line bandpass filters", *IEEE Trans. Appl. Supercond.*, vol. 5, no. 2, pp. 2675-2677, Jun. 1995.
[53] R. S. Withers, A. C. Anderson, P. V. Wright, S. A. Reible, "Superconductive tapped delay lines for microwave analog signal processing", *IEEE Trans. Magn*., vol. 19, no. 3, pp. 480-484, May 1983.
[54] P. V. Wright, H. A. Haus, "A closed form analysis of reflective array gratings", *IEEE Ultrasonics Symposium Proceedings*, New York, pp. 282-287, 1980.
[55] F. Huang, "Low loss quasitransversal microwave filters with specified amplitude and phase characteristics", *IEE Proceedings-H*, vol. 140, no. 6, pp. 433-440, Dec. 1993.
[56] H. C. H. Cheung, M. Holroyd, F. Huang, M. J. Lancaster, B. Aschermann, M. Getta, G. Muller, H. Schlick, "125% bandwidth superconducting chirp filters", *IEEE Trans. Appl. Supercond.*, vol. 7, no. 2, pp. 2359-2362, Jun. 1997.
[57] Y. Wang, H. T. Su, F. Huang, M. J. Lancaster, "Wideband superconducting coplanar delay lines", *IEEE Trans. Microwave Theory Tech.*, accepted for publication, Jul. 2005.

Chapter 3 Superconductors and Superconductivity at Microwave Frequencies

3.1 High-temperature superconductor materials

The term "high-temperature superconductor (HTS)" usually refers to the category of superconductors with transition temperatures (T_c) higher than 77K. This would be high enough for operating in liquid nitrogen - the commonly available coolant, but still much lower than room temperature. To date, the record T_c at ambient pressure is 138 K, exhibited by a thallium-doped, mercuric cuprate (Hg-Tl-Ba-Ca-Cu-O). The majority of the applications of HTS at microwave frequencies employ thin films (less than 1μm thick) of $YBa_2Cu_3O_7$ (YBCO) or $Tl_2Ba_2CaCu_2O_8$ (TBCCO), both with layered crystalline structures including copper oxide planes and chains. Some of the important parameters for these two HTS materials are listed in Table 3-1. Both materials have low surface resistances. Using established fabrication techniques, large-area high-quality films can be deposited on appropriate dielectric substrates with a standard size of 2-3 inches in diameter.

The substrate of HTS thin film must have suitable crystalline structures for epitaxial growth of HTS films. It should also have excellent microwave properties, such as low loss tangent and stable dielectric constant. As far as the miniaturisation of the device is concerned, a moderate or high dielectric constant is preferred. The most used three substrates for microwave applications are listed in Table 3-2. Sapphire (Al_2O_3) has the lowest dielectric loss. But its dielectric properties are anisotropic. As mentioned in Chapter 2, for HTS, this means the circuit deposited on it may not be oriented randomly. Therefore, special care must be taken in the design. $LaAlO_3$ has a large dielectric constant (~23). Because of the large dielectric constant, it can provide the longest possible delay and shortest half wavelength, so it is widely used in HTS delay lines and some other devices where the primary concern is miniaturisation. But the twin-structure in $LaAlO_3$ makes its dielectric constant vary slightly, which could reduce the fabrication yield of HTS components based on precise designs, such as filters. MgO is widely used as the substrate for HTS filters. Its mechanical strength is not so good as for the other two substrates, because MgO is more fragile and it can cleave.

Table 3-1 HTS materials for microwave applications[1]

	$YBa_2Cu_3O_7$	$Tl_2Ba_2CaCu_2O_8$
T_c(K) in thin-film	85-93	100-106
J_c(A/cm^2)	~10^6	~10^6
R_s(mΩ)@77K,10GHz*	0.1-0.5	0.1-0.5
Penetration depth λ(nm)	150	200

*Copper: R_s=8.7mΩ@77K and 26.1mΩ@300K at 10 GHz.

Table 3-2 Substrates for microwave applications of HTS thin films (extracted from Table 2.1 in [1]).

	Crystal structure	Growth surface	ε_r@300K	tanδ@77K,10 GHz
$LaAlO_3$	Rhombohedral	(110)	24	0.76×10^{-5}
MgO	Cubic	(100)	10	0.62×10^{-5}
Al_2O_3	Rhombohedral Hexagonal	(110) (1$\bar{1}$02)	9.3 ($\perp c$)* 11.6 ($//c$)*	3.8×10^{-8} (80K)

*c stands for the optic axis of the material.

3.2 Fundamentals of superconductivity

To design superconducting microwave devices, knowledge of the quantum mechanics theory of superconductivity is not essential. But some phenomenological theories would be helpful in understanding the electromagnetic response of the superconductors at microwave frequencies. The classical two-fluid model is simple but effective in establishing the microwave properties of superconductors.

Thermodynamically, the superconducting state is a state with a minimum free energy, when some electrons are condensed into pairs (Cooper pairs) and others (quasiparticles) behave similar to normal electrons. Therefore the carriers in a superconductor consist of both superconducting pairs and normal single-electrons, which forms the concept of the "two-fluid" model - superfluid and normal fluid. In the framework of this model, the complex conductivity of the superconductor can be defined. When this conductivity is combined with the Maxwell's equations, some unique electromagnetic features of superconductors can be derived. Among them is the Meissner effect, which distinguishes superconductors not only from normal conductors but also from ordinary perfect conductors[2]. Material parameters such as penetration depth, surface impedance and kinetic inductance can be defined. The formulation of the two-fluid model will be described next. Derivations that follow are based on the book by M. J. Lancaster[3].

3.2.1 Two-fluid model

The derivation of the two-fluid equations starts from applying Newton's motion law to a superconductive Cooper pair and a single normal electron:

$$2m\frac{d\vec{v}_s}{dt} = -2e\vec{E}, \qquad \textbf{Equation 3-1}$$

$$m\frac{d\vec{v}_n}{dt} = -e\vec{E} - m\frac{\vec{v}_n}{\tau}. \qquad \textbf{Equation 3-2}$$

where $\vec{v}_s$ and $\vec{v}_n$ are the velocities of the superconductive pair and the normal electron, e and m are the charge and mass of an electron. $\vec{E}$ is the applied electrical field. The fundamental difference between the two equations is the term $-m\vec{v}_n/\tau$, which represents the viscous loss due to the scattering of normal electrons.

Current-density vectors corresponding to the two fluids are

$$\vec{J}_s = -n_s e\vec{v}_s, \qquad \textbf{Equation 3-3}$$

$$\vec{J}_n = -n_n e\vec{v}_n. \qquad \textbf{Equation 3-4}$$

with n_s and n_n the paired and normal electron densities, respectively. The total current density can be associated with the applied electrical field through an effective conductivity σ according to the Ohm's law, i.e.

$$\vec{J} = \vec{J}_s + \vec{J}_n = \sigma\vec{E} \qquad \textbf{Equation 3-5}$$

To find σ, substitute $\vec{v}_s$ and $\vec{v}_n$ in (3-3) and (3-4) into (3-1) and (3-2) respectively, and assume a sinusoidal time dependence $e^{j\omega t}$. The resultant σ is complex and can be expressed as

$$\sigma = \sigma_1 - j\sigma_2 \qquad \textbf{Equation 3-6}$$

where

$$\sigma_1 = \frac{n_n e^2 \tau}{m(1+\omega^2\tau^2)}, \qquad \textbf{Equation 3-7}$$

$$\sigma_2 = \frac{n_s e^2}{\omega m} + \frac{n_n e^2}{\omega m}\frac{\omega^2\tau^2}{(1+\omega^2\tau^2)}. \qquad \textbf{Equation 3-8}$$

The real part σ_1 is the contribution of the normal fluid to resistive loss and the imaginary part σ_2 is the inductive contribution, signifying that energy can be stored in the superconductor as in an inductor without dissipation. For a direct current (ω=0), σ_2 tends to infinity. Therefore, the current bypasses the resistance (real part) and this results in zero resistivity. However, when an alternative current is applied, the two-fluid system will experience finite resistance and inductance. This is why the superconductor loss at microwave frequencies is non-zero.

In most of the practical situations for superconductors, σ_2 is much larger than σ_1. For YBCO at 77K and 10 GHz, σ_2 is ~10^8 S/m whereas σ_1 is ~10^6 S/m. In the following derivation, the approximation $\sigma_2 >> \sigma_1$ will be used all the way through. This is a very good approximation unless the temperature is close to T_c.

3.2.2 Wave equations of superconductors

Combining the two-fluid model with the Maxwell's equations, some unique wave equations for superconductors can be found.

In the extreme case that there is only the superconductive fluid, which is an approximation at low frequencies and low temperatures ($T << T_c$), two important equations, the London equations (firstly introduced by London brothers in 1934), can be derived.

Using (3-1) and (3-3), one can arrive at the first London equation,

$$\Lambda \frac{\partial \vec{J}_s}{\partial t} = \vec{E} \qquad \textbf{Equation 3-9}$$

where $\Lambda = m/(n_s e^2)$ is a constant, related to the penetration depth to be introduced later. Taking the curl of (3-9) and using Faraday's law

$$\nabla \times \vec{E} = -\frac{\partial \vec{B}}{\partial t} \qquad \textbf{Equation 3-10}$$

gives the second London equation

$$\Lambda \nabla \times \vec{J}_s = -\vec{B}. \qquad \textbf{Equation 3-11}$$

More generally, if the superconductor is in two-fluid state ($\vec{J} = \vec{J}_s + \vec{J}_n$), by applying the first London equation (3-9) to the superfluid and the Ohm's relation $\vec{J}_n = \sigma_1 \vec{E}$ to the normal fluid, the wave equation can be expressed as[3]

$$\nabla^2 \vec{E} = \mu\varepsilon \frac{\partial^2 \vec{E}}{\partial^2 t} + \mu\sigma_1 \frac{\partial \vec{E}}{\partial t} + \frac{\mu}{\Lambda}\vec{E}. \qquad \textbf{Equation 3-12}$$

Firstly, for the field not varying with time, the above wave equation is reduced to

$$\nabla^2 \vec{E} = \frac{\mu}{\Lambda}\vec{E}. \qquad \textbf{Equation 3-13}$$

Its plane wave solution is

$$\vec{E} = E_x e^{-z/\lambda_L} \vec{a}_x. \qquad \textbf{Equation 3-14}$$

where z is the penetration distance of the filed into the superconductor. Equation (3-14) indicates that even static electrical field decays exponentially into the superconductor. This is in contrast to the normal conductor, for which full penetration takes place in this case. The characteristic length λ_L of the field penetration is called the London penetration depth,

$$\lambda_L = \sqrt{\frac{\Lambda}{\mu}} = \sqrt{\frac{m}{\mu n_s e^2}}. \qquad \textbf{Equation 3-15}$$

Secondly, for the field varying with time as $e^{j\omega t}$, the wave equation becomes

$$\nabla^2 \vec{E} = j\omega\mu\left(\sigma_1 - j\frac{1}{\omega\Lambda} + j\omega\varepsilon\right)\vec{E} = j\omega\mu[(\sigma_1 - j\sigma_2) + j\omega\varepsilon]\vec{E} \quad \textbf{Equation 3-16}$$

(Similar equation can be derived for $\vec{H}$.) From this wave equation, the general form of penetration depth and surface resistance can be found.

3.2.3 Penetration depth

From the wave equation (3-16), the propagation constant (perpendicular to the superconductor surface) can be written as

$$\gamma = \sqrt{j\omega\mu[(\sigma_1 - j\sigma_2) + j\omega\varepsilon]}, \quad \textbf{Equation 3-17}$$

As the conductive current is much larger than the displacement current in superconductors ($\sigma_2 >> \omega\varepsilon$), $j\omega\varepsilon$ can be neglected. So,

$$\gamma = \alpha + j\beta = \sqrt{j\omega\mu(\sigma_1 - j\sigma_2)}. \quad \textbf{Equation 3-18}$$

Using the approximation $\sigma_2 >> \sigma_1$, the real part of γ becomes

$$\alpha = \sqrt{\omega\mu\sigma_2}, \quad \textbf{Equation 3-19}$$

which is the attenuation coefficient related to the material loss. This attenuation causes an exponential decay of the field in *z*-direction. The amplitude of the decaying wave into the superconductor can be expressed as

$$A = A_0 e^{-\alpha z}. \quad \textbf{Equation 3-20}$$

Similar to the definition of the London depth in (3-15), another characteristic length λ_p can be defined as

$$\lambda_p = \frac{1}{\alpha} = \frac{1}{\sqrt{\omega\mu\sigma_2}}. \qquad \textbf{Equation 3-21}$$

This is a general definition of penetration depth in contrast to the London depth defined for a static field. The counterpart of this "penetration depth" in a normal conductor is the "skin depth"[4]. However, the two have completely different frequency dependencies.

Using the approximation $\omega\tau << 1$ in (3-8) (Ignoring the relaxation effect at microwave frequencies is a good approximation in most practical situations), it can be found that σ_2 is inversely proportional to ω, so λ_p in (3-21) is independent of frequency. This has been experimentally confirmed. Experimental results given in Chapter 8 also imply the frequency independence. This is an important characteristic of superconductors. It means there is no intrinsic dispersion, in contrast to normal conductors. This can be seen from the calculated phase velocities in a parallel-plate transmission line.[1] The parallel-plate transmission line is a pair of conductors with a width of *w*, which is much larger than the separation *d* between the two plates. Each conductor has a thickness of *t*.

If the plates are made of normal conductors, the phase velocity is

$$v_p = \frac{c_0}{1 + \delta/(2d)}, \qquad \textbf{Equation 3-22}$$

c_0 is the light velocity. δ is the skin depth, which depends on ω as $\omega^{0.5}$. Thus the signal is dispersive.

If the plates are superconductors with infinite thickness, then

$$v_p = \frac{c_0}{1 + \lambda_p / d}. \qquad \textbf{Equation 3-23}$$

Because λ_p is independent of frequency, so is v_p. This means there is no dispersion.

If the superconductor plate is thinner than the penetration depth, an interesting property can be seen from its phase velocity:

$$\upsilon_p = \frac{c_0}{\sqrt{1+(\lambda_p/d)\coth(t/\lambda_p)}}, \qquad \textbf{Equation 3-24}$$

where t is the superconductor thickness. In this case, υ_p is much less than the light velocity. This effect of slowing the wave has been employed to design delay lines[5] and filters[6].

3.2.4 Surface impedance of infinitely thick superconductors

Surface impedance is the most important parameter to characterise the superconductor at microwave frequencies. Knowing this value is also useful for the design of superconducting circuits.

Assume a thick superconductor placed against a thick dielectric. A plane wave propagates in z-direction perpendicular to the conductor-dielectric boundary with

$$\vec{E} = E_x e^{-\gamma z}\vec{a}_x, \qquad \textbf{Equation 3-25}$$

$$\vec{H} = E_y e^{-\gamma z}\vec{a}_y. \qquad \textbf{Equation 3-26}$$

Surface impedance, as its name tells, is defined on the surface (boundary) between the superconductor and dielectric. It is a material parameter, which is derived from the boundary condition of the electromagnetic wave. This can be seen from its definition as the ratio between $E_x^{(s)}$ and $H_y^{(s)}$:

$$Z_s = \frac{E_x^{(s)}}{H_y^{(s)}} = \frac{E_x^{(s)}}{\int_{-\infty}^{0} J_x(z)dz}. \qquad \textbf{Equation 3-27}$$

where $E_x^{(s)}$ and $H_y^{(s)}$ are the tangential electrical field and magnetic field at a point on the boundary. At the same time, the surface impedance can be related to the current decaying into the superconductor through the integration $\int_{-\infty}^{0} J_x(z)dz$. J_x varies along the z direction. J_x is in units of A/m^2 and Z_s is in Ohms.

It has been explicated that this surface impedance is equal to the intrinsic impedance of a bulk superconductor[3], which can be obtained in the following way.

Substituting (3-25) and (3-26) into the Faraday's law and assuming the sinusoidal time dependence again, one can correlate E_x with H_y by

$$-\gamma E_x e^{-\gamma z}\vec{a}_y = -\mu(j\omega)H_y e^{-\gamma z}\vec{a}_y .$$

The intrinsic impedance of the medium comes out as

$$Z_s = \frac{E_x}{H_y} = \frac{j\omega\mu}{\gamma} = \sqrt{\frac{j\omega\mu}{\sigma_1 - j\sigma_2}} . \qquad \textbf{Equation 3-28}$$

This is equal to the surface impedance defined by (3-27). Using the approximation $\sigma_2 >> \sigma_1$, Z_s can be split into its real and imaginary parts.

$$Z_s = R_s + jX_s \approx \sqrt{\frac{\omega\mu}{\sigma_2}}\left(\frac{\sigma_1}{2\sigma_2} + j\right) \qquad \textbf{Equation 3-29}$$

The real part (surface resistance) is

$$R_s = \mathrm{Re}(Z_s) = \frac{\sigma_1}{2\sigma_2}\sqrt{\frac{\omega\mu}{\sigma_2}} = \frac{\omega^2\mu^2\sigma_1\lambda_p^3}{2} . \qquad \textbf{Equation 3-30}$$

R_s is proportional to ω^2 provided λ_p is independent of frequency as mentioned before. The measurements in Chapter 8 will look at the frequency dependence of R_s.

The imaginary part (surface reactance) is

$$X_s = \mathrm{Im}(Z_s) = \sqrt{\frac{\omega\mu}{\sigma_2}} = \omega\mu\lambda_p . \qquad \textbf{Equation 3-31}$$

An "internal inductance" can be defined from X_s as

$$L_I = \mu\lambda_p . \qquad \textbf{Equation 3-32}$$

This inductance is attributed to two energy-storage mechanisms: the kinetic energy of the electron flow and the penetration of the magnetic field. At low temperature, these two mechanisms have similar contributions to the energy of the system. As the temperature approaches T_c, normal carriers outnumber the superconducting carriers, and the kinetic energy decreases significantly while the magnetic energy dominates. Another situation when the equal energy contribution fails is the case of a superconductor thin film with a thickness t comparable to λ_p[7]. As the ratio t/λ_p becomes smaller, the magnetic inductance decreases, whereas the kinetic inductance, together with the total internal inductance, increases significantly.

The internal inductance is usually much smaller than the external inductance of the transmission media. But in certain circumstances, such as for a superconductor with a thickness less than the penetration depth, the internal inductance becomes important. This can be seen later in (3-36). The slow-wave effect mentioned in (3-24) is due to this inductance.

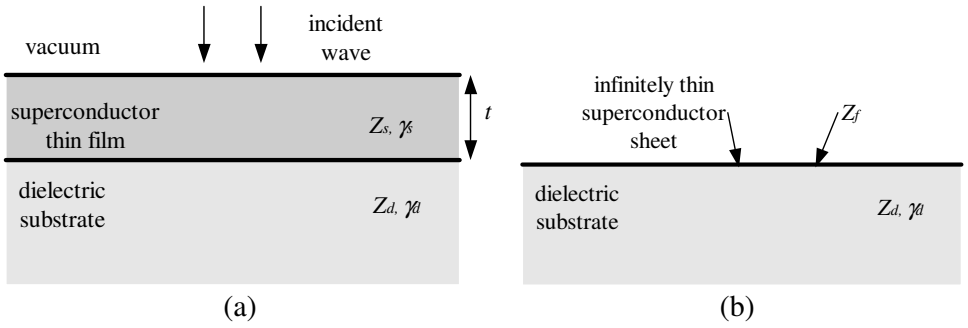

Figure 3.1 (a) Superconductor thin film with a finite thickness and an intrinsic impedance Z_s; (b) the equivalent configuration with an infinitesimal film thickness and an effective surface impedance Z_f.

3.2.5 Effective surface resistance of superconductor thin films

The previous analysis assumes an infinitely thick superconductor. As far as thin-film application is concerned, the effect of finite thickness should be taken into account. In certain circumstances, this may lead to the appearance of some special properties, as mentioned in the context of (3-24) and (3-32). The following analyses will find out when a superconductor

film behaves more like a bulk (the thick-superconductor case) and when it does not (the thin-film case).

The effective surface impedance Z_f of thin films can be treated as an input impedance of a layered structure as shown in Figure 3.1(a). Z_s (Z_d) and γ_s (γ_d) are the intrinsic impedance and propagation constant of the superconductor (dielectric substrate). t is the thickness of the thin film. Then,

$$Z_f = Z_s \frac{Z_d + Z_s \tanh(\gamma_s t)}{Z_s + Z_d \tanh(\gamma_s t)} \qquad \textbf{Equation 3-33}$$

Assuming that both the real and imaginary part of the superconductor surface impedance are much less than those of the substrate, and the film is not too thin, i.e.

$$Z_d \tanh(\gamma_s t) >> Z_s \qquad \textbf{Equation 3-34}$$

Z_f can be simplified to

$$Z_f = Z_s \coth(\gamma_s t). \qquad \textbf{Equation 3-35}$$

Hence, the superconducting film in Figure 3.1(a) can be equalised to an infinitely thin sheet with effective surface impedance Z_f as shown in Figure 3.1(b). Again, using the approximation $\sigma_2 >> \sigma_1$, Z_f can be split into its real and imaginary parts as

$$Z_f = R_f + jX_f = R_s \left[\coth\left(\frac{t}{\lambda_p}\right) + \frac{t}{\lambda_p} \frac{1}{\sinh^2\left(\frac{t}{\lambda_p}\right)} \right] + jX_s \coth\left(\frac{t}{\lambda_p}\right) \qquad \textbf{Equation 3-36}$$

where $Z_s = R_s + jX_s$. The effective surface resistance R_f and the effective surface reactance X_f from (3-36) are plotted against the ratio t/λ_p in Figure 3.2.

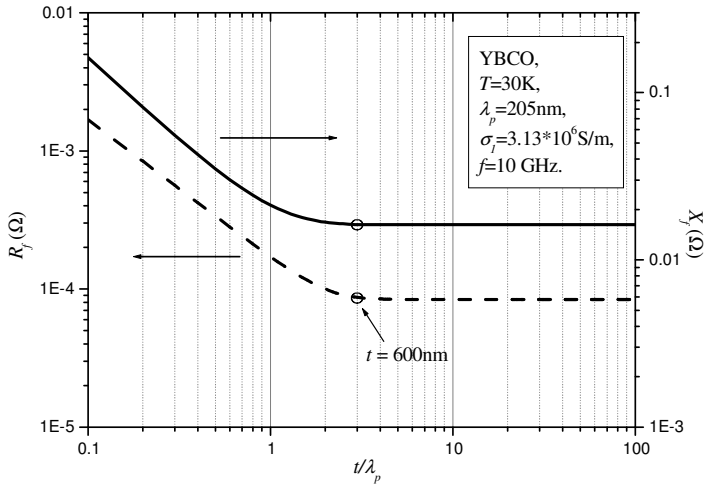

Figure 3.2 The effective surface resistance and surface reactance versus the ratio between the film thickness and penetration depth, calculated using (3-36).

If $t<<\lambda_p$, $X_f = X_s \coth(t/\lambda_p) >> X_s$. This means the effective inductance of the thin film is much larger than the intrinsic inductance when the film is much thinner than the penetration depth. This effect can be observed in a trilayer structure: a thin superconducting film, a thin dielectric layer and another thin superconducting film. Some kinetic-inductance superconducting devices are based on this. If $t>>\lambda_p$, Z_f is reduced to Z_s, the intrinsic impedance of an infinitely thick superconductor.

For the 600 nm thick YBCO film used in this work, assuming λ_p of 205nm at 30K[8], the ratio t/λ_p lies in the flat part of the graph in Figure 3.2. Hence, in this case the film behaves effectively like a bulk material. Its effective surface impedance can be approximated by Z_s. If $t/\lambda_p < 2$, the effect of finite thickness is important and equation (3-36) applies.

3.2.6 Comparison of the formulas for some major physical properties between normal conductors and superconductors

Table 3-3 summarises several important formulas for superconductors in comparison with those for normal conductors.

Table 3-3 Comparison between normal conductors and superconductors ($\sigma_2 >> \sigma_1, \sigma >> \omega\varepsilon$)

	Normal conductors	Superconductors
Conductivity σ	Real σ_1	Complex $\sigma_1 - j\sigma_2, (\sigma_2 = 1/\mu\omega\lambda_p^2)$
Penetration depth *or* Skin depth	$\delta = \sqrt{2/(\omega\mu\sigma_1)} \propto \omega^{-0.5}$	$\lambda_p \propto \omega^0$
Propagation constant γ	$(1-j)/\delta$	$\sqrt{\omega\mu\sigma_2}[1 + j\sigma_1/(2\sigma_2)]$
Surface resistance R_s (bulk)	$\sqrt{\mu\omega/(2\sigma_1)} \propto \omega^{0.5}$	$\omega^2\mu^2\sigma_1\lambda_p^3/2 \propto \omega^2$
Surface reactance X_s (bulk)	$\sqrt{\mu\omega/(2\sigma_1)} \propto \omega^{0.5}$	$\omega\mu\lambda_p \propto \omega$
Effective surface resistance R_f (film)	$R_s \dfrac{\coth(t/\delta)\cdot\tan^{-1}(t/\delta)+1}{\coth(t/\delta)+\tan^{-1}(t/\delta)}$ $t >> \delta, \quad \mu\omega\delta/2 = (\sigma\delta)^{-1}$ $t << \delta, \quad (\sigma t)^{-1}$	$R_s[\coth(t/\lambda_p)+(t/\lambda_p)\sinh^{-2}(t/\lambda_p)]$ $t >> \lambda_p, \quad \omega^2\mu^2\sigma_1\lambda_p^3/2$ $t << \lambda_p, \quad \omega^2\mu^2\sigma_1\lambda_p^4/t$
Effective surface reactance X_f (film)	$X_s \dfrac{\coth(t/\delta)\cdot\tan^{-1}(t/\delta)+1}{\coth(t/\delta)+\tan^{-1}(t/\delta)}$ $t >> \delta, \quad \mu\omega\delta/2$ $t << \delta, \quad \mu\omega t/2$	$X_s \coth(t/\lambda_p)$ $t >> \lambda_p, \quad \omega\mu\lambda_p$ $t << \lambda_p, \quad \omega\mu\lambda_p^2/t$

3.2.7 Temperature dependence

In the two-fluid model, the densities of the superconducting and normal electrons vary as temperature changes:

$$n_n = n(T/T_c)^4, \; n_s = n\left[1-(T/T_c)^4\right] \qquad \textbf{Equation 3-37}$$

where $n=n_s+n_n$ is the total electron density. From (3-7), (3-8), and (3-21), the temperature dependences of the complex conductivity and penetration depth can be derived. The temperature dependence of the penetration depth is particularly important as it is directly related to the surface resistance and reactance through (3-30) and (3-31).

Different models have given different values of N for the dependence of λ_L on the reduced temperature in the form of $(T/T_c)^N$. For a strongly coupled superconductor, the two-fluid model is a good approximation, which gives

$$\lambda_L(\lambda_0, T) = \frac{\lambda_0}{\sqrt{1-(T/T_c)^4}} \qquad \textbf{Equation 3-38}$$

where λ_0 is the penetration depth at zero Kelvin.

For a clean, weakly coupled superconductor, $\lambda_L(T)$ can be well described by the BCS theory:

$$\lambda_{BCS}(\lambda_0, T) = \frac{\lambda_0}{\sqrt{1-(T/T_c)^{3-T/T_c}}} \qquad \textbf{Equation 3-39}$$

Whereas, according to experimental results for YBCO, $\lambda_L(T)$ can be best expressed by[9,10]

$$\lambda_{ph}(\lambda_0, T) = \frac{\lambda_0}{\sqrt{1-(T/T_c)^2}}. \qquad \textbf{Equation 3-40}$$

The change of the penetration depth affects the internal inductance and surface resistance of the superconductor. For a transmission line, this causes the variation of insertion loss and propagation velocity with temperature. For a resonator, it causes the variation of quality factor and the shift of resonant frequency with temperature.

For instance, the fractional frequency shift for a HTS transmission line resonator can be given by (g_1 is a function of the resonator geometry and the penetration depth)[9]

$$\frac{\Delta f(T)}{f(T)} = \frac{1}{2}\frac{\Delta\varepsilon_r}{\varepsilon_r} + \frac{\Delta l}{l} + \frac{1}{2g_1(\lambda_p)}\frac{\partial g_1(\lambda_p)}{\partial \lambda_p}\Delta\lambda_p. \qquad \textbf{Equation 3-41}$$

According to this relation, besides the change of the penetration depth λ_p, the variation of the dielectric constant ε_r and the thermal expansion of the resonator also have some contribution. However, they are insignificant compared with the last term.[9] Therefore, the fractional frequency shift is largely proportional to the change of the penetration depth.

$\Delta f/f$ can also be used to check whether the penetration depth is independent of frequency. Basically, the last term in (3-41) is proportional to $\Delta\ln\left[g_1(\lambda_p)\right]$. Provided the change of the resonator geometry with temperature is negligible, $\Delta\ln\left[g_1(\lambda_p)\right]$ is solely determined by the variation of the penetration depth. So, if $\Delta f/f$ does not change at different resonant

frequencies, it indicates that λ_p is frequency independent. This will be looked at by characterising a number of resonances at different temperatures in Chapter 8.

3.3 Characterisation of surface resistance

There are many methods to measure the surface resistance (R_s) of HTS thin films. Most of them are based on resonators of different configurations.

Cavity, parallel plate and dielectric resonator techniques are used to measure R_s of unpatterned films. Because their geometric structures are usually simple, the electromagnetic field distribution can be solved and the geometric factors can be accurately determined in order to extract R_s from measured quality factors (Q). The dielectric resonator technique has become an industrial standard for measuring R_s of as-grown (unpatterned) HTS films. The value obtained is a useful assessment of the film quality.

R_s can also be measured by planar transmission line resonators. The resultant surface resistance, however, will be that of the patterned film. As most of the HTS microwave circuits are made of patterned structures, R_s measured in this way is more closely related to the real device. It should be noted that the patterning process may have some impact on the quality of the original film. This is partly due to the interaction of HTS with wet etchants or ion beams, and partly due to the damage of the edge. Therefore, different R_s-values may be expected from patterned and unpatterned films. In transmission line resonators, current distribution is not uniform. Current crowding occurs at the edges of the conductors. This must be taken into account in order to define the geometric factors relating R_s to the measured Q. In many circumstances, other factors such as film thickness or edge shape may further complicate the acquisition of R_s[11]. In Chapter 8, characterisations of R_s using coplanar line resonators will be discussed.

Using resonator techniques, the films are normally characterised at one or a few frequencies due to the limitations in resonator size and ability to accurately measure many modes over a wide frequency range. The experimental justification of the frequency-dependence of R_s is usually generalised from these scattered data. Certain consistency has been shown between various methods to conform to the ω^2-dependence predicted by (3-30) in the two-fluid model.[12] Non-square relations such as $\omega^{1.8}$ and $\omega^{2.3}$ were also reported[13,14]. It is understood

that different measurements may not give consistent R_s-values due to different film qualities or varied acquisition procedures.

Theoretically, a continuous profile of the frequency dependence can be established by measuring a non-resonant transmission line. This has been investigated by using low-temperature probe station.[15] One of the disadvantages of this method is the inclusion of the input/output connections. This may incur extra contact loss, which is not repeatable in different runs of the measurements and also difficult to characterise quantitatively. Another disadvantage is its difficulty in accurate calibration, which is too often a challenge to low-temperature transmission measurements.

To yield a continuous profile of frequency dependence using the resonator techniques, a resonator with a very low resonant frequency has to be used. It is possible to make such a resonator from a long HTS transmission line. This has been done in this thesis by adapting the 25ns delay line to a 20 MHz resonator. More than 1000 harmonics of this resonator can be produced from 20 MHz to 20 GHz at an interval of 20 MHz. Although this is not a precise method due to some limitations discussed in Chapter 8, it provides complementary information to the scattered data, giving a picture over a wide frequency range. Besides its usage in the wideband measurement, there is also great interest in the characterisation at the low frequencies. An application background in magnetic resonance imaging (MRI) devices was discussed in [16]. This usually involves a resonator working below 100 MHz. A long transmission-line resonator has to be employed in this case.

---

[1] Z.-Y. Shen, *High-temperature superconducting microwave circuits*, Artech, 1994.
[2] T. P. Orlando, K. A. Delin, *Foundations of applied superconductivity*, Addison-Wesley, 1990.
[3] M. J. Lancaster, *Passive microwave device applications of high-temperature superconductors*, Cambridge University Press, Cambridge, UK, 1997.
[4] H. A. Wheeler, "Formulas for the skin effect", *Proceedings of the I.R.E.*, pp. 412-424, Sept. 1942.
[5] J. M. Pond, J. H. Claassen, W. L. Carter, "Measurements and Modeling of Kinetic Inductance Microstrip Delay Lines", *IEEE Trans. Microwave Theory Tech.*, vol. 35, no. 12, pp. 1256-1262, Dec. 1987.
[6] K. R. Carroll, J. M. Pond, E. J. Cukauskas, "Superconducting kinetic-inductance microwave filters", *IEEE Trans. Appl. Supercond.*, vol. 3, no. 1, pp. 8-16, Mar. 1993.
[7] D. W. Huish, *Microwave and optical reflectance studies of YBCO films*, PhD Thesis, The University of Birmingham, 2003.
[8] J. C. Booth, C. L. Holloway, "Conductor loss in superconducting planar structures: calculations and measurements", *IEEE Trans. Microwave Theory Tech.*, vol. 47, no. 6, pp. 769-774, Jun. 1999.
[9] A. Porch, M. J. Lancaster, R. G. Humphreys, "The coplanar resonator technique for determining the surface impedance of $YBa_2Cu_3O_{7-\delta}$ thin film", *IEEE Trans. Microw. Theo. Tech.*, vol. 43, no. 2, pp. 306-314, 1995.
[10] S. Cho, "Inductance measurements in $YBa_2Cu_3O_{7-x}$ thin films", *Supercond. Sci. Tech.*, vol. 10, pp. 594-597, 1997.

[11] C. L. Holloway, E. F. Kuester, "A quasi-closed form expression for the conductor loss of CPW lines, with an investigation of edge shape effects", *IEEE Trans. Microwave Theory Tech.*, vol. 43, no. 12, pp. 2695-2701, Dec. 1995.

[12] W. L. Holstein, L. A. Parisi, Z.-Y. Shen, C. Wilker, M. S. Brenner, J. S. Martens, "Surface Resistance of Large Area $Tl_2Ba_2CaCu_2O_8$ Thin Films at Microwave and Millimeter Wave Frequencies Measured by Three Non-Cavity Techniques", *J. Supercond.*, vol. 6, pp. 191-200, 1993

[13] M. S. DiIorio, Alfredo C. Anderson, B. -Y. Tsaur, "rf surface resistance of Y-Ba-Cu-O thin films", *Phys. Rev. B*, vol. 38, no. 10, pp. 7019–7022, Oct. 1988

[14] J. P. Carini, A. M. Awasthi, W. Beyermann, G. Grüner, T. Hylton, K. Char, M. R. Beasley, A. Kapitulnik, "Millimeter-wave surface resistance measurements in highly oriented $YBa_2Cu_3O_{7-\delta}$ thin films", *Phys. Rev. B*, vol. 37, no. 16, pp. 9726–9729, Jun. 1988

[15] J. C. Booth, J. A. Beall, D. C. DeGroot, D. A. Rudman, R. H. Ono, J. R. Miller, M. L. Chen, S. H. Hong, Q. Y. Ma, "Microwave characterization of coplanar waveguide transmission lines fabricated by ion implantation patterning of $YBa_2Cu_3\ O_{7-\delta}$", *IEEE Trans. Appl. Supercond.*, vol. 7, no. 2, pp. 2780-2783, Jun. 1997.

[16] J. C. Ginefri, L. Darrasse, P. Crozat, "Comparison of radio-frequency and microwave superconducting properties of YBaCuO dedicated to magnetic resonance imaging," *IEEE Trans. Appl. Supercon.*, vol. 9, no. 4, pp. 4695-4701, Dec. 1999.

Chapter 4 Coplanar transmission lines

This chapter mainly employs the quasi-TEM theory of transmission lines to investigate the characteristic impedance, loss, and coupling of both coplanar waveguide (CPW) and conductor-backed coplanar waveguide (CBCPW). Dimensions of the 50 Ω coplanar delay lines are defined. The variations of the transmission loss and cross coupling between adjacent lines with geometric configurations and frequencies are estimated. The conductor loss of CBCPW is formulated based on the incremental-inductance method to look at the loss increase due to the presence of the conductor backing. The parasitic modes in the coplanar structures are also described.

4.1 Transmission line overview

Microstrip, stripline and coplanar waveguide are the most commonly used transmission lines both in normal conductor and superconductor microwave circuits, as shown in Figure 4.1(a,b,c)[1,2,3].

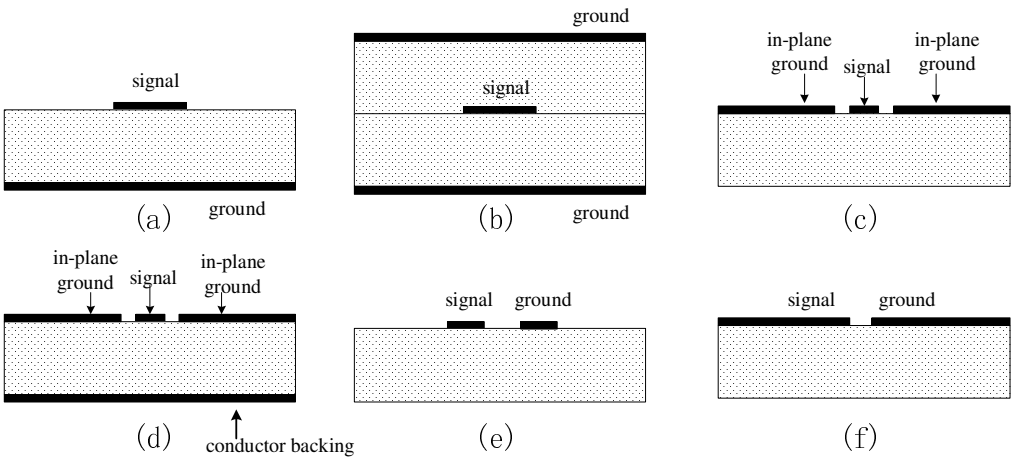

Figure 4.1 Main transmission line types: (a) microstrip, (b) stripline, (c) coplanar waveguide (CPW), and three types of modified coplanar structure: (d) conductor-backed coplanar waveguide (CBCPW), (e) coplanar stripline (CPS), (f) slotline.

Microstrip is most likely the first choice of many devices because of its ease and flexibility in fabrication and packaging. It also has the lowest achievable conductor loss among these three transmission lines. However, it has higher radiation and has more electromagnetic field

overlapping between adjacent lines due to its open structure. The latter results in relatively strong cross coupling between parallel microstrip lines, and therefore makes it not a preferred structure for delay lines because cross coupling is especially detrimental in the application. Microstrip propagates a non-TEM mode and has some mode dispersion.

Stripline has a pure TEM propagation mode. Because the even- and odd-mode velocities are the same in a coupled stripline structure, it has negligible forward coupling and therefore good isolation. In fabrication, a stripline is made from two wafers, which are then clamped together in precise alignment and with appropriate pressure. This sandwiched structure suffers from the difficulty in eliminating air gaps between the two wafers, which effectively makes the dielectric inhomogeneous. This often results in strong coupling and increased reflections. The transition and connection between the stripline and coaxial connectors should also be carefully implemented. A stripline-to-coplanar transition may be needed to facilitate the connection with coaxial connectors.

For both microstrip and stripline, as long as the substrate thickness is fixed, the line width can not be arbitrarily chosen for certain characteristic impedance, whereas coplanar waveguide (CPW) still has some degrees of freedom: the strip width and the slot width. By keeping an appropriate slot-to-strip ratio, different line widths can be chosen for a specific characteristic impedance. This offers the flexibility in optimising the circuit density. Potentially very compact devices can be realised. But the compactness has to be traded off against a higher loss level, as narrower line width causes greater current density and therefore higher conductor loss. Coplanar waveguide also features the lowest cross coupling among these three transmission media, partly due to the screening effect of the in-plane grounds (labelled in Figure 4.1(c)), and partly because the line can be made very narrow while retaining a reasonable value of characteristic impedance. However, with the coplanar structure, it is a big problem to achieve pure propagation modes. Slot modes and surface-wave leakage are parasitic and can all be detrimental. Crossover bonding-wires may have to be used to balance the unequal potentials between the in-plane grounds and suppress the slotline modes.

Figure 4.1(d,e,f) are three modified coplanar structures.[1,2] Figure 4.1(e) is the coplanar stripline, which can be regarded as a complementary to the CPW. Figure 4.1(f) is the slotline, composed of two half-plane conductors separated by a gap. Figure 4.1(d) is the conductor-

backed coplanar waveguide (CBCPW). The introduction of the conductor backing increases its mechanical strength because it facilitates mounting of the device on a metal surface, as with microstrip. But this conductor backing could bring parallel-plate modes, which may be established between the upper and lower ground planes unless they are properly interconnected. Experimental results given in Chapter 9 reveal another attractive property of CBCPW to efficiently suppress the parasitic slotline modes. This helps to achieve an excellent wideband transmission without using any bonding wires in the CBCPW delay line.

In this work, both conventional CPW and conductor-backed CPW (CBCPW) are used as the transmission media. Characteristic impedance, loss, cross-coupling, and parasitic modes of both coplanar waveguides are discussed.

4.2 Coplanar waveguides (CPW and CBCPW)

4.2.1 Characteristic impedance and effective permittivity

Although CPW is a non-TEM structure, the quasi-TEM approximation has proved a good representation of its characteristic properties, as long as the slot and strip widths are much smaller than its substrate thickness. In this case, the two coplanar slots can be treated as perfect magnetic walls. So conformal-mapping techniques[4] can be used to calculate the characteristic impedance and effective permittivity.

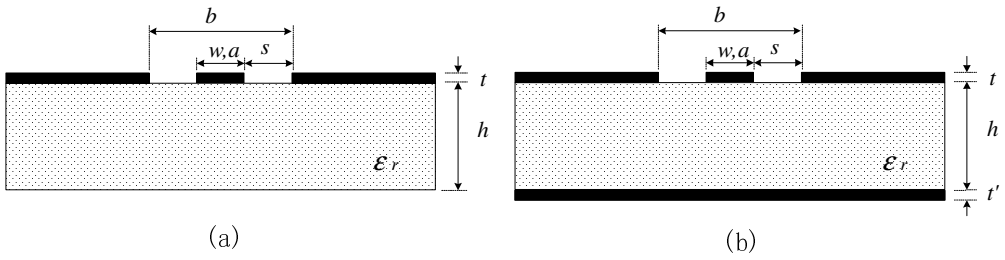

Figure 4.2 Dimensional symbols for coplanar waveguides (a) CPW (b) CBCPW. *w* is the strip width, *s* is the slot width. *b*=*w*+2*s*, *a*=*w*.

Ghione's formulas[7] are adopted to calculate the characteristic impedance of CPW and CBCPW with finite substrate thickness. The effect of upper shielding, which is not shown in Figure 4.2, is included. All the conductors are assumed infinitely thin.

For a CPW as shown in Figure 4.2(a), the characteristic impedance and effective permittivity are given by [7]

$$Z_0 = \frac{60\pi}{\sqrt{\varepsilon_{eff}}} \frac{1}{K(k_2)/K'(k_2) + K(k)/K'(k)} \qquad \textbf{Equation 4-1}$$

$$\varepsilon_{eff} = 1 + (\varepsilon_r - 1) \frac{K(k_1)/K'(k_1)}{K(k_2)/K'(k_2) + K(k)/K'(k)} \qquad \textbf{Equation 4-2}$$

where $K(k)$ is the complete elliptic integral of the first kind, $K'(k) = K(k')$ and $k' = \sqrt{1-k^2}$ .The factors k, k_1, and k_2 are

$$k = a/b, \quad k_1 = \sinh\left(\frac{\pi a}{4.0h}\right) \Big/ \sinh\left(\frac{\pi b}{4.0h}\right), \quad k_2 = \tanh\left(\frac{\pi a}{4.0h_1}\right) \Big/ \tanh\left(\frac{\pi b}{4.0h_1}\right) \qquad \textbf{Equation 4-3}$$

where h_1 is the height of the upper shielding. Its effect is negligible when $h_1 >> s$ and $h_1 >> w+2s$, applicable to all the practical situations in this work.

For a CBCPW as shown in Figure 4.2(b), Z_0 and ε_{eff} can be expressed as[7]

$$Z_0 = \frac{60\pi}{\sqrt{\varepsilon_{eff}}} \frac{1}{K(k_3)/K'(k_3) + K(k_4)/K'(k_4)} \qquad \textbf{Equation 4-4}$$

$$\varepsilon_{eff} = 1 + (\varepsilon_r - 1) \frac{K(k_3)/K'(k_3)}{K(k_3)/K'(k_3) + K(k_4)/K'(k_4)} \qquad \textbf{Equation 4-5}$$

$$k_3 = \tanh\left(\frac{\pi a}{4.0h}\right) \Big/ \tanh\left(\frac{\pi b}{4.0h}\right), \quad k_4 = \tanh\left(\frac{\pi a}{4.0h_1}\right) \Big/ \tanh\left(\frac{\pi b}{4.0h_1}\right). \qquad \textbf{Equation 4-6}$$

Using these equations, the slot width as a function of strip width can be found for the 50Ω CPW and CBCPW lines, with 0.508mm or 1.0mm thick $LaAlO_3$ (ε_r=23.6) substrates, as shown in Figure 4.3.

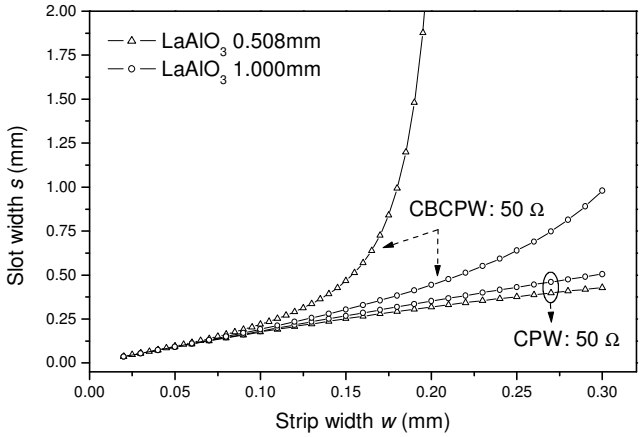

Figure 4.3 The strip-width versus slot-width curves for 50 Ω CPW and CBCPW on 0.508 mm or 1.0 mm $LaAlO_3$ substrates.

In Figure 4.3, when w<0.1mm (then s<0.22mm), both strip width and slot width are much smaller than the substrate thickness, the slot width is linearly proportional to the strip with a ratio (s/w) of 1.85. In this region, the substrate thickness and the presence of the conductor-backing have little effect on the characteristic impedance. As w increases, the effect of the conductor-backing makes the difference between CBCPW and CPW more noticeable. With the same dimensions, CBCPW has smaller characteristic impedance and larger effective permittivity. When w>0.15mm, a dramatic increase of the slot width is required for the 0.508mm thick CBCPW to keep 50Ω. This is because when the slot width becomes comparable to the substrate thickness, more and more electric field concentrates between the strip and conductor backing rather than in the slots. So a parasitic microstrip-mode emerges. If the slot is sufficiently wide, this mode may dominate, and the structure loses the flexibility to keep a certain Z_0 by tuning the slot-to-strip ratio. The achievable impedance turns into that of a microstrip structure, which is 50Ω only if the strip is 0.174 mm. Therefore, a CBCPW strip wider than this cannot maintain 50Ω by any means, which results in the rapid divergence of the curve for the CBCPW line on 0.508mm $LaAlO_3$ in Figure 4.3. It should be borne in mind that the quasi-TEM formulas may lose accuracy if the slot is too wide to be treated as a magnetic wall, so the divergence in Figure 4.3 may also be partly related to the failure of the formulation.

Some calculated parameters for 50Ω CPW and CBCPW are listed in Table 4-1. The results from full-wave Sonnet[5] simulations (infinitely thin conductors are assumed as well) agree well with the conformal-mapping calculations.

Table 4-1 Parameters obtained from conformal-mapping calculations and Sonnet simulations. (h=0.508mm, $LaAlO_3$, ε_r=23.5)

	w(mm)	Calculation method	s(mm)	ε_{eff}	Z_0 (Ω)
CPW	0.02	Conformal mapping	0.0367	12.234	50
		Sonnet[a]	0.036	12.26	49.9
		[6][b]	0.035	-	≈50
	0.04	Conformal mapping	0.0730	12.185	50
		Sonnet[a]	0.074[c]	12.302	50
CBCPW	0.02	Conformal mapping	0.0370	12.263	50
		Sonnet[a]	0.036	12.267	49.9
	0.04	Conformal mapping	0.0754	12.303	50

[a] The cell size in simulations is 0.001 mm, i.e. the line width w is divided into 20 cells for the 0.02mm line and 40 cells for the 0.04mm line. The values are obtained at 2 GHz.
[b] Obtained from a full-wave spectral-domain technique, developed to calculate the characteristic impedance of superconducting CPW. The superconducting film is 400nm thick, the width of the in-plane ground is 0.6mm.
[c] This value is also consistent with the simulation result from 3-dimensional full-wave simulator-HFSS[9].

Although above calculation and simulation techniques are originally for normal conductors, they apply to superconductors very well. A full-wave spectral-domain technique was developed to calculate the characteristic impedance of superconducting CPW.[6] The calculation result is included in Table 4-1 for comparison, which is in good agreement with those from conformal-mapping and Sonnet.

It is well known that conformal mapping is a quasi-static approximation and only rigorously valid at zero frequency. But, many analyses based on this technique yield reasonable results over a wide frequency range, especially for those structures which are not frequency-sensitive. This has been argued in [7]. In this work, the frequency of interest is below 20 GHz. As discussed in the following, since the characteristic impedance of the coplanar waveguides only varies slightly at different frequencies, it should be acceptable to apply some quasi-static results to higher frequencies.

By fitting experimental results, the effective permittivity of CPW as a function of frequency has been given in the form of[8]

$$\varepsilon_{eff}(f) = \left[\sqrt{\varepsilon_{eff,0}} + \frac{\sqrt{\varepsilon_r} - \sqrt{\varepsilon_{eff,0}}}{1 + x \cdot \left(f / f_{TE}\right)^{-y}} \right]^2 . \qquad \textbf{Equation 4-7}$$

where x=182.7 (dependent of dimensions, with w=0.02mm, s=0.04mm, h=0.508mm), y=1.8 (independent of dimensions). $\varepsilon_{eff,0}$ is the effective permittivity in the quasi-static limit. f_{TE} is the cut-off frequency of the lowest-order TE mode,

$$f_{TE} = c_0 / \left(4h\sqrt{\varepsilon_r - 1}\right) \qquad \textbf{Equation 4-8}$$

where c_0 is the velocity of light. For a 0.5mm thick $LaAlO_3$ substrate, f_{TE} is 31.125 GHz.

The frequency-dependence of the effective permittivity has also been investigated by Sonnet simulations, as plotted in Figure 4.4. It agrees well with equation (4-7). The effective permittivity increases by less than 0.2% from 2 to 20 GHz and the characteristic impedance decreases slightly. The unphysical rising in Z_0 at above 30 GHz is a deficiency of the simulator due to the proximity of the frequency corresponding to a half-wavelength. All dispersivity shown from Sonnet simulations is due to the change of field distribution in the dielectric and air. Phase dispersion of the conductors is disregarded as infinitely thin metallization is assumed.

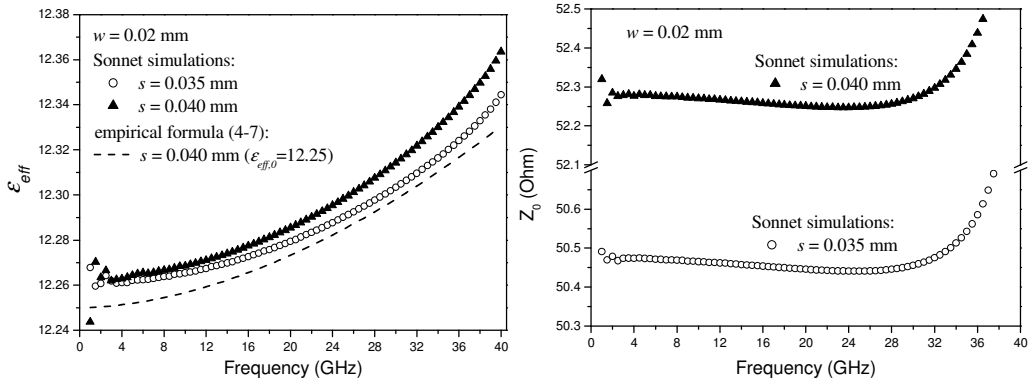

Figure 4.4 Effective permittivity and characteristic impedance as a function of frequency for coplanar waveguides. The simulation is for a 1mm coplanar line. At 40GHz, it is half of a wavelength.

The transmission-line parameters used in the experimental devices are listed in Table 4-2. The 50 Ω line is 0.04 mm wide with a slot of 0.074 mm. This dimension is consistent with

both Sonnet and HFSS[9] simulation results. The selection of the line width is mainly a concern of loss, which will be discussed in Section 4.2.2.

Table 4-2 Parameters of the HTS coplanar waveguides used in the experimental devices.

ε_r	w (mm)	s (mm)	h (mm)	h_1 (mm)	t (nm)
23.6 ($LaAlO_3$)	0.04	0.074	0.508	5	600

4.2.2 Loss

This section is to establish a relation between the attenuation of a coplanar waveguide and the material parameters – loss tangent $tan(\delta)$ and surface resistance R_s. This is through geometric factors (GF_d and GF_c). The dielectric loss (α_d) and conductor loss (α_c) are considered separately. If the attenuation of a transmission line is in dB/m, then

$$\alpha_d = 8.68 \cdot GF_d \cdot \tan(\delta) \cdot f \qquad \textbf{Equation 4-9}$$

$$\alpha_c = 8.68 \cdot GF_c \cdot R_f \qquad \textbf{Equation 4-10}$$

The effective surface resistance R_f rather than R_s is used in (4-10), denoting that this is not necessarily the intrinsic surface resistance of a bulk material. For a thin film conductor, it should be the value including the effect of finite conductor thickness. For a thin film superconductor, the relation between R_f and R_s can be expressed by (3-36). As was discussed in the context of Fig. 3.2, the 600nm YBCO film used in this work behaves more like a thick superconductor and its effective surface resistance R_f approximates to R_s.

The geometric factors (GF_c and GF_d) for the conductor loss and the dielectric loss will be discussed in more details.

4.2.2.1 Conductor loss of CPW

To find the geometric factor GF_c of a transmission line, both numerical and analytical approaches have been developed, mainly based on quasi-static approximation. This is a close approximation for a straight line with very small dispersion. However, when dispersion does exist, the resultant GF_c needs to be carefully interpreted. All the following approaches are

intended for non-dispersive straight lines. Only analytical treatments are presented and actually used in this work.

For normal conductors, the incremental-inductance method[1,10,11] and a direct method based on conformal-mapping of current distribution[12,13] are used to formulate the conductor loss of coplanar waveguides. Based on the incremental-inductance method, the geometric factor of a CPW can be expressed as[1]

$$GF_c^{CPW} = \frac{Z_0 \varepsilon_{eff}}{15\pi^2 \mu_0 c_0} \frac{P'}{s}\left(1+\frac{w}{s}\right) \frac{1+\dfrac{1.25t}{\pi w}+\dfrac{1.25}{\pi}\ln\left(\dfrac{4\pi w}{t}\right)}{\left(2+\dfrac{w}{s}-\dfrac{1.25t}{\pi s}\left(1+\ln\left(\dfrac{4\pi w}{t}\right)\right)\right)^2} \quad \textbf{Equation 4-11}$$

where P' depends on structural parameters and is given in Section A.3.2.1 of Appendix A.

Using the direct method, the geometric factor is[13]

$$GF_c^{CPW} = \frac{1}{16 Z_0 K^2(k)\left[1-(a/b)^2\right]}\left\{\frac{2}{a}\left[\pi+\ln\left[4\pi\frac{a(b-a)}{t(b+a)}\right]\right]+\frac{2}{b}\left[\pi+\ln\left[4\pi\frac{b(b-a)}{t(b+a)}\right]\right]\right\} \quad \textbf{Equation 4-12}$$

(More details of both approaches are in Appendix A.)

Equation (4-12) shows better accuracy[13], which yields smaller geometric factors than the incremental-inductance method does.

For superconductors, the field penetration follows different mechanism from normal conductors. Normal conductors are governed by the frequency-dependent "skin depth" while superconductors by the frequency-independent "penetration depth". To represent the distinct field penetration of superconductors more accurately, the aforementioned two methods need some modifications.

The incremental-inductance method was used on a HTS microstrip by introducing an inductance *L*, combining both the internal and external contributions of the superconducting layers.[14] As a disadvantage pointed out in [1], the accuracy of the incremental-inductance

method significantly depends on the accuracy of L as a function of conductor thickness t, which is very difficult to obtain.

In the direct approach, once the current distribution in the finite-thickness conductor is found using conformal mapping, the attenuation can be determined by calculating the power dissipation as[15]

$$\alpha_c = \frac{R_f}{2Z_0}\frac{\oint_\gamma |J|^2 dl}{I^2} \qquad \textbf{Equation 4-13}$$

where I is the total current carried by the transmission line, J the longitudinal current density on the line, and γ is the contour of the conducting strip chosen as a closed path for the integration. Again, R_f rather than R_s is used here to denote a general situation, which may need to take the finite thickness of the conductor into account. For superconductors, the evaluation of (4-13) should consider the magnetic penetration predicted by the two-fluid model. Holloway's quasi-closed formula is among the few numerical[16] or analytical[17] approaches dealing with superconductor losses in CPW structures. This is adopted in this work. Its geometric factor can be written as[17]

$$GF_c^{CPW} = \frac{1}{16Z_0 K^2(k)\left[1-(a/b)^2\right]}\left\{\frac{2}{a}\ln\left[\frac{a(b-a)}{\Delta(b+a)}\right]+\frac{2}{b}\ln\left[\frac{b(b-a)}{\Delta(b+a)}\right]\right\} \qquad \textbf{Equation 4-14}$$

A "stopping distance"[18] Δ is used here. It is a numerically determined quantity, depending on the material properties (penetration depth λ_p of the superconductive fluid and skin depth δ_{nf} [*] of the normal fluid) and the shape of the conductor (thickness and edge profile)[19]. This is given in Figure 4.5 for a 90^0 edge. A look-up table is also available in [3]. As interpolation is required to find the value of stopping distance using this table, the accuracy is compromised. Fortunately, GF_c^{CPW} is insensitive to the ratio t/Δ. The percentage error of GF_c^{CPW} is 0.2% at 30K and 0.4% at 77K by a unit variation of t/Δ. Based on the structural parameters given in Table 4-2, the stopping distances and geometric factors are found and listed in Table 4-3. By introducing the stopping distance, the geometric factor becomes temperature-dependent.

[*] It is defined similar to the skin depth of a normal conductor as in Table 3-3, i.e. $\delta_{nf} = \sqrt{2/\mu\omega\sigma_1}$. σ_1 is the real part of the complex conductivity.

From 30K to 77K, the ratio t/Δ is halved and the geometric factor decreases by 10.5%.

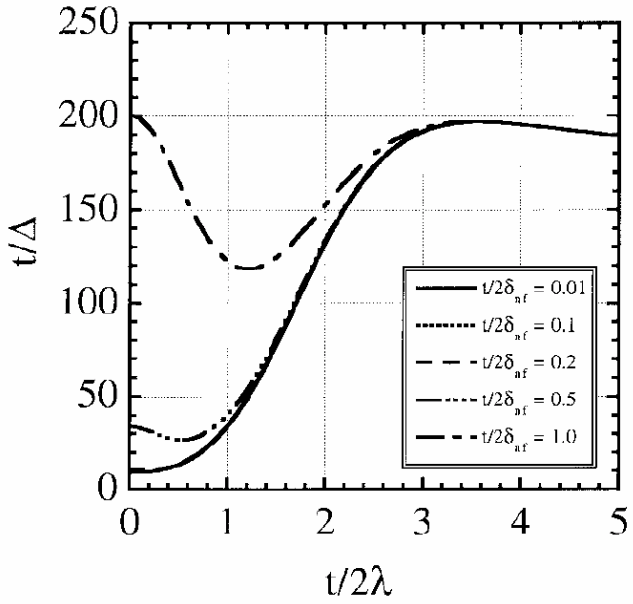

Figure 4.5 The ratio t/Δ plotted as a function of $t/2\lambda$ for various values of $t/2\delta_{nf}$. The curves for $t/2\delta_{nf}$=0.01, 0.1, 0.2 are overlapping. © IEEE [19]

Table 4-3 Stopping distances and geometric factors estimated using Holloway's approach, based on the structural parameters in Table 4-2.

	λ_p (μm)	$t/2\lambda_p$	σ_1 (10^6 S/m)	$t/2\delta_{nf}$ (10GHz)[b]	t/Δ	GF_c ($m^{-1}\Omega^{-1}$)
30 K	0.205[*]	1.463	3.13[*]	0.088	73.448	262.4
60 K	0.232[a]	1.293	<3.13	<0.088	56.66	254.1
77 K	0.316[*]	0.949	<3.13	<0.088	30.712	234.9

[*] material parameters of YBCO given in [19].

[a] As the penetration depths (λ_p) at 30K and 77K are known, the value at 60K is obtained from $\lambda_p = \lambda_0 / \sqrt{1-(T/T_c)^4}$, T_c=87 K.

[b] From Figure 4.5, t/Δ is not sensitive to $t/2\delta_{nf}$ when $t/2\delta_{nf}$<0.2. According to [19], this is the case for $\lambda_p << \delta_{nf}$, i.e. $\sigma_2 >> \sigma_1$, which applies to most of the good superconductors.

Table 4-4 Geometric factors ($m^{-1}\Omega^{-1}$) obtained by different approaches.*

	Holloway's approach for superconductors	Direct method for normal conductors	Incremental-inductance method for normal conductors
30 K	262.4	305.7	364.4
60 K	254.1		
77 K	234.9		

*Parameters used in the calculation of geometric factors are Z_0=50 Ω, ε_{eff}=12.25 and those in Table 4-2.

Holloway's formula has the ability to deal with arbitrary conductor thickness and different shapes of the conductor edges. When $\Delta = t/(4\pi e^{\pi})$, the quasi-closed form (4-14) is reduced

to the closed form (4-12) given in [12] and [13]. Generally, Holloway's approach gives smaller geometric factors than (4-11) and (4-12) as shown in Table 4-4.

Assuming R_f=R_s, the attenuations calculated from (4-10) and (4-14) are plotted in Figure 4.6 for different widths of CPW lines. The loss is proportional to the surface resistance and inversely proportional to the line width. In the literature, R_s of YBCO ranges from 80 μΩ to 250 μΩ at 10 GHz. Based on a value of 110 μΩ (77K, 7.95GHz) given by [20], a 0.02mm wide, 50ns delay line has an insertion loss of 12.4dB at 18 GHz. For a 0.04mm line, this loss is reduced to 6.7dB at a cost of a less compact circuit. Aiming at a 50ns delay line with less than 8dB insertion loss and also taking into account the circuit size, the 0.04mm line width was chosen for the experimental device.

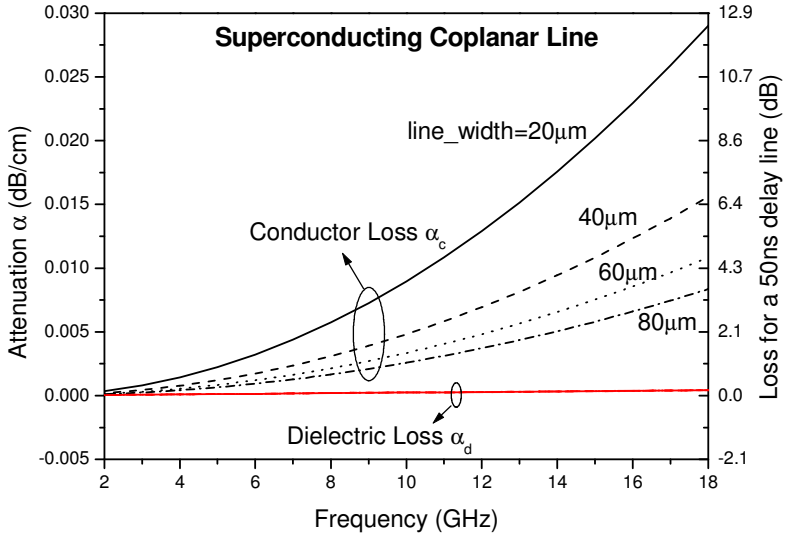

Figure 4.6 Calculated conductor loss by (4-14) and dielectric loss by (4-15) for coplanar waveguides with different line widths. Here R_s=110 μΩ (77K, 7.95GHz)[20] is used and extrapolated over the frequency range from 2 to 20GHz using quadratic relation $R_s(f)=R_s(7.95)\cdot f^2/7.95^2$, f in GHz.

4.2.2.2 Dielectric loss of CPW

The derivation of the dielectric loss can be found in Section A.2 of Appendix A. The final expression is written as[2]

$$\alpha_d = 8.68 \cdot \frac{\pi}{c_0} \frac{\varepsilon_r}{\varepsilon_r - 1} \frac{\varepsilon_{eff} - 1}{\sqrt{\varepsilon_{eff}}} \tan(\delta) \cdot f \qquad \textbf{Equation 4-15}$$

Due to the small loss tangent (0.76×10^{-5} at 77K, 10GHz[21]) of $LaAlO_3$, the conductor loss will be the main source of insertion loss in LAO/YBCO, as can be seen from Figure 4.6. Only if the dielectric loss tangent amounts to 2×10^{-4}, does its contribution become obvious (0.01dB/cm at 18GHz) and comparable to the conductor loss.

4.2.2.3 Conductor loss of CBCPW

There have not been any formulations for the loss of the conductor-backed CPW (CBCPW) in the literature. In order to account for the attenuation attributed to the conductor-backing, an analytical expression of the conductor loss in CBCPW is developed using the incremental-inductance method. All the metallizations are treated as normal conductors. This is given by

$$\alpha_c^{CBCPW} = \frac{8.68}{\mu_0 c_0 Z_0^{CPWG}}\left[R_f^s\left(\frac{\partial Z_0^a}{\partial s}-\frac{\partial Z_0^a}{\partial w}-\frac{\partial Z_0^a}{\partial t}+\frac{1}{2}\frac{\partial Z_0^a}{\partial h}\right)+R_f^g\left(\frac{1}{2}\frac{\partial Z_0^a}{\partial h}\right)\right] \quad \textbf{Equation 4-16a}$$

where Z_0^a is the characteristic impedance of CBCPW with air as dielectric, i.e. $\varepsilon_{eff} = 1$ in (4-4). R_f^s and R_f^g are the surface resistances on the coplanar strip and the conductor-backing. Assume $R_f^s=R_f^g$. The difficulty in this derivation is to find the dependence of Z_0^a on the conductor thickness t. Since infinitely thin conductors are assumed for the calculation of Z_0^a by (4-4), in order to take the conductor thickness into account, effective values of the strip and slot widths have to be defined. The resultant attenuation can be expressed in the following form,

$$\alpha_c^{CPWG} = \frac{8.68}{60\pi^2\mu_0 c_0} R_f \varepsilon_{eff} Z_0^{CPWG}\left(X_1\cdot Y_1 + X_2\cdot Y_2\right) \quad \textbf{Equation 4-16b}$$

X_1, Y_1, X_2, and Y_2, together with the detailed derivation are given in Section A.3.2.2 of Appendix A. The conductor losses of a CPW and a CBCPW with the same dimensions (Figure 4.2 and Table 4-2) are calculated using the incremental-inductance method. It is found that only 2% extra loss is introduced by the conductor-backing.

4.2.3 Cross coupling between parallel coplanar lines

Cross coupling occurs when the fields of different transmission media overlap with each other. If a signal is passing through such a system with cross coupling, some energy transfers between adjacent lines, which results in crosstalk preceding or lagging behind the intended signal. If the magnitude of the crosstalk is high enough, an incorrect switch or response may be incurred in signal processing. Here, a coupling coefficient is used to estimate this magnitude, which is defined as[4]

$$c = \frac{Z_e - Z_o}{Z_e + Z_o} \qquad \textbf{Equation 4-17}$$

c is the maximum of the backward coupling $|S_{41}|$ in a pair of coupled lines (Figure 4.7), which can be expressed as

$$|S_{41}| = \frac{c \cdot \sin(\phi)}{\sqrt{1 - c^2 \cdot \cos^2(\phi)}} \qquad \textbf{Equation 4-18}$$

where $\phi=\beta l$, and l is the length of the coupled line. The maximum coupling occurs when $\beta l=\pi/2$. The even- and odd-mode impedances (Z_e and Z_o) of the structure in Figure 4.7 can be evaluated by conformal-mapping method[22,23]. See Appendix B for details.

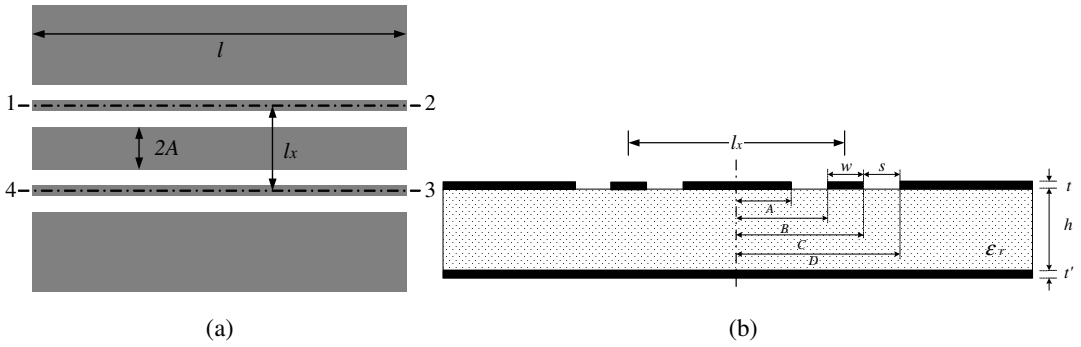

Figure 4.7 (a) A pair of parallel coupled coplanar lines. (b) Dimensional symbols for the parallel coupled CBCPW lines. The dimensions for the coupled CPW lines are the same but without the conductor backing. The centre-to-centre separation between the two lines is $l_x=B+C$.

Figure 4.8(a) contains the calculation results for a pair of parallel coupled coplanar lines with a strip width of 0.02mm. Also included are results from Sonnet[5] simulations using the layouts in Figure 4.9 for even-mode and odd-mode respectively. In layout (a), the ports are

numbered as +1/+1 and +2/+2 to set an even excitation. In layout (b), the ports are numbered as +1/-1 and +2/-2 to set an odd excitation. The calculated coupling coefficients using conformal-mapping method agree very well with those from Sonnet as shown in Figure 4.8(b). The consistency of analytical formulas with full-wave simulations in evaluating both the coupling and characteristic impedance gives full confidence in using conformal mapping. The displacement of the impedances obtained using the two methods in Figure 4.8(a) is because the simulated coplanar line has a characteristic impedance of 54Ω due to a 2:1 slot-to-strip ratio.

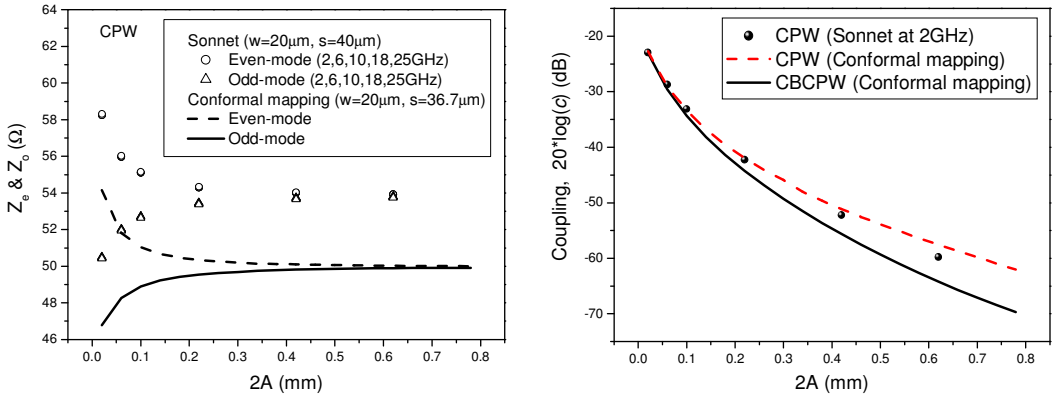

Figure 4.8 (a) Even- and odd-mode impedances of coupled CPW lines; (b) Coupling coefficients of parallel CPW lines and CBCPW lines. Both graphs are plotted against the in-plane ground width 2*A* between the two lines. The results from Sonnet simulations and conformal-mapping calculations are compared.

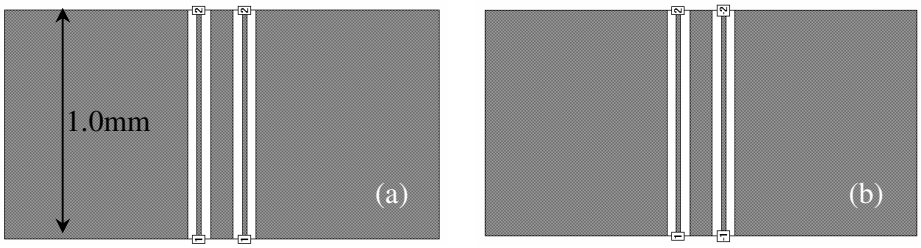

Figure 4.9 The layouts for evaluating the impedances of (a) even-mode and (b) odd-mode in Sonnet. The coplanar line width is 0.02mm and the slot width is 0.04mm.

For the coupled CPW lines, when the ground width (2*A*) between the two lines is 10 times the strip width, the coupling is -40dB, when it is 20 times wider, the coupling is reduced to less than -50dB. With the same dimensions, the CBCPW shows weaker cross-coupling than the CPW (Figure 4.8(b)). This indicates that the conductor-backing of the CBCPW also has some screening effect as the in-plane ground does. From conformal-mapping calculations, it

is found that a thicker substrate causes slightly stronger coupling in CBCPW, while for the CPW, the substrate thickness has little effect on the cross-coupling.

Using full-wave simulations, the mode impedances can be evaluated at different frequencies for the pair of coupled lines in Figure 4.9. The calculated Z_o and Z_e are given in Figure 4.8(a) at 2, 6, 10, 18, and 25 GHz. But their variation with frequency is very small. As shown in Table 4-5, the coupling only increases slightly at 25 GHz, compared with that at 2 GHz.

Table 4-5 Comparison of the coupling level at 2 GHz and 25 GHz between the coupled CPW lines (*w*=0.02mm, *s*=0.04mm). The coupling coefficients are acquired by Sonnet simulations using the structures shown in Figure 4.9.

2*A* (mm)	Coupling (dB) at 2GHz	Coupling (dB) at 25 GHz
0.10	-33.1	-32.6
0.22	-42.3	-40.9
0.42	-52.2	-49.1
0.62	-59.8	-55.0

In the experimental delay lines, the coplanar line is 0.04mm wide. The narrowest ground width (2*A*) is 0.2 mm, resulting in -33 dB coupling (see Table 4-6). Compared with other published HTS delay lines (decoupled by -40 to -55 dB, see Table 2-1), the delay lines in this work have to tolerate stronger cross coupling.

Table 4-6 Cross coupling between a pair of 0.04mm wide coplanar lines, calculated using conformal-mapping method.

***w* (mm) / *s* (mm)**	**2*A* (mm)**	**CPW**		**CBCPW**	
		Coupling (dB)	**Z_e (Ω) / Z_o (Ω)**	**Coupling (dB)**	**Z_e (Ω) / Z_o (Ω)**
0.040 / 0.074	0.04	-22.5	54.5 / 46.9	-23.7	53.4 / 46.9
	0.10	-27.4	52.4 / 48.2	-29.3	51.5 / 48.1
	0.20	-33.0*	51.3 / 49.0	-36.1	50.5 / 48.9
	0.40	-40.5	50.6 / 49.7	-46.1	50.0 / 49.5
	0.80	-51.3	50.3 / 50.0	-60.6	49.7 / 49.6

* According to Sonnet simulation, if 2*A*=0.20 mm, the backward coupling S_{41} is -33.8dB at the maximum.

4.2.4 Parasitic modes in CPW and CBCPW

Figure 4.10 shows the quasi-static field distributions of three ideal propagation modes: CPW, microstrip, and CBCPW. In practice, there always exist different parasitic modes, particularly in the two coplanar structures.

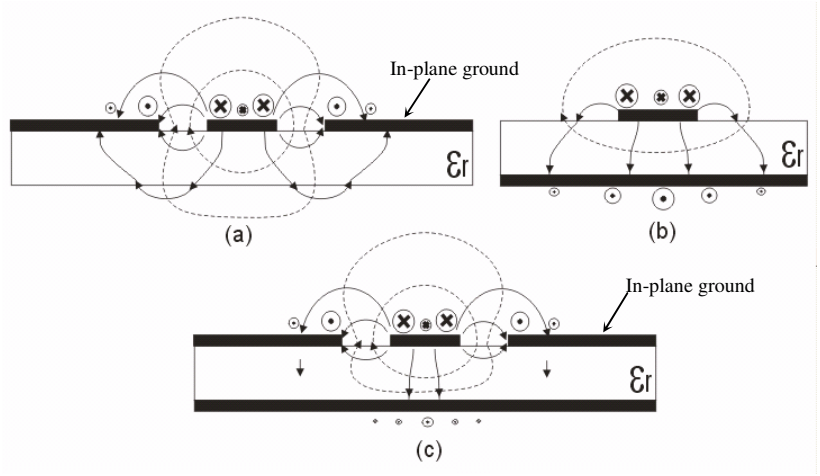

Figure 4.10 Quasi-static field distribution of (a) CPW, (b) micrsotrip and (c) CBCPW. The current density distributions are roughly marked as circles of different sizes, with "×" for the current flow into the paper and "•" out of the paper.

- Slotline mode

The most problematic parasitic mode in a coplanar waveguide is the slotline mode. It is induced by unequal potentials between the two in-plane grounds alongside of the signal line. These unbalanced in-plane grounds exist in many asymmetric structures, such as coplanar bends[24], where the unequal potentials can be regarded as the result of different path-lengths between the inner slot and outer slot, guiding the CPW mode.[25] This is illustrated in Figure 4.11(a).

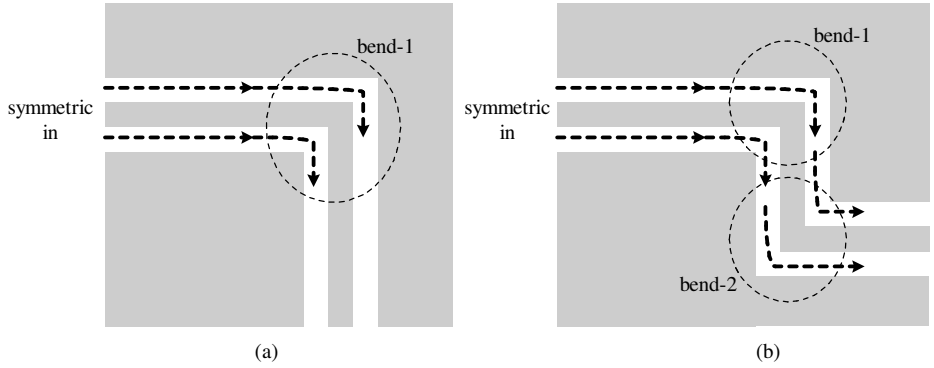

Figure 4.11 Illustration of the signal paths in the slots of a CPW line. The transient signals in the two slots are asynchronous after travelling through (a) a single bend, but may be synchronised again after passing through (b) the pair of oppositely oriented bends.

There are several possible ways to suppress this mode. Some are by means of imposing equal potentials on the unbalanced grounds. Some are by compensating the path difference. Others may try to attenuate the slotline mode while maintaining dominant CPW mode.

(1) Wire-bond or air-bridge

The conventional way is to use conductor crossovers (wire-bond or air-bridge [26]), interconnecting the unbalanced in-plane grounds (Figure 4.12 shows a picture of a bond-wire on a HTS CPW delay line). The disadvantage is the increase in loss and the occurrence of resonances between bonds or bridges. This method is also costly, especially for a complex CPW circuit where a large number of crossovers may be needed.

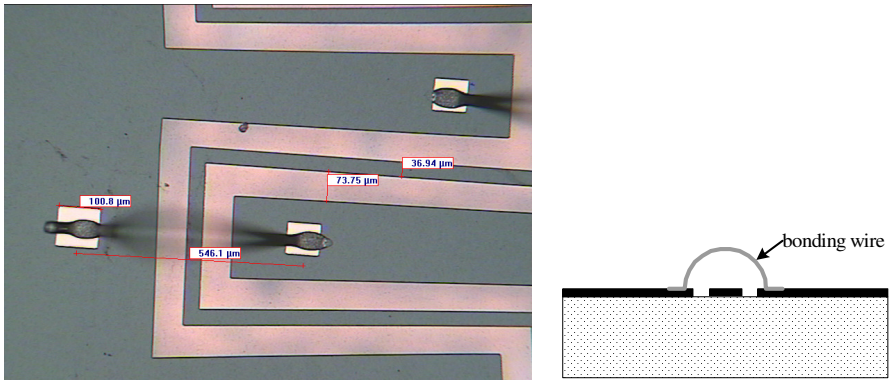

Figure 4.12 A bond-wire in a HTS CPW delay line. 25 µm wide aluminum wire bonded on gold pads; bonding force: 23g; height of the crossover: 60% of the length (for longer bonds it may be 30% of the length); bond wire DC resistance: about 55 Ω/m; bond-pull strength: 9-10g estimated.

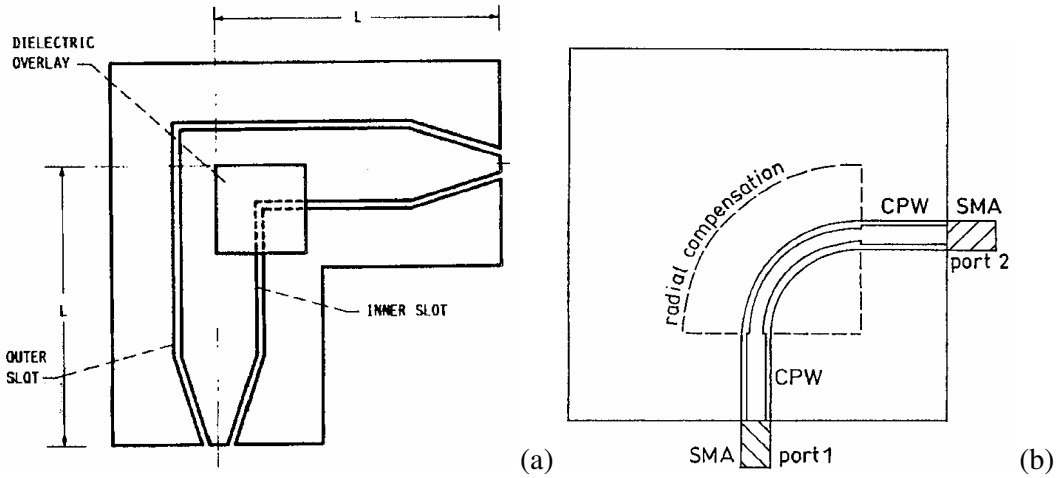

Figure 4.13 (a) Dielectric overlay. Taken from [25]. ©IEEE; (b) Quarter-disk patch as conductor-backing. Taken from [24]. ©IEE

(2) Dielectric overlay

To compensate the path difference, one way is to slow down the wave travelling in the inner slot, which is shorter in length, so that it emerges from the bend in phase with the wave in the outer slot. This can be done by placing a dielectric medium over the inner slot as shown in Figure 4.13(a)[25]. This has been shown to be effective over a broad band. But it is not

practical for a complex circuit with many coplanar bends. In addition, the dielectric overlay will unavoidably increase the loss.

(3) Quarter-disk patch as conductor-backing

Another way to compensate the path difference has been suggested by laying a quarter-disk patch beneath the bend structure as shown in Figure 4.13(b)[24]. This patch forms a localised conductor-backing and it can be realised by photolithography. The frequency and bandwidth of the effective compensation depend on the radius of the patch, which needs to be carefully optimised.

(4) Top and bottom shields

Interestingly, the top and bottom shields of a packaged device have been found to be able to reduce the slotline modes.[27] This effect was explained as an attenuation of slot mode. As pointed out in [27], the field of a slot mode decays slower than a CPW mode in the direction normal to the substrate surface, so that it would be more severely affected by the shields. The top shield can be the box lid and the bottom shield can be the conductor-backing of a CBCPW structure. However, to suppress the slot mode effectively, either shield should be placed as close as possible to the slots. It was suggested that the space between the circuit and the shields should be less than $w+2s$.[27] This brings unfavourable effect of power leakage into parallel-plate modes.[27] In addition, because microstrip mode may dominate when the bottom shield (conductor backing) is too close, it may be the propagating microstrip mode that helps to reduce the slot mode.

(5) Others

The induction of slot modes due to the path difference has been visualised in time domain by picosecond transient measurements[28,29]. Excited by a symmetric input transient, the signals travelling in the two slots can be probed after they pass through a bend structure as in Figure 4.11(a). A separation in the arrival time was observed, which implies the presence of an odd mode. However, these signals can be synchronised again if they further pass the other oppositely oriented bend as illustrated in Figure 4.11(b). The symmetric CPW mode (even mode) is re-established in this way, although some signal distortion and reflection due to the bend is not reversible.[28] Even so, it is still helpful to suppress the slot mode (odd mode) before some energy leaks into it. In a meander line, there also exist similar structures which can geometrically compensate the path difference, i.e. a pair of U-turns, each with two bends. It may be interesting to look at their possible compensating effect. The commercial software

simulator ADS[30] provides a useful technique, which enables simulation of the magnetic current in the slots rather than the electrical current in the conductors. This may be a helpful tool to investigate the phase difference between the signals travelling in the two slots.

Among all the available approaches to suppress slotline modes, the only practical one for a long delay line, operating over a wideband, would have to be wire-bonding. However, it is found in my work that a conductor-backed coplanar delay line is immune from the parasitic modes. Although it is not fully understood, the suppression effect of the conductor backing is so obvious and helpful, as will be discussed in Chapter 9. It is believed that none of the abovementioned mode-suppression effects works in a similar way as the conductor backing.

Besides the slotline mode, a coplanar waveguide may also hold odd TE and even TM surface wave modes. This is because the in-plane ground together with the dielectric underneath forms a conductor-backed "dielectric slab".[31]

- Parallel-plate mode and microstrip mode in CBCPW

For a CBCPW, if the in-plane ground is wide enough, parallel-plate mode may establish between the upper and lower ground plane. Proper interconnection between both ground planes can reduce this mode. If the in-plane ground is too narrow, that is also a problem. Riaziat[32] treated a CBCPW with narrow in-plane grounds as three coupled microstrip lines as in Figure 4.14. There are three normal propagation modes for such a configuration. Each mode is represented by a three-dimensional vector, with its elements representing the relative potentials on the three lines[33]. The following analysis quoted from [32] helps to understand the possible mode conversion from coplanar to microstrip.

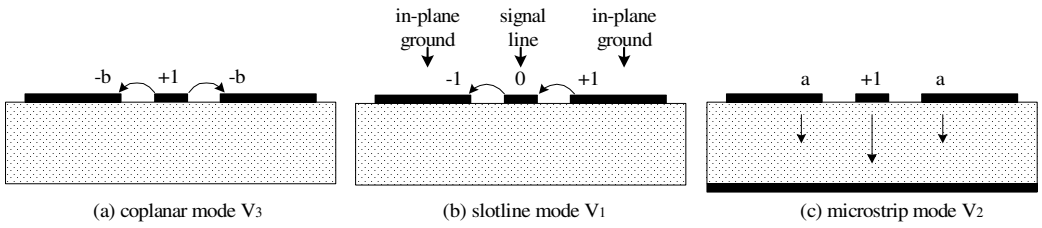

Figure 4.14 The three normal modes in a CBCPW structure with finite in-plane grounds.

An ideal excitation on a CBCPW line can be denoted by

$$V_0 = \begin{pmatrix} 0 & 1 & 0 \end{pmatrix}^T \qquad \textbf{Equation 4-19}$$

representing a signal on the centre conductor with the side conductors at zero potential. However, this is not a normal mode, which means "the relation between the three potentials on the lines will change as the excitation propagates" and finite potentials will appear on the ground planes. The 3 normal modes of V_0 are

$$V_1 = \begin{pmatrix} -1 & 0 & +1 \end{pmatrix}^T, \quad V_2 = \begin{pmatrix} a & 1 & a \end{pmatrix}^T, \quad V_3 = \begin{pmatrix} -b & 1 & -b \end{pmatrix}^T, (a \geq 0, b \geq 0),$$

as shown in Figure 4.14, the slotline mode, microstrip mode and coplanar mode. Even with the slotline mode V_1 fully suppressed, V_0 is still a combination of mode V_2 and V_3,

$$V_0 = \frac{1}{a+b}\left[b\begin{pmatrix} a \\ 1 \\ a \end{pmatrix} + a\begin{pmatrix} -b \\ 1 \\ -b \end{pmatrix} \right] = \frac{1}{a+b}\left[b \cdot V_2 + a \cdot V_3 \right]. \qquad \textbf{Equation 4-20}$$

So the coplanar mode V_3 is competing with a microstrip mode V_2. Although V_0 is not a normal mode, it can approximate to a single coplanar propagation mode if b is much less than 1. This is the case when the in-plane ground width and the substrate thickness are much larger than $w+2s$.[34] Otherwise, if $b>a$, a mode conversion from coplanar to microstrip may occur. Table 4-7 summarises the possible parasitic modes in the CPW and CBCPW.

Table 4-7 Summary of the possible parasitic modes in coplanar waveguides.

	Finite substrate		**Infinite substrate**
	Infinite in-plane ground	**Finite in-plane ground**	
CPW	odd TE_0 mode and even TM_0 mode of a dielectric slab	full slab modes	radiation from the guided CPW into the substrate
CBCPW	parallel plate waveguide modes	slotline mode, microstrip mode	--

[1] K. C. Gupta, R. Garg, I. Bahl, P. Bhartia, *Microstrip lines and slotlines*, 2nd ed., Artech House, 1996.
[2] R. K. Hoffmann, *Handbook of microwave integrated circuits*, Artech House, 1987.
[3] R. N. Simons, *Coplanar Waveguide Circuits Components and System*, Wiley-IEEE Press, Apr. 2001.
[4] R. E. Collin, *Foundations for microwave engineering*, 2nd ed., McGraw-Hill, 1992.
[5] Sonnet simulation tools, Sonnet Software, Inc.
[6] L. H. Lee, S. M. Ali, W. G. Lyons, D. E. Oats, J. D. Goettee, "Analysis of superconducting transmission-line structures for passive microwave device applications", *IEEE Trans. Appl. Supercond.*, vol. 3, no. 1, pp. 2782-2787, Mar. 1993.

[7] G. Ghione, C. Naldi, "Coplanar waveguides for MMIC applications: effect of upper shielding conductor backing, finite-extent ground planes, and line-to-line coupling", *IEEE Trans. Microwave Theo. Tech.*, vol. 35, no. 3, pp. 260-267, Mar. 1987.
[8] G. Hasnain, A. Dienes, J. R. Whinnery, "Dispersion of picosecond pulses in coplanar transmission lines", *IEEE Trans. Microwave Theo. Tech.*, vol. 34, no. 6, pp. 738-741, Jun. 1986.
[9] Agilent High Frequency Structure Simulator (HFSS) 5.5 simulation tools, Agilent Technologies.
[10] H. A. Wheeler, "Formulas for the skin effect", *Proceedings of the I.R.E.*, pp. 412-424, Sept. 1942.
[11] R. A. Pucel, D. J. Massé, C. P. Hartwig, "Losses in microstrip", *IEEE Trans. Microwave Theory Tech.*, vol. 16, no. 6, pp. 342-350, Jun. 1968.
[12] G. H. Owyang, T. T. Wu, "The approximate parameters of slot lines and their complement", *IRE Trans. Anten. Propag.*, pp. 49-55, Jan. 1958.
[13] G. Ghione, "A CAD-oriented analytical model for the losses of general asymmetric coplanar lines in hybrid and monolithic MICs", *IEEE Trans. Microwave Theory Tech.*, vol. 41, no. 9, pp. 1499-1510, Sep. 1993.
[14] D. Okai, M. Kusunoki, M. Mukaida, S. Ohshima, "Surface resistance measurement of superconducting thin film using probe-coupling-type microstrip line resonator", *Electronics and Communications in Japan*, part 2, vol. 86, no. 4, pp. 27-35, 2003. Translated from *Denshi Joho Tsushin Gakkai Ronbunshi*, vol. J84-C, no. 11, pp. 1113-1121, Nov. 2001.
[15] R. E. Collin, *Field theory of guided waves*, McGraw-Hill, pp. 124-128, 1960.
[16] W. Heinrich, "Model-matching approach for superconducting planar transmission lines including finite conductor thickness", *IEEE Microwave Guided Wave Lett.*, vol. 1, pp. 294-296, Oct. 1991.
[17] C. L. Holloway, E. F. Kuester, "Edge shape effects and quasi-closed form expressions for the conductor loss of microstrip lines", *Radio Science*, vol. 29, no. 3, pp. 539-559, May 1994.
[18] L. Lewis, "A method of avoiding the edge current divergence in perturbation loss calculations", *IEEE Trans. Microwave Theory Tech.*, vol. 32, no. 7, pp. 717-719, 1984.
[19] J. C. Booth, C. L. Holloway, "Conductor loss in superconducting planar structures: calculations and measurements," *IEEE Trans. Microwave Theory Tech.*, vol. 47, no. 6, pp. 769-774, Jun. 1999.
[20] A. Porch, M. J. Lancaster, R. G. Humphreys, "The coplanar resonator technique for determining the surface impedance of $YBa_2Cu_3O_{7-\delta}$ thin film", *IEEE Trans. Microw. Theo. Tech.*, vol. 43, no. 2, pp. 306-314, 1995.
[21] T. Konaka, M. Sato, H. Asano, S. Kubo, "Relative permittivity and dielectric loss tangent of substrate materials for high-T_c superconducting film," *J. Supercond.*, vol. 4, pp. 283-288, 1991.
[22] K. K. M. Cheng, "Effect of conductor backing on the line-to-line coupling between parallel coplanar lines", *IEEE Trans. Microwave Theo. Tech.*, vol. 45, no. 7, pp. 1132-1134, 1997.
[23] K. K. M. Cheng, "Analytical formula for calculating the coupling characteristics between parallel coplanar lines", *Electronics Letters*, vol. 32, no. 13, pp. 1208-1209, Jun. 1996.
[24] D. Jaisson, "Coplanar waveguide bend with radial compensation", *IEE Proc. Microwave Anten. Propag.*, vol. 143, no. 5, pp. 447-450, Oct. 1996.
[25] R. N. Simons, G. E. Ponchak, "Modeling of some coplanar waveguides discontinuities", *IEEE Trans. Microwave Theory Tech.*, vol. 36, no. 12, pp. 1796-1803, Dec. 1988.
[26] T. Becks, I. Wolff, "Full-wave analysis of various coplanar bends and T-junctions with respect to different types of air-bridges", in *1993 IEEE MTT-S Int. Microwave Symp.*, pp. 697-700, 1993.
[27] A. A. Omar, Y. L. Chow, "Coplanar waveguide with top and bottom shields in place of air-bridges", *IEEE Trans. Microwave Theory Tech.*, vol. 41, no. 9, pp. 1559-1563, Sep. 1993.
[28] S. Alexandrou, R. Sobolewski, T. Y. Hsiang, "Bend-induced even and odd modes in picosecond electrical transients propagated on a coplanar waveguide", *Appl. Phys. Lett.*, vol. 60, no. 15, pp. 1836-1838, Apr. 1992; S. Alexandrou, R. Sobolewski, T. Y. Hsiang, "Time-domain characterization of bend coplanar waveguides", *IEEE J. Quantum Electronics*, vol. 28, no. 10, pp. 2325-2332, Oct. 1992.
[29] J. Lee, H. Lee, W. Kim, J. Lee, J. Kim, "Suppression of coupled-slotline mode on CPW using air-bridges measured by picosecond photoconductive sampling", *IEEE Microwave Guided Wave Letters*, vol. 9, no. 7, pp. 265-267, Jul. 1999.
[30] Advanced Design System (ADS) simulation tools, Agilent Technologies.
[31] E. M. Godshalk, "Generation and observation of surface waves on dielectric slabs and coplanar structures", in *1993 IEEE MTT-S Int. Microwave Symp.*, pp. 923-926, 1993.
[32] M. Riaziat, R. Majidi-Ahy, I. J. Feng, "Propagation Modes and Dispersion Characteristics of Coplanar Waveguides," *IEEE Trans. Microwave Theory Tech.*, vol. 38, pp. 245-251, Mar. 1990.
[33] K. D. Marx, "Propagation modes, equivalent circuits, and characteristic terminations for multiconductor transmission lines with inhomogeneous dielectrics", *IEEE Trans. Microwave Theory Tech.*, vol. 21, pp. 450-457, 1973.
[34] M. Riaziat, I. J. Feng, R. Majidi-Ahy, B. A. Auld, "Single-mode operation of coplanar waveguides", *Electronics Letters*, vol. 23, no. 24, pp. 1281-1283, Nov. 1987.

Chapter 5 Design considerations of delay lines

This chapter covers the design considerations from selecting the basic routing structure to determining the final pattern of the delay lines. It focuses on how to achieve a wide bandwidth and control the dispersion. The effect of cross coupling between adjacent sections of the delay line is investigated. The design mainly relies on full-wave simulations. Admittance-matrix method is also used to model the meander line structures. First of all, an introduction is given to categorise the usage of different full-wave simulators in various design contexts of delay lines.

5.1 Introduction to modelling and simulation

Three commercial full-wave simulators - Sonnet[1], ADS[2], and HFSS[3] - are used in different design contexts of this work. Main features of the simulators are compared in Table 5-1.

Table 5-1 Comparison of the commercial full-wave simulators used in this work.

	Sonnet 9	**ADS 2002**	**HFSS 5**
EM solving method	Method of moments	Method of moments	finite-element
Meshing cell	rectangle, conformal*	rectangle or triangle, (automatic)	tetrahedron (3D) or triangle (2D)
Memory requirement	medium	Low	high
Capability	planar 3 D	2.5 D	3 D
Mesh layer	strip layer	strip or slot layers	strip layer
Design context in this work	all unwound meander lines, taper transitions	all spiral structures	interconnection between coplanar and coaxial

Sonnet has been proved to be very accurate in the design of passive components, such as filters. It is used in this work whenever it is capable, such as for all the unwound meander structures. However, if there are non-rectangular edges in the simulation layout, the number of subsections required to fill in the irregular area increases significantly because of the rectangular meshing cell of Sonnet.[*] For a complex circuit, the required memory may become unacceptable. Unlike Sonnet, ADS is more efficient due to the use of triangular meshing cells. The number of subsections can be greatly reduced without sacrificing the

[*] Only recently after the design work in this project was completed, Sonnet introduced a "conformal mesh" technique in Release 9 to treat the non-rectangular edges.

accuracy. For this reason, ADS is adopted in this design to deal with the complex layout of the delay lines to be shown in Section 5.5.

As far as a complex coplanar structure is concerned, triangular meshing is still not enough to reduce the huge amount memory required on meshing the large extent of in-plane grounds. To further lower the computation effort, another unique capability of ADS is utilised, i.e. the slot-layer (an inverse of the strip layer) simulation strategy.[2] This is useful for slot-based structures such as coplanar waveguides or slotlines. ADS employs the *equivalence principle* of electromagnetics. Instead of simulating the electric current on the ground plane, only the electric field in the slot is considered and modelled as an equivalent magnetic current.[2] By meshing the slots rather than the much wider extent of ground planes, a large amount of memory usage and computing time is saved. This was the only way to simulate the complex coplanar structure (0.5 m long), as discussed in Section 5.5.

However, this slot-layer simulation strategy is not good for a conductor-backed CPW (CBCPW). The simulation response of a CBCPW meander line is accompanied by a parasitic mode. This may be the parallel-plate mode, which could be induced because of the assumed "semi-infinite" in-plane grounds in a slot layer. A finite in-plane ground could only be specified in the strip layer, but this will incur too much memory to be affordable for the simulation of the coplanar structure. For this reason, ADS simulation results are not obtained for the CBCPW version of the circuits studied in this chapter.

HFSS is only used to model the interconnections between the coplanar line and coaxial connector, which requires full 3D modelling capability. Limited by the computer memory, only configurations in close proximity to the feed-lines are put into the simulator, as discussed in Chapter 6.

As long as the simulation is run with discrete frequency steps, the resolution of the resultant response is often a problem. For a lossless circuit, some resonances or transmission notches may have infinite quality factors, and occur over a frequency band which is too narrow to be visible because of the finite frequency step. The adaptive-frequency-sampling (AFS) technique in ADS (or ABS-adaptive band synthesis-in Sonnet) can overcome this problem over a narrow band, but it is not efficient and practical in simulating a complex structure over a wide frequency range.

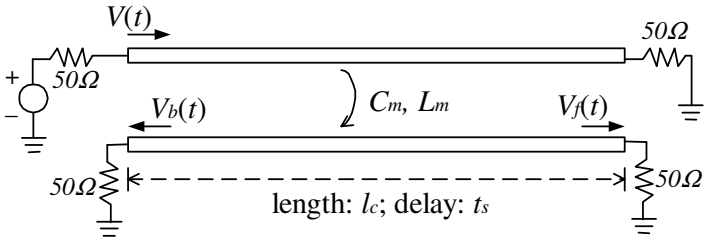

Figure 5.1 Crosstalk in parallel coupled transmission lines.

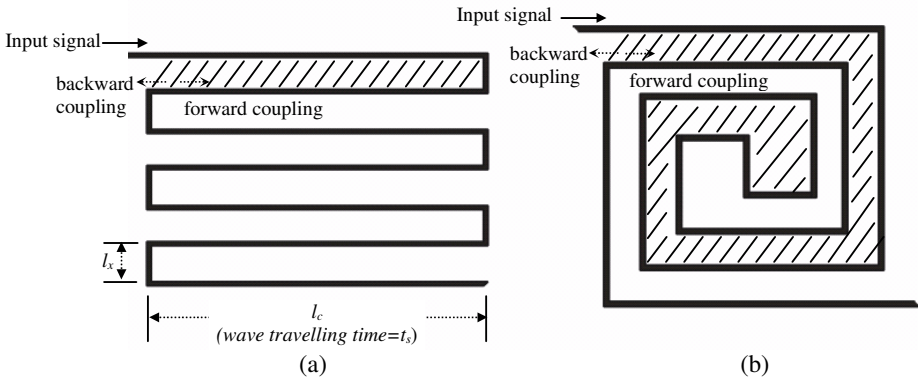

Figure 5.2 The backward and forward coupling in (a) a meander line and (b) a square double-spiral line. The shadow areas show where the coupled lines run parallel to each other, which may result in the accumulation of forward coupling with length.

5.2 Initial design concept

It is firstly important to find a novel routing structure with reduced impact of crosstalk. Crosstalk, usually described best in the time domain, is the spurious signal induced by cross coupling between transmission-line sections. In a pair of parallel coupled transmission lines as shown in Figure 5.1, the crosstalk signal $V_b(t)$ and $V_f(t)$ due to the backward coupling and forward coupling from an original signal $V(t)$ can be expressed by[4,5]

$$V_b(t) = K_b \cdot [V(t) - V(t - 2t_s)], \qquad where \quad K_b = \frac{1}{4}\left(\frac{C_m}{C} + \frac{L_m}{L}\right). \qquad \textbf{Equation 5-1}$$

$$V_f(t) = K_f \cdot t_s \cdot \frac{dV(t - t_s)}{dt}, \qquad where \quad K_f = \frac{1}{2}\left(\frac{C_m}{C} - \frac{L_m}{L}\right). \qquad \textbf{Equation 5-2}$$

where K_b and K_f are coupling coefficients, C_m, L_m, C, L are the mutual capacitance, mutual inductance, self capacitance and self inductance, t_s is the time delay along the coupled length l_c. Most analysis of crosstalk can be based on these simple relations. More intuitively and

accurately, the induction of crosstalk can be observed in the time domain response calculated by finite-difference-time-domain (FDTD) method.[6,7]

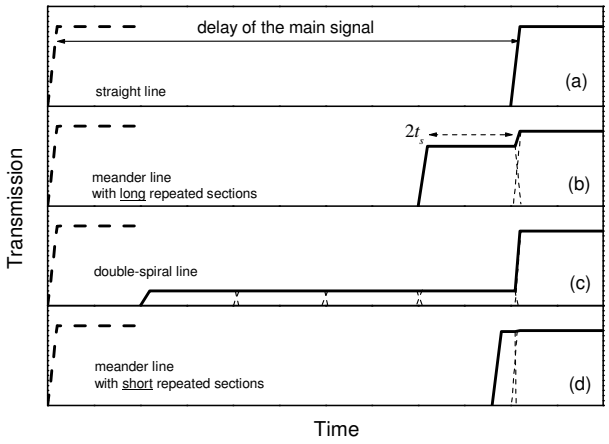

Figure 5.3 Received waveforms of a straight line, a meander line with long repeated sections, a double-spiral line, and a meander line with short sections, adapted from Fig. 3 of [8] and Fig. 5 of [9]. The input is a step-wave shown in dashed lines. Only crosstalk due to backward coupling between adjacent transmission lines is taken into account. t_s is the wave travelling time marked in Figure 5.2. A calculated impulse response by FDTD[7] and a step response by the method-of-moments[10] also support the analyses[8,9] leading to (b) and (c).

The commonly used delay line structures are meander and double-spiral as shown in Figure 5.2. The coupled length l_c of the meander line is only limited by the size of the usable substrate and usually much larger than the quarter-wavelength at the upper band limit. The impact of the crosstalk on the time domain response has been studied based on wave tracing model[8,9] by only considering the backward coupling between adjacent transmission lines. Adapted from Fig. 3 of [8] and Fig. 5 of [9], Figure 5.3 illustrates the simplified received waveforms from a straight line, a meander line with long repeated sections, a double-spiral line, and a meander line with short sections. The most severe crosstalk comes from the meander line with long repeated sections (long coupled lengths) as shown in Figure 5.3(b), where the crosstalk precedes the main signal by $2t_s$. As discussed in [8], this advance crosstalk is a consequence of cumulative backward coupling. Its magnitude depends on the coupling coefficient between adjacent lines and the number of repeated sections as well. If this crosstalk level is sufficiently high, it could cause a reduction of $2t_s$ in delay time. A meander line with unequal coupled lengths or a double-spiral line can reduce the effect of this accumulation. For a double-spiral line as in Figure 5.2(b), the crosstalk can be spread uniformly over a time span[9], as illustrated in Figure 5.3(c). In this sense, the double-spiral

line is a preferable structure because the crosstalk level is evenly lowered. This may avoid the penalty of delay time.

However, above analyses assume the crosstalk is solely from backward coupling. This is not valid for non-uniform transmission media such as coplanar waveguide and microstrip, where $C_m/C \neq L_m/L$ in (5-2) and forward coupling is non-zero. For a delay line with sufficiently long coupled length, the forward coupling may be even more detrimental than backward coupling because its magnitude is proportional to the travelling time as can be seen from (5-2), i.e. it is cumulative with length. This has been an argument for using stripline rather than other transmission media in delay lines[11], considering that a stripline ideally has no forward coupling. However, in practice the air gaps between the upper and lower substrates of a stripline still cause unequal odd- and even-mode velocities and so forward coupling also exists. It is believed that the cumulative forward coupling could be an inherent problem of a double-spiral structure, although this structure does have the advantage of reduced backward coupling. A double-spiral line can be regarded as a single-spiralled coupled-line pair with the two ends in the middle of the spiral connected, as shown by the shadow area in Figure 5.2(b). So the coupled length is about half of the total length. Disregarding the effect of multiple coupling for simplicity, the forward coupling may be accumulated to such a high level as to compromise the transmission efficiency. Full-wave simulations of a 0.5 m coplanar double-spiral line shown in Section 5.5 may give some evidence of this harmful forward coupling. It is not clear if the limited bandwidth of previously demonstrated double-spiral HTS delay lines can be accounted for by this forward coupling effect, even though they were made from stripline.

Besides the conventional meander line and double-spiral line shown in Figure 5.2, there is another choice, which is based on a meander structure but with sufficiently short coupled lengths l_c. This usually means l_c is shorter than the quarter-wavelength at the upper band limit. Clearly, in this case, t_s is reduced, so the preceding crosstalk would be close to and eventually merge with the main signal as illustrated in Figure 5.3(d). Although this adversely disperses the signal, it reduces the likely penalty of delay time. In addition, as long as the coupled length is shorter than a quarter-wavelength ($\lambda/4$=2.1 mm at 10 GHz for a 50Ω coplanar line on 0.508mm $LaAlO_3$), the magnitude of the cross coupling between adjacent meander segments is low. Following this concept, a delay line can be made out of a meander line with sufficiently short sections, which is then wound into certain pattern in order to fill

in a large area. As discussed in [12], when different parts of a meander line are in the proximity of each other, the forward coupling between them can be reduced as more electromagnetic field concentrates in between the short meander sections.

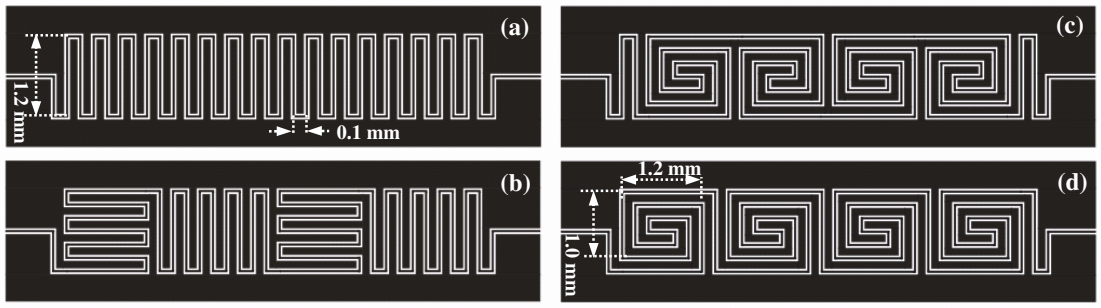

Figure 5.4 Layouts of (a) a meander line, (b) cascaded meanders with vertical orientations, (c) cascaded spirals-1, and (d) cascaded spirals-2. All the coplanar lines in the simulation layouts have *w*=0.020 mm and *s*=0.040 mm. Other dimensions are marked in the diagrams.

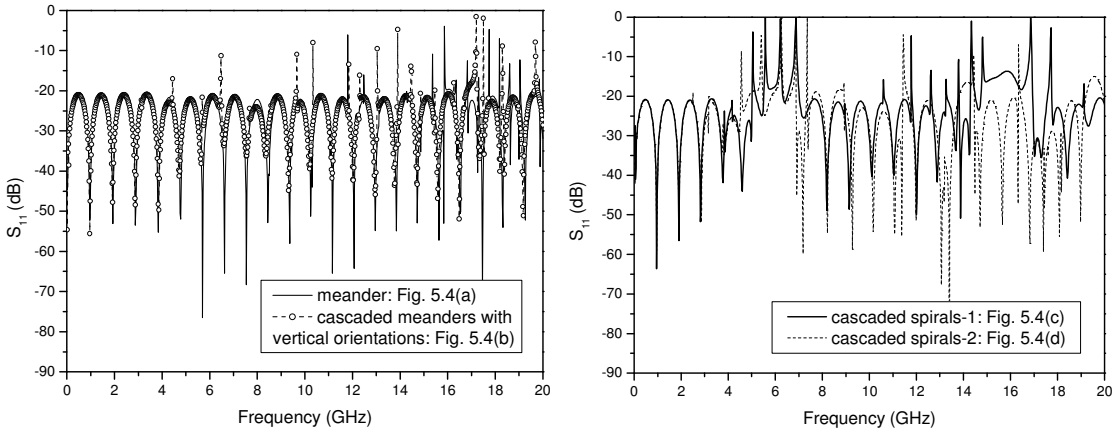

(a) (b)

Figure 5.5 Simulated S_{11} of the structures shown in Figure 5.4. The frequency step is 0.02GHz.

5.3 Comparison of basic routing structures

As shown in Figure 5.4, four basic structures with short coupled length less than 1.2 mm have been simulated. They are the meander line in Figure 5.4(a), the cascaded meanders with vertical orientations in Figure 5.4(b), and two types of cascaded double-spirals in Figure 5.4(c,d). The change of meandering orientations in Figure 5.4(b) may adversely function as a "bend" discontinuity, which results in more reflections above 10GHz as can be seen from S_{11} in Figure 5.5(a). The two cascaded double-spiral structures were intended to reduce the

effect of cumulative backward coupling. But both give poor responses at low frequencies in Figure 5.5(b).

Transmission lines with space-filling fractal structures are also investigated by simulations, as discussed in Appendix F. The achievable bandwidth of such routing structures is compromised by resonances due to the large number of variously oriented bends.

As a structure with the best wideband and resonance-free transmission, the meander line is adopted as the basic structure for the following design. What differs from other meander structures used for HTS delay lines (Table 2-1) is the short coupled length l_c. However, the disadvantage of a meander line is that the periodic structure makes it dispersive and band-limited, which is the topic of next section.

5.4 Dispersion and bandwidth of coplanar meander lines

A superconductor itself has no phase dispersion due to the frequency-independent penetration depth. A straight coplanar line also has negligible dispersion as discussed in Section 4.2.1. But when it is meandered, dispersion will be exhibited due to the periodicity and the presence of cross coupling. Weiss[13] formulated the dispersion of a periodic meander line analytically by

$$\tan^2\left(\frac{\phi}{4}\right) = \frac{Z_o}{Z_e}\begin{cases}\tan(k_e l_c/2)\tan(k_o l_c/2), \\ \cot(k_e l_c/2)\cot(k_o l_c/2),\end{cases} \qquad \textbf{Equation 5-3}$$

where l_c is the coupled length in a meander unit, ϕ is the phase increment per unit cell (with a length of $2l_c$). Subscripts o and e indicate the odd- and even-mode parameters of the parallel coupled sections in a meander line. The upper and lower equations are the forward- and backward-wave branches of the dispersion curves. This formula is based on the unit-cell approximation assuming an infinitely periodic meander line. A more accurate dispersion model for a finite structure can be established based on impedance or admittance matrices of multiple coupled lines[14].

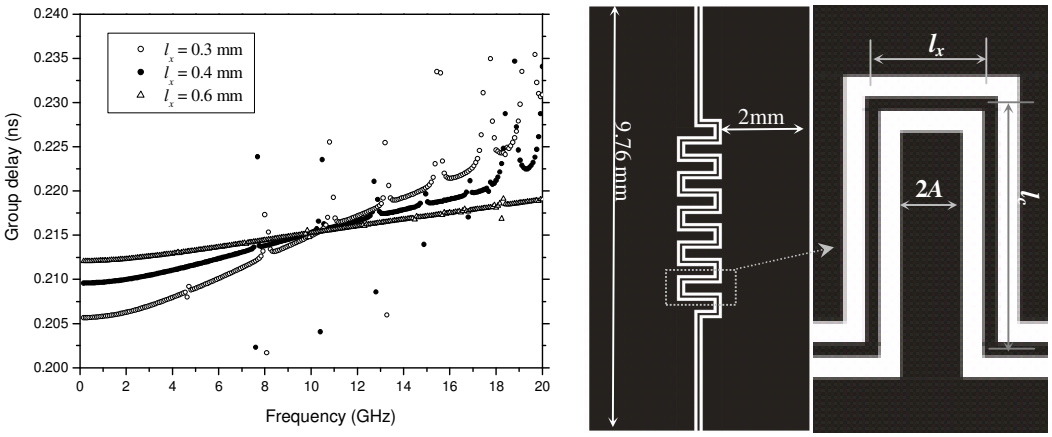

Figure 5.6 Group delays of three CPW meander lines with different separations between adjacent lines (l_x=0.3, 0.4, 0.6mm). The three lines have the same total length (19.04mm). Some dimensional symbols are marked in the enlarged meander unit. w=0.04mm, s=0.08mm, l_c=0.84mm.

From (5-3), it can be found that the larger difference in the wave numbers of even- and odd-mode, the larger is the deviation from linear phase. This means the dispersion increases with the coupling coefficients. The coupling is inversely related to the separation l_x between adjacent meander segments. By simulating three meander lines (Figure 5.6(b)) with 11 U-bends and l_x=0.3, 0.4, 0.6 mm using Sonnet, the difference of dispersions due to various coupling levels can be seen from the group delays as a function of frequency in Figure 5.6(a). The group delay is extracted from the phase change with respect to frequency as

$$t_g = \frac{l_{tot}}{\upsilon_g} = \frac{l_{tot}}{d\omega/d\beta} = \frac{l_{tot} \cdot d\beta}{d\omega} = -\frac{d\varphi}{d\omega} \qquad \textbf{Equation 5-4}$$

where φ is the phase change in a length of l_{tot}, the minus sign is due to the phase lag, i.e. $d\varphi < 0$. From 2 to 18 GHz, the group delay increases by 9% for l_x=0.3 mm, 5% for l_x=0.4 mm, and 3% for l_x=0.6 mm.

The dispersion equation (5-3) also implies that there is a stopband in the meander line at the frequency for which l_c is half of a wavelength. Cross coupling present between the meander segments may move the stopband to a lower frequency than expected. To investigate this, an unwound coplanar meander line with 91 U-bends (~1.2ns delay) is simulated using Sonnet up to 40 GHz. Figure 5.7(a) shows both the CPW and CBCPW meander lines have a stopband starting from 30 GHz and extending to 36 GHz. The stopband is an important feature of meander lines, which has been characterised on a PCB microstrip line[15] (with a

dielectric constant of 4.3). However, the same work did not observe a stopband in the stripline meander structure. The time domain reflection (TDR) measurements[15] showed that much less mismatch was experienced at the U-bends in the stripline meander line, as compared with the microstrip structure. This links the origin of the stopband to the discontinuity at the bends. This discontinuity is less of a problem in the stripline because of its lower mutual coupling. However, this can be enhanced in case of a larger dielectric constant or a more densely routed structure, where stronger coupling would be present in a meander line.

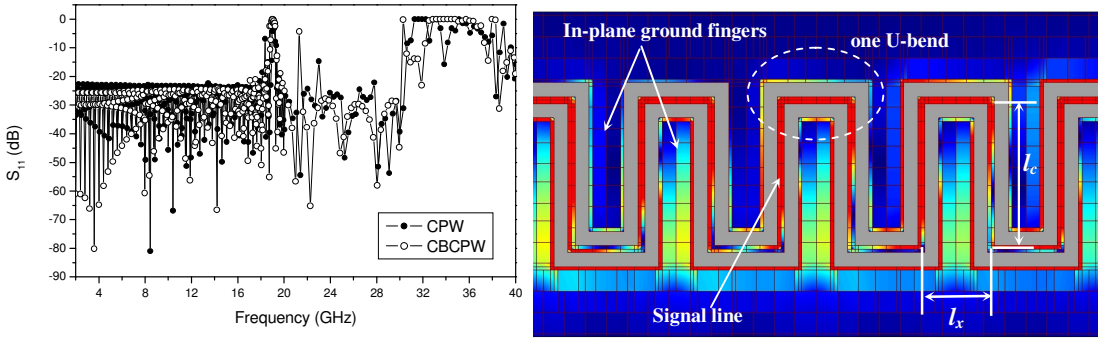

(a) (b)

Figure 5.7 (a) Simulated S_{11} for coplanar meander lines with 91 U-bends (b) Current density at 19.08 GHz (within the bandgap in S_{11}). In the simulation layout, w=0.040 mm, s=0.080 mm, l_c=0.84 mm, l_x=0.40 mm. Frequency step: 0.08GHz (0-20GHz) and 0.32GHz (20-40GHz).

In Figure 5.7(a), a bandgap at around 19 GHz can also be identified for both coplanar structures. The bandwidth of this bandgap is much smaller than that of the 30-36 GHz stopband. This is not predicted by either equation (5-3) or admittance-matrix method. To find the origin of this bandgap, the current-density distribution at 19.08 GHz is calculated for the CPW meander line. As shown in Figure 5.7(b), the color range from red to dark-blue corresponds to the current density from high to low. The highly uneven current distribution along the finger-like in-plane ground indicates a quarter-wavelength resonance with one end (dark blue) open and the other (light yellow) short to the ground patch. This produces the peak at 19 GHz in Figure 5.7(a). Similar bandgap structure has not been observed in microstrip meander lines[16]. It is unique to the coplanar meander structure due to the presence of in-plane grounds. The bandgap shifts to lower frequency as the coupled length l_c increases. This dependence has been investigated by Sonnet simulation. To save computation time, the meander line used in this simulation is shorter than the one in Figure 5.7 and has 41 U-bends. The distance l_x between the meander segments keeps unchanged at 0.4 mm, while

the coupled length l_c varies from 0.44 to 1.24 mm. Hence, the meander unit length ($l=l_x+l_c$) is between 0.84 and 1.64 mm. Figure 5.8(a) shows the simulated bandgaps for the meander lines with different unit lengths. The bandgaps all have a four-peak structure. The four peaks in the case of l=0.84 mm are marked in Figure 5.8(a) as A, B, C, and D. The frequencies at these peaks as a function of the meander unit length l are plotted in Figure 5.8(b). For a coplanar meander line to operate between 2 and 18 GHz, the unit length l of the meander should be less than 1.3 mm. From the S_{11} responses, it can be seen that the two resonances (B and C) couple with each other. For the meander line with a unit length l of 1.24 mm, the current-density distributions are shown in Figure 5.9 at the four resonant peaks of the bandgap and at 17.26 GHz where there is no resonance. At 17.26 GHz, the current density on the in-plane grounds is very low and uniformly distributed except at the edges of the conductors. In contrast, at the other four frequencies where resonances occur, the current distributions on the grounds are uneven, similar to the case in Figure 5.7. What distinguishes the four resonances is the different arrangement of the current distributions on the in-plane ground fingers. It should be noted that the meander line in Figure 5.7 shows somewhat different bandgap features from the four-peak structure. It is found that this fine feature depends on the number of meander units used in the simulation layout.

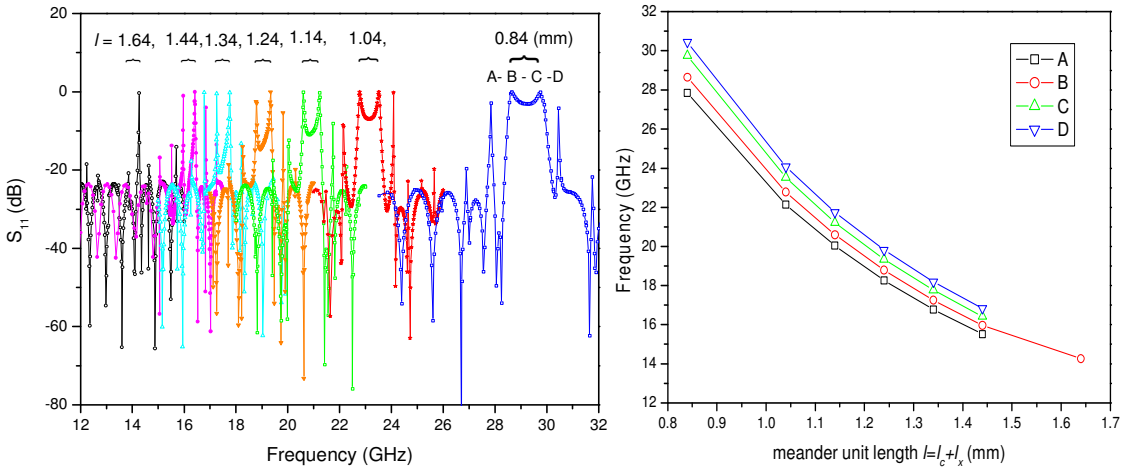

Figure 5.8 The change of the bandgap frequency with the meander unit length l in a CPW meander line. (w=0.040 mm, s=0.080 mm, l_x=0.4 mm)

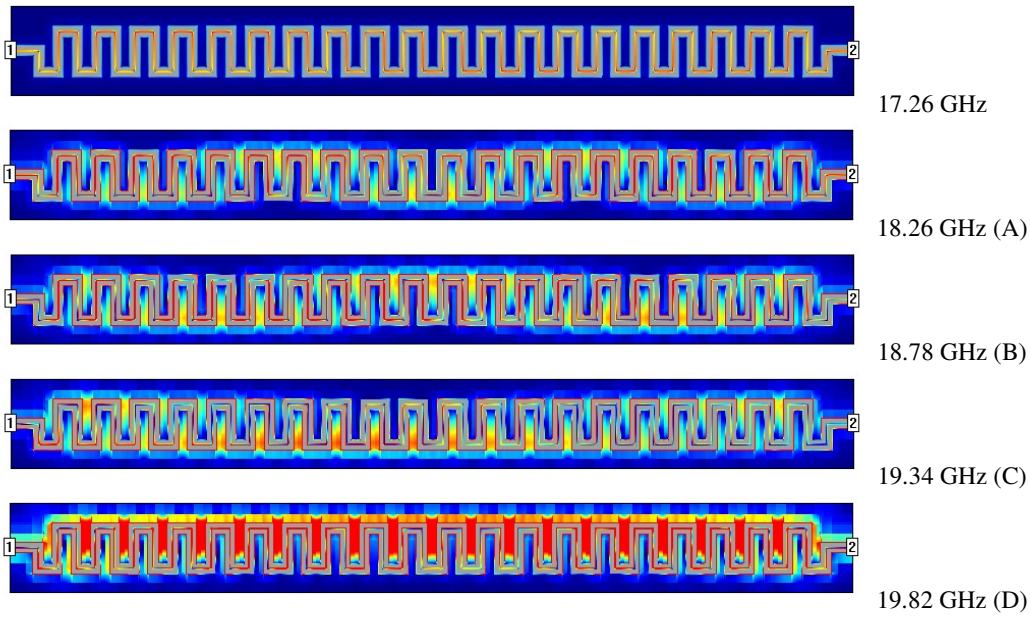

Figure 5.9 The current-density distributions of the meander line (*l*=1.24 mm). There is no resonance at 17.26 GHz, while the other four frequencies correspond to the four peaks around the bandgap.

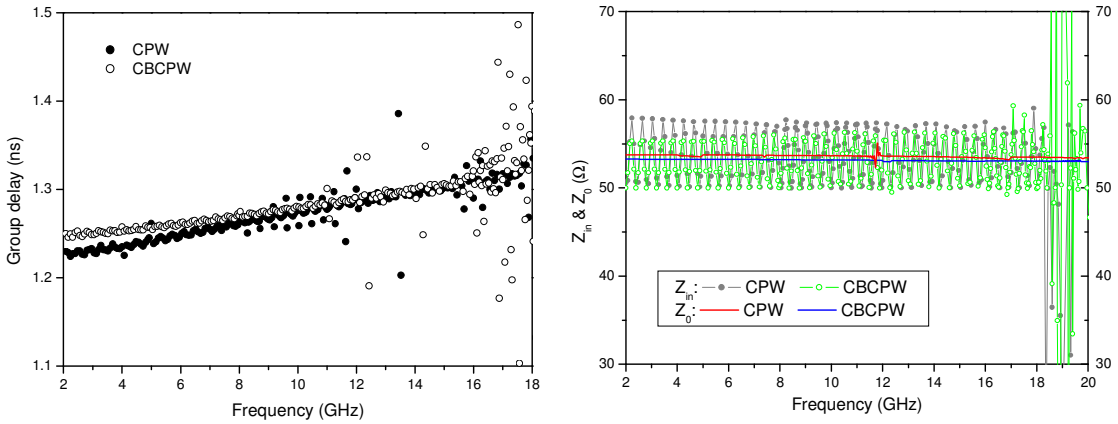

Figure 5.10 (a) Group delays, (b) input impedances of the CPW and CBCPW meander lines (~1.2 ns delay) in Figure 5.7.

From the simulated phase responses of Figure 5.7, the group delays of the CPW and CBCPW meander lines are evaluated and plotted in Figure 5.10(a). The CPW meander line is slightly more dispersive than the CBCPW line due to the relatively stronger cross coupling between adjacent CPW lines. The variations of the group delays from 2 to 18 GHz are 8.1% for the CPW and 6.4% for the CBCPW. This is larger than the 5% increase exhibited by the shorter CPW meander line (~0.21 ns) in Figure 5.6. The group delay of the CPW line is slightly smaller than the CBCPW at 2 GHz. This indicates a higher effective permittivity of the CBCPW due to the presence of conductor backing. But this difference reduces as the

frequency increases. Eventually, the group delays of the two meander lines converge at above 14 GHz. This shows that the conductor backing has more influence on the field distribution at lower frequency. Ripples and anomalies in the group delay are correlated with magnitude ripples and transmission notches in simulated S_{21} respectively, which are not shown. The ripples are mainly due to mismatch at the input/output. The notches are elusive, and change with the size of the simulation model. They are likely to be spurious resonances from the ground patches or slotline modes, although current distributions do not show clear patterns of ununiformity. It should be mentioned that such anomalies are not observed in the experimental CBCPW double-spiral meander delay line, to be presented in Chapter 9.

As a transmission line is meandered, its impedance is no longer like a straight line due to coupling and bend discontinuity. Figure 5.10(b) shows the simulated input impedance Z_{in} of the meander line and the characteristic impedance Z_0 of a short straight line. Although the ripples are big due to mismatch with the 50Ω port, Z_{in} generally fluctuates around Z_0 without deviating from it. This implies the coupling effect is not very strong. Otherwise, the resultant even- or odd-mode impedances will deflect from Z_0, as shown in Fig. 4.8(a). The port mismatch results from an expedient choice of a coplanar slot-to-strip ratio of 2, in order to simplify the meshing of the full-wave simulation. For the real devices, this ratio will be 1.85, providing a much better match with 50 Ω. Further optimised match between the input line and the meander is possible. This would be particularly useful if stronger coupling exists between segments of the meander lines.

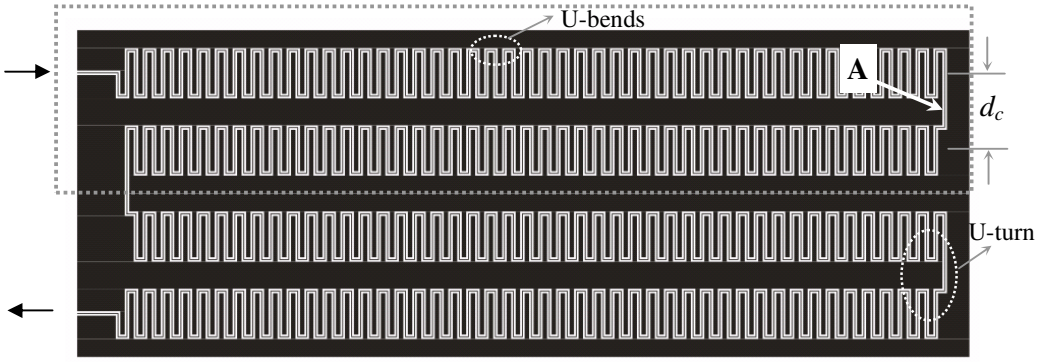

Figure 5.11 A meander line of short coupled length wound into a meandering structure. w=0.02 mm, l_x=0.2 mm, l_c=1.2 mm, d_c=1.9 mm. The two branches in the dash line box are used for Sonnet simulation.

To fill in a large substrate area with the meander lines of short coupled length, again there are two choices: meandering or spiralling. The disadvantage of a meandering structure as

shown in Figure 5.11 is the reflection from the U-turns joining adjacent meander branches. A structure with two juxtaposed meander branches (in the dash line box of Figure 5.11) is simulated. It produces 2.5ns total delay. The centre-to-centre distance (d_c) between the two branches is 1.9 mm.

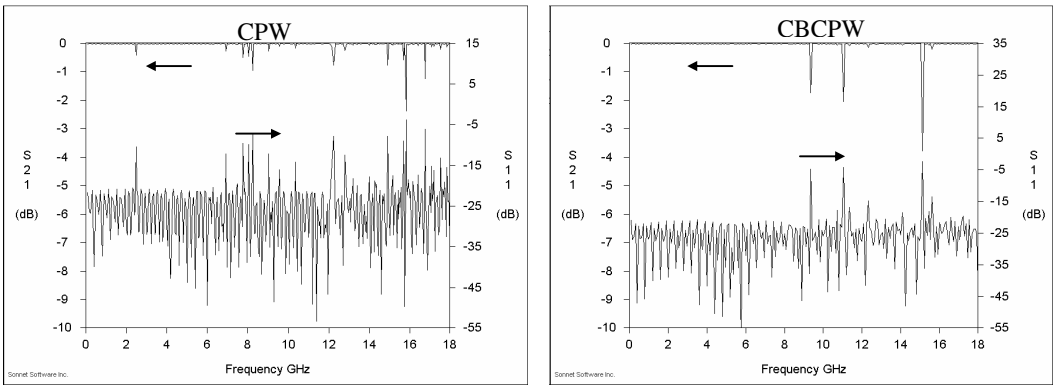

Figure 5.12 Simulated S-parameters of the CPW and CBCPW meander lines shown in the dash line box of Figure 5.11. The frequency step is 0.04 GHz.

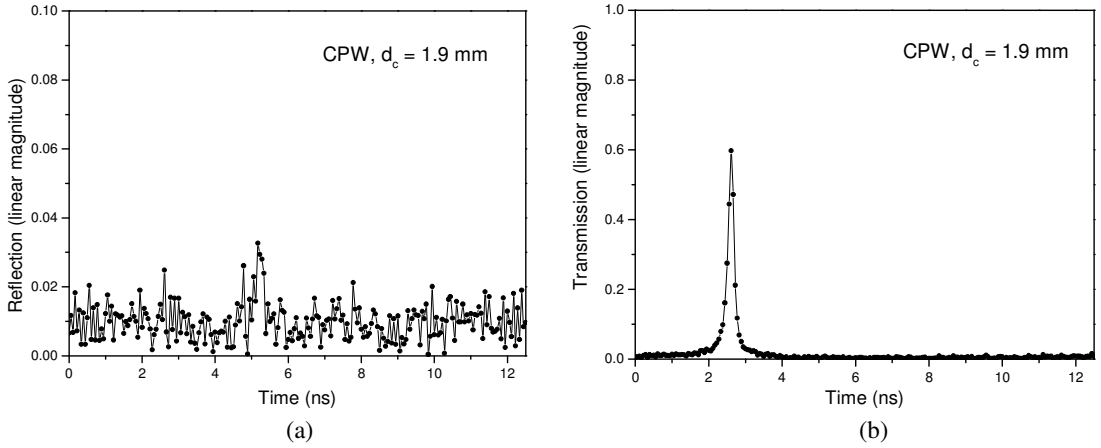

Figure 5.13 Time domain responses of the CPW meander line shown in the dash line box of Figure 5.11. The time interval of the responses is 0.056 ns, which is the reciprocal of a frequency range of 18 GHz.

The calculated S-parameters are shown in Figure 5.12. Using the same frequency step (0.04 GHz) in simulation, the CBCPW line sees fewer transmission notches. This may be in part attributed to the slightly lower cross coupling between adjacent CBCPW lines as shown in Figure 4.8. S_{11} and S_{21} of the CPW meander line are transformed to the time domain by Fast Fourier Transform (FFT) as shown in Figure 5.13. The peak in the transmission response of Figure 5.13(b) indicates a time delay of 2.5 ns. In the reflection response of Figure 5.13(a), the signal at 5 ns is reflected due to the port discontinuity, while the hump at 2.5 ns corresponds to the reflection from the U-turn at point-*A* in Figure 5.11. The effect of this

reflection may become more detrimental if a number of meander line branches are joined together as in Figure 5.11. A double-spiral structure without sharp turning structures can reduce the reflection in this aspect. Therefore, a double-spiral meander line (DSML) structure would be a better choice for the plane-filling pattern, as illustrated in Figure 5.14. It is a coplanar meander line with very short coupled lengths, which is then curled into a double-spiral, making a good use of the round substrate area. This will be the structure implemented in the experimental HTS delay lines, which is firstly investigated by simulations in the next section.

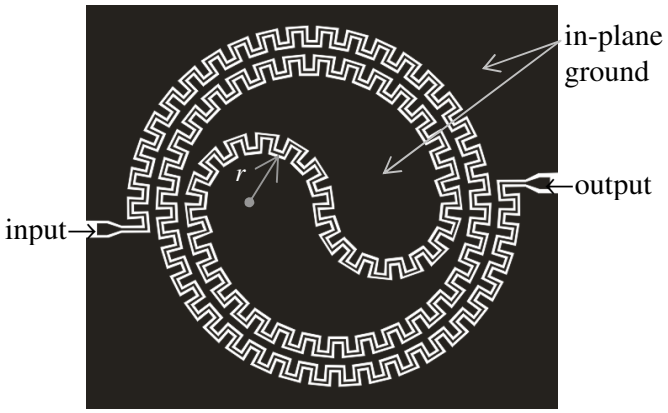

Figure 5.14 Diagrammatic view of a coplanar double-spiral meander line (DSML) structure with the black area showing the HTS thin film (not to the scale).

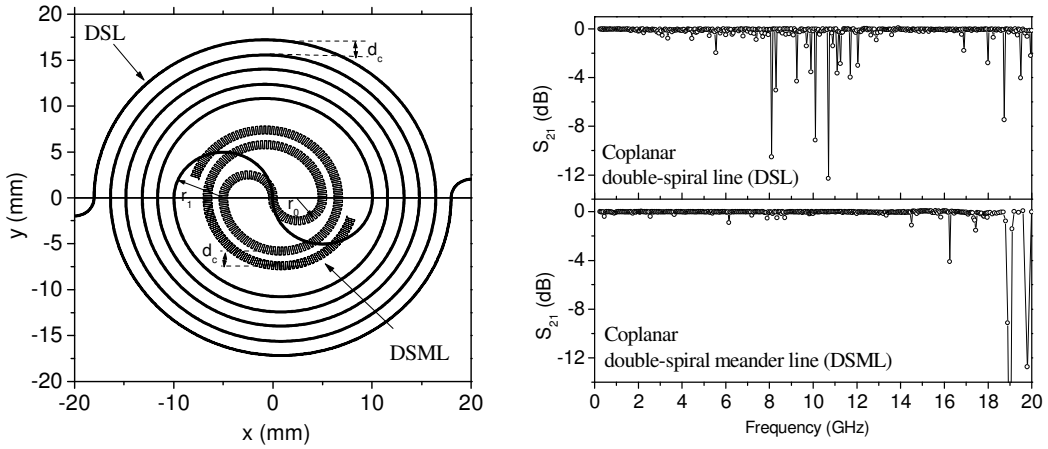

Figure 5.15 A comparison of a CPW-DSL and a CPW-DSML: (a) Layouts (For clarity, only the slots of the coplanar waveguides are plotted to show the routing structure, with the centre conductor between them too small to be visible.) (b) Simulated S_{21}. The frequency step is 0.050 GHz. In the simulation layout, w=0.02 mm, s=0.04 mm, l_x=0.2 mm, l_c=0.98 mm, r_0=2.5 mm, r_1=5 mm, d_c=1.6 mm.

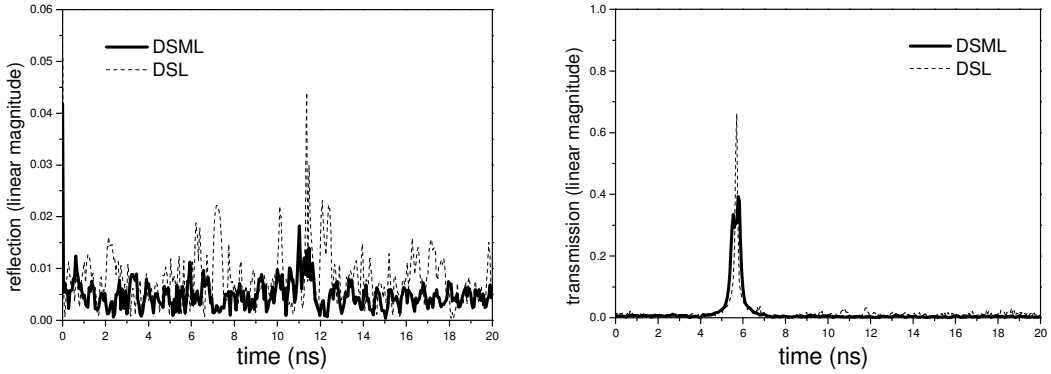

Figure 5.16 Time domain responses of the DSL and DSML in Figure 5.15: (a) reflection, (b) transmission. The time interval of the responses is 0.056 ns.

5.5 Double-spiral line and double-spiral meander line

Figure 5.15(a) shows a 0.5 m (~5.4 ns time delay) coplanar DSML, simulated using ADS in the slot layer, and compared with a conventional coplanar double-spiral line (DSL) of the same total length. Identical coplanar waveguide dimensions are used. The separation between the adjacent lines of the DSL is 1.6 mm (providing a coupling of less than –50 dB). This is the same as the space d_c between the meandered spiraling-turns in the DSML. The DSML structure is more compact mainly because a tighter coupling of -33 dB between each adjacent meander segments is tolerated, which is determined by l_x in Figure 5.6(b). In addition, a smaller inner radius is used in the simulation layout of DSML (r_0=2.5mm for the DSML, and r_1=5mm for the DSL). Even with these unfavorable factors, the DSML gives much better transmission properties over a wide frequency band than the DSL, as seen from the simulation results in Figure 5.15(b). It is believed that the coupling between adjacent meandered spiraling-turns is lowered as more electromagnetic field concentrates between the short meander segments rather than between the spiraling turns. The time domain response in Figure 5.16(a) shows that the DSL structure produces more reflected signals than the DSML. In a double-spiral structure, the reflection response contains the signals either reflected by discontinuities or sent back due to forward coupling. In terms of discontinuities, the DSL structure should be advantageous because it has a much wider inner radius and has not the large number of bends as in the meander structure. Therefore, the even more severe reflection in DSL is very likely due to the forward coupling in the double-spiral structure, which may be cumulative with length as discussed in Section 5.2.

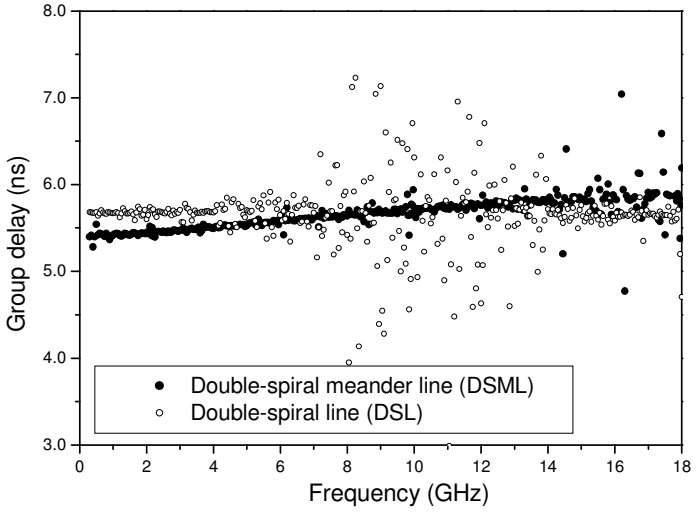

Figure 5.17 Group delays of the DSL and DSML estimated from the simulated phase responses.

A problem caused by the tighter coupling in the DSML structure is the increased dispersion. As shown in Figure 5.16(b), the transmitted pulse in the DSML is broadened, as compared with the DSL. In the frequency domain, this means a larger variation of group delay with frequency, which can be seen in Figure 5.17. The points of scattering in Figure 5.17 again correlate with the transmission notches in Figure 5.15(b). From 2 to 18 GHz, the group delay of the DSML increases by 8.5%.

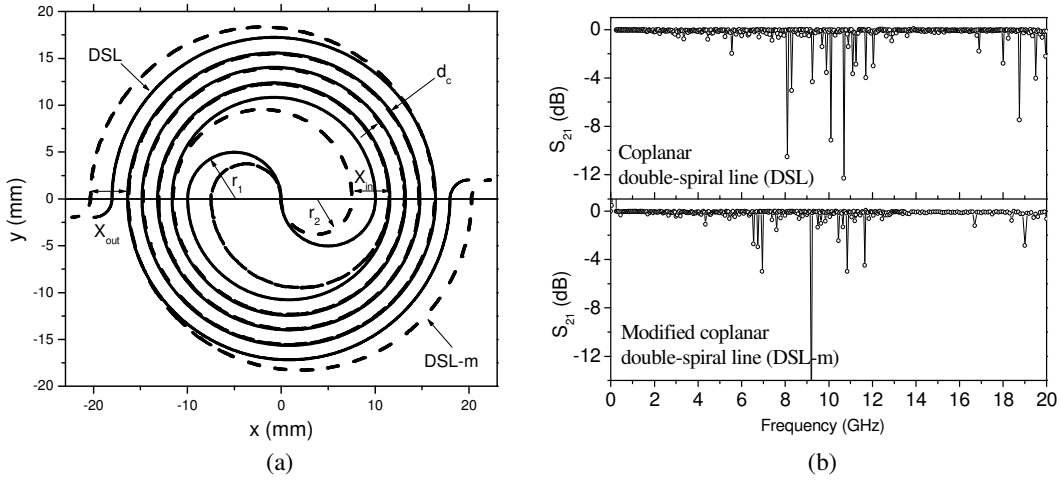

Figure 5.18 A comparison of the DSL and DSL-m: (a) Layout (For clarity, only the slots of the coplanar waveguides are plotted to show the routing structure, with the centre conductor between them too small to be visible.) (b) Simulated S_{21}. The frequency step is 0.050 GHz. w=0.02 mm, s=0.04 mm, d_c=1.6 mm, r_1=5 mm, r_2=3.75 mm, X_{in}=X_{out}=4 mm.

Poor S_{21} response has also been found in a microstrip DSL structure using similar ADS

simulations[16]. Minor modification has been tried on the CPW DSL to relax the coupling at the input/output and the inner part of the spiral as shown in Figure 5.18(a). From the simulation results of Figure 5.18(b), however, there is no significant improvement by this modification.

5.6 Summary (Chapter 4 and 5)

The delay line is designed to be 50Ω, avoiding the impedance transformation which could compromise the bandwidth. Simulations show that meandering does not alter the impedance very much. The input impedance of the meander line is hardly dependent of frequency until it is close to the bandgap at 19 GHz. Meandering would have more effect on the line impedance, if the mutual coupling becomes stronger as the space between the meander segments is reduced. The selection of the coplanar line width mainly depends on the specified loss level and also takes the size of the circuit into account. A 0.04 mm coplanar line with a slot width of 0.074 mm is used in this work. Based on a surface resistance of 110 μΩ (77K, 7.95GHz)[17], the analytically calculated attenuation is 0.134dB/ns at 18GHz, i.e. 6.7dB for a 50ns delay line. It is worth mentioning that some simulations (Figure 5.5, Figure 5.12, Figure 5.15, and Figure 5.18) were run on 0.02 mm wide transmission line as was specified at the initial design stage. The main findings from these simulations are still meaningful when the line width is relaxed to 0.04 mm and the same coupling level is maintained by scaling the separation between the coupled sections. All simulations to be compared with experiments in terms of dispersion and band limitations are run on 0.04 mm line, as in Figure 5.6, Figure 5.7, Figure 5.8, and Figure 5.10.

A meander line with a short coupled length (l_c=0.84 mm) is used as the basic structure in order to reduce the impact of crosstalk and achieve a bandwidth from 2 to 18 GHz. Unlike a microstrip meander line, with the first bandstop at the frequency for which the meander unit length l is half a wavelength, the coplanar meander line exhibits a bandgap due to a quarter-wavelength resonance on the in-plane ground. As a coplanar meander line is band-limited, its dimension must be optimised so that the first bandgap occurs beyond the band of interest (2-18 GHz). This requires the unit length l is less than 1.3 mm, which not only depends on the coupled length l_c, but also on the space l_x between adjacent meander segments. l_x also determines the level of cross coupling.

The selection of l_x correlates to the dispersion of the delay line. For the experimental delay lines, l_x is 0.39mm ($2A$=0.2mm), resulting in a coupling of -33 dB. According to the simulations in Figure 5.10, the dispersion in terms of the variation of group delay from 2 to 18 GHz is 8.1% for CPW and 6.4% for CBCPW. Linearly scaled to a 25 ns delay, the variation would be 2.0 ns and 1.6 ns respectively.

When the meander line is curled into a double-spiralling structure, there are other two parameters to be defined: the space d_c between the spiralling turns and the radius r of the innermost semi-circles. Having d_c in the DSML the same as the inter-line separation of a DSL, simulations show the DSML has much better transmission properties. In the experimental delay line, d_c is 1.6 mm. For a pair of straight coplanar lines separated by this distance, the coupling is lower than -50 dB. No optimisation is made on this parameter. A too small inner radius could increase the reflection from the middle of the spiral. In the simulation layout, the inner radius is 2.5 mm. For the experimental delay line, the radius is chosen to be as large as possible, so long as a 25 ns delay line can be fit in a 2-inch substrate area.

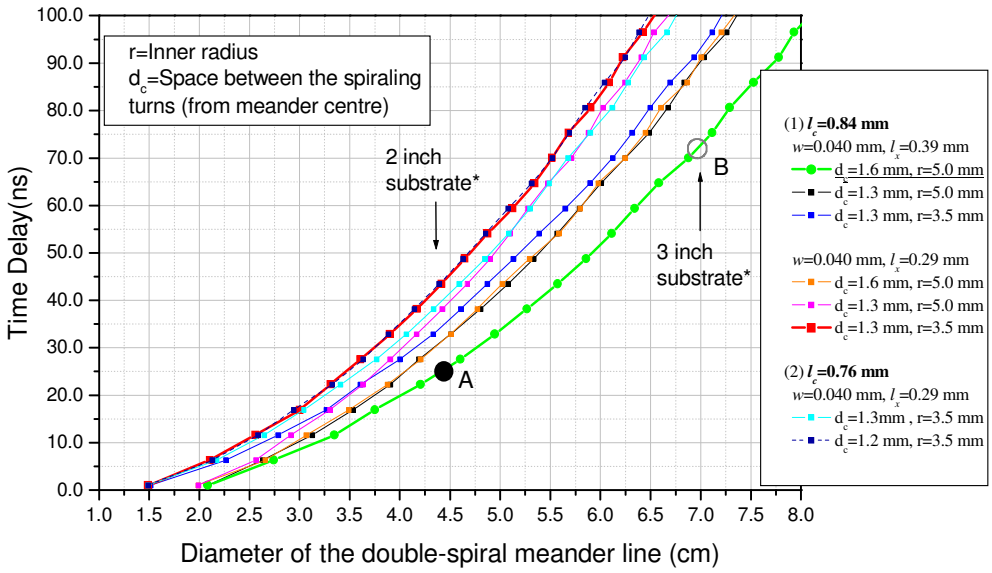

Figure 5.19 Achievable delay for a DSML structure using different geometric parameters.
*** with a 2.5 mm clearance between the circuit and the edge of the wafer.**

To summarize, the geometric parameters to be used are

- Coplanar line width and slot width: w=0.040 mm and s=0.074 mm;

- Width of the finger-like in-plane ground: $2A$=0.20 mm, so l_x=0.39 mm;
- Coupled length: l_c=0.84 mm, so l=l_x+l_c=1.23 mm;
- Distance between the meandered spiralling-turns: d_c=1.6 mm;
- Radius of the innermost semi-circle: r=5.0 mm.

This corresponds to the point A in Figure 5.19, which estimates the achievable delays for a DSML delay line using different geometric parameters. What can be seen from this graph is

(1) The coupled length l_c can be reduced from 0.84 mm to 0.76 mm without sacrificing the use of substrate. This will increase the frequency of the first bandgap to 21 GHz and achieve a wider bandwidth.

(2) Reducing the space d_c between the spiralling turns may prominently increase the achievable delay. But this needs to be carefully optimised so that it will not adversely increase the cross coupling and compromise the performance.

(3) To achieve 50 ns delay on a 2-inch wafer with the DSML structure, the geometric dimensions will be put to a limit, which is unfavourable to the performance. However, on a 3-inch wafer, 70 ns delay line can be realised (point B in Figure 5.19) with 2.5 mm clearance between the circuit and the edge of the wafer using the same dimensions as the 25 ns delay line tested in this project.

5.7 Admittance-matrix method and meander line

This section briefly presents some theoretical results by using admittance-matrix (Y-matrix) method on meander lines. It helps to understand the coupling structure. Details of the theory are given in Appendix C.

A meander line can be modelled using the admittance-matrix method by breaking the transmission line into a nodal structure as shown in Figure 5.20(a). This method has been widely used in modelling multiple coupled lines[18,19]. Although the accuracy is not as high as full-wave simulations, it is helpful to distinguish the outcomes of different effects such as electromagnetic coupling or impedance discontinuity in a meander line. This can be done by independently applying different mathematical representations of these effects. The coupling

between adjacent or even non-adjacent parallel sections in the meander line can be treated[20]. However, it is difficult to have the effect of the finite coplanar-grounds included in an admittance matrix. So, this method is more suitable for a microstrip circuit or a general transmission line. To construct the admittance matrix, odd- and even-mode parameters for the coupled lines (adjacent or non-adjacent) are required. These can be obtained by conformal mapping.

As an example, the meander line in Figure 5.20(a) is modelled as a 2-port/10-node structure, disregarding the bend corners. The evaluation procedure is described in Appendix C. As shown in Figure 5.20(b), the calculated S parameters agree well with the Sonnet simulations of a similar CPW meander line. The small inconsistency is partly due to the lack of representation of the coplanar in-plane grounds, which may cause parasitic propagation modes.

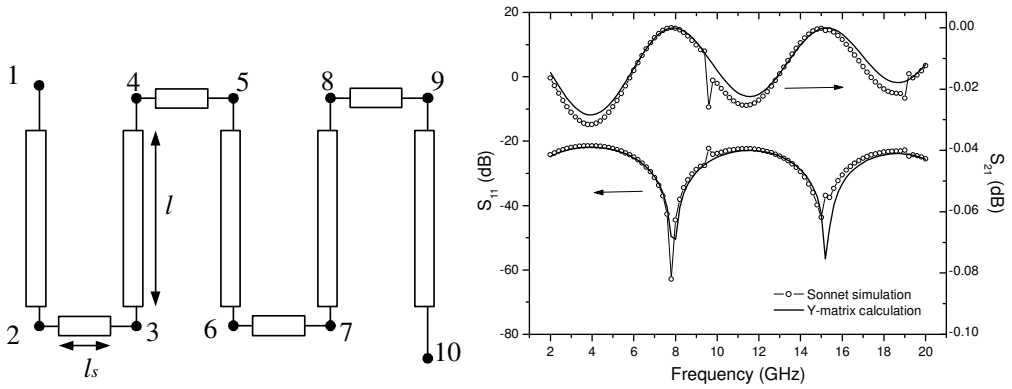

(a) (b)

Figure 5.20 (a) Nodal transmission line model for a 2-port/10-node meander; (b) Comparison of S parameters from Sonnet simulation and Y-matrix calculation. w=0.02mm, s=0.04mm, l=1mm, l_s=0.18mm.

Using the admittance-matrix method, one can study the effect of cross coupling on the dispersion, the input impedance and the stopband of a meander line, by varying the values of the odd- and even-mode parameters. Attempts were also made on modelling a meander line like Figure 5.11 with two juxtaposed branches. The cross coupling between the two branches is simply treated as if there is a directional coupler with its four ports terminated at node 1, n/2, (n+2)/2, and n. The admittance elements representing this are superposed on the matrix of an unwound meander line.

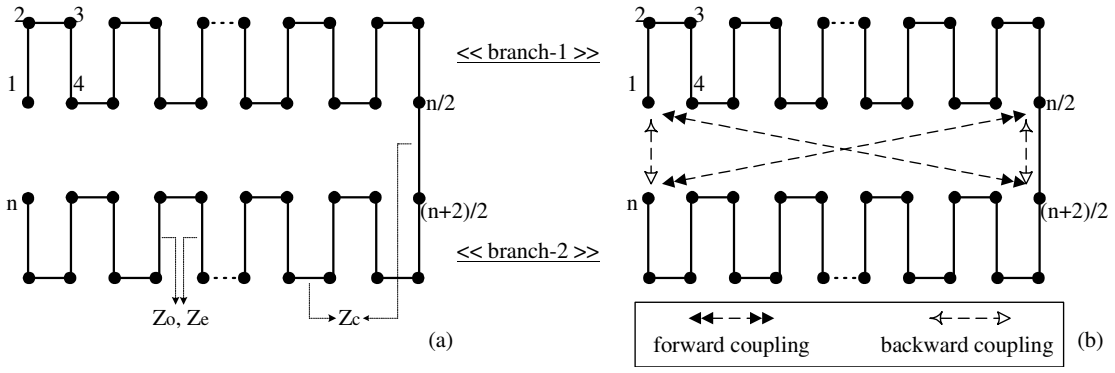

Figure 5.21 A meander line with juxtaposed branches represented by a 2-ports/*n*-node model. In case (a), there is no coupling between the two branches; In case (b), forward coupling exists between node 1 and (*n*+2)/2, and between *n*/2 and *n*, backward coupling exists between node 1 and *n*, and between *n*/2 and (*n*+2)/2.

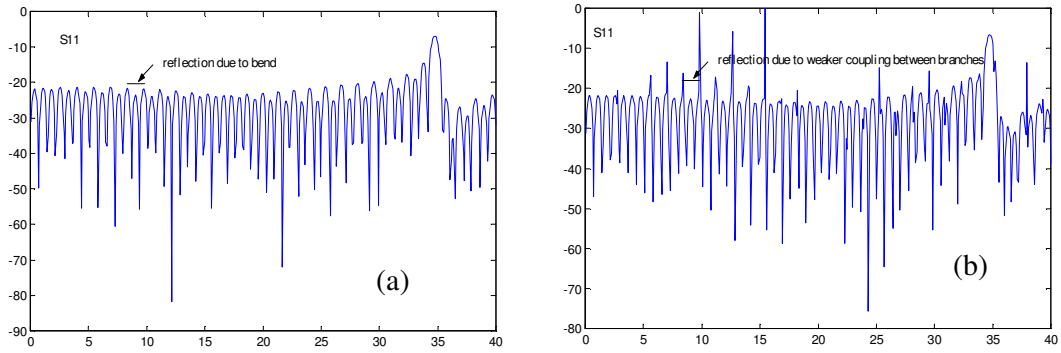

Figure 5.22 Calculated S_{11} for the 2-port/100-node meander lines as diagrammed in Figure 5.21(a,b) using Y-matrix method.

Figure 5.22 shows the calculation results of the 2-port/100-node meander lines corresponding to the two cases diagrammed in Figure 5.21. In the first case of Figure 5.21(a), it is assumed that there is no coupling between the juxtaposed branches. However, there is a discontinuity at the connecting line between node $n/2$ and $(n+2)/2$, because the characteristic impedance of this line is Z_c, mismatched with Z_e and Z_o of the section in the meander branch. As expected, this impedance discontinuity results in the ripples in Figure 5.22(a), twice the smallest interval caused by the port discontinuity. In the case of Figure 5.21(b), admittance elements are added in the matrix to represent a weak coupling between the two branches. This causes some reflection peaks in S_{11} of Figure 5.22(b). Although this can not adequately treat the complex electromagnetic coupling between the two meander branches, it does show that a weak coupling between them could cause some reflection peaks. This is a possible explanation of the responses in Figure 5.12. In both cases of Figure 5.21, a stopband at 34 GHz can be recognised.

[1] Sonnet simulation tools, Sonnet Software, Inc.
[2] Advanced Design System (ADS) simulation tools, Agilent Technologies.
[3] Agilent High Frequency Structure Simulator (HFSS) 5.5 simulation tools, Agilent Technologies.
[4] J. A. DeFalco, "Reflection and crosstalk in logic circuit interconnections", *IEEE Spectrum*, pp. 44-50, Jul. 1970.
[5] C. W. Davidson, *Transmission lines for communications*, 2nd ed., Macmillan Education, 1989.
[6]A. U. Bhobe, C. L. Holloway, M. Piket-May, "Meander Delay Line Challenge Problem: A Comparison Using FDTD, FEM and MOM", in *2001IEEE International Engineering Management Conference*, pp. 13-17, Aug. 2001.
[7]N. Orhanovic, R. Raghuram, N. Matsui, "Characterization of microstrip meanders in PCB interconnects", in *2000 Electronic Components and Technology Conference*, pp. 508-512, 2000.
[8] R. B. Wu, F. L. Chao, "Laddering wave in serpentine delay line", *IEEE Trans. Components, Packaging, and Manufacturing Technology*, Part B: vol. 18, no. 4, pp. 644 -650, Nov. 1995
[9] R. B. Wu, F. L. Chao, "Flat spiral delay line design with minimum crosstalk penalty", *IEEE Trans. Components, Packaging, and Manufacturing Technology*, Part B: vol. 19, no. 2, pp. 397 -402, May 1996
[10] B. J. Rubin, B. Singh, "Study of meander line delay in circuit boards", *IEEE Trans. Microwave Theo. Tech.*, vol. 48, no. 9, pp. 1452 -1460, Sept. 2000.
[11] S. H. Talisa, M. A. Janocko, D. J. Meier, C. Moskowitz, R. L. Grassel, J. Talvacchio, P. LePage, D. C. Buck, R. S. Nye, S. J. Pieseski, G. R. Wagner, "High-temperature superconducting wide band delay lines", *IEEE Trans. Appl. Supercond.,* vol. 5, no. 2, pp. 2291-2294, 1995.
[12] H. T. Su, Y. Wang, F. Huang, M. J. Lancaster, "Wideband superconducting microstrip delay line", (accepted) *IEEE Trans. Microwave Theory Tech.*, 2004, to be published.
[13] J. A. Weiss, "Dispersion and field analysis of a microstrip meander-line slow-wave structure", *IEEE Trans. Microwave Theo. Tech.*, vol. 22, no. 12, pp. 1194-1201,1974.
[14] A. K. Agrawal, "Dispersion in *n* coupled microstrip meanders", *IEEE Trans. Microwave Theory Tech.*, vol. 28, no. 8, pp. 927-932, Aug. 1980.
[15] T. Sudo, J. Kudo, Y. Ko, K. Ito, "Experimental characterization and numerical modelling approach of meander delay lines", in *2002 IEEE Int. Symp. Electromagnetic Compatibility*, pp. 711-715, Sept. 2002.
[16] H. T. Su, private communication, EDT Group, Dept. of EECE, The University of Birmingham, 2004.
[17] A. Porch, M. J. Lancaster, R. G. Humphreys, "The coplanar resonator technique for determining the surface impedance of $YBa_2Cu_3O_{7-\delta}$ thin film", *IEEE Trans. Microw. Theo. Tech.*, vol. 43, no. 2, pp. 306-314, 1995.
[18] A. I. Grayzel, "The admittance matrix of coupled transmission lines", *IEEE Trans. microwave Theory Tech.*, pp. 902-904, Oct. 1974.
[19] Z. Q. Chen, "Fast computation of multiple parameters of multiconductor coupled microstrip lines", *IEEE Trans. Microwave Theo. Tech.*, vol. 43, no. 6, pp. 1393-1395, Jun. 1995.
[20] D. G. Swanson, "A novel method for modeling coupling between several microstrip lines in MIC's and MMIC's", *IEEE Trans. Microwave Theo. Tech.*, vol. 39, no. 6, pp. 917-923, Jun. 1991.

Chapter 6 Design of transitions and connections

This chapter considers the design of the transitions from narrow coplanar waveguide to three types of wider transmission lines in order to facilitate the connections with the coaxial connectors. The term "transition" here refers to a tapering section between a narrow coplanar waveguide to a wide transmission line such as microstrip, CPW or CBCPW. The term "connection" refers to the interconnection between an external coaxial connector and the wide end of the transition. The transition and connection then forms the feed-line, which is treated separately from the main circuit in the design phase.

To take full advantage of the low material loss of superconductors, efficient transitions and connections between planar superconducting circuits and external connectors are required. This is particularly critical for a wideband device. At low frequencies, e.g. 2 GHz, the attenuation of a HTS coplanar waveguide is only 0.037dB/m at 30K[*], so the loss due to the transition and connection can readily surpass the loss of several meters of delay lines. With increasing frequencies, the surface resistance of a superconductor increases in proportion to the square of the frequency. At the same time, the return loss from the feed-line areas may also increase due to mismatches in the proximity of the interconnection. These effects are even more important for a coplanar waveguide than for a microstrip because of the presence of parasitic propagation modes[1], such as the slot-line mode in the CPW and microstrip-mode in the CBCPW. In the literature, transitions have been investigated between coplanar waveguide and different planar transmission lines, such as microstrip[2,3,4], stripline[5], slotline[6], and coplanar stripline[7]. The connections of microstrip and coplanar waveguide with coaxial structures were modelled in [8]. Most of the work is in the application context of CPW monolithic microwave integrated circuit (MMIC).

Tapering transitions are required for the work reported in this thesis because the line width of the delay lines is only 0.040 mm, whereas the coaxial connector has much wider feeding conductor. For the K-connectors[9] used here, the inner conductor (coaxial pin) is 0.30 mm in diameter, sleeved with a stress-releasing sliding contact of 0.15 mm wide, to which the coplanar delay line is connected by silver-loaded epoxy. An enlarged view of the interfacial

[*] This attenuation is acquired using the resonator techniques in Chapter 8. The value is 0.054 dB/m at 60K and 0.097 dB/m at 77K.

configuration is shown in Figure 6.1. The design aim is to achieve efficient transition over the wideband from 2 to 18 GHz by using tapering structures to keep a 50Ω characteristic impedance. The narrow end of the transition should match the width of the delay line, which is 0.04 mm. But for all simulations in this chapter, a width of 0.02 mm rather than 0.04 mm is used, because a 0.02 mm wide delay line was specified at the initial design stage. When this width is relaxed to 0.04 mm, the reflections would be expected to be somewhat smaller than simulated. For the wide end of the transition, its dimension needs to be optimized so as to achieve a good electromagnetic match with the feeding coaxial connectors. This will be investigated in the following section before dealing with the design of the transitions.

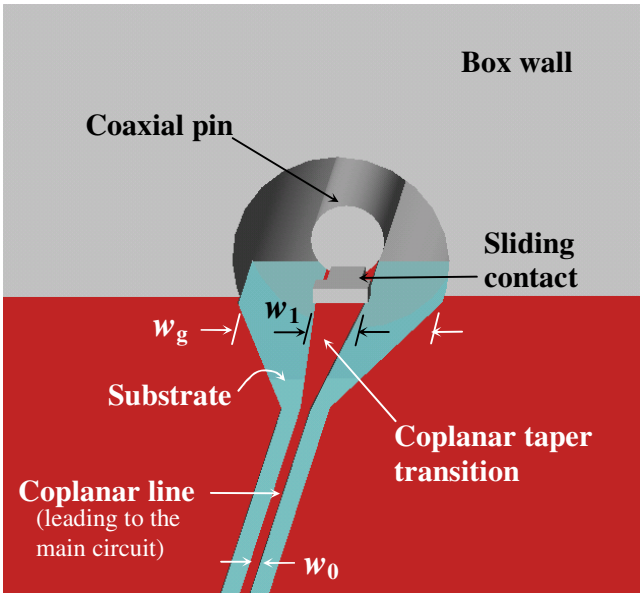

Figure 6.1 An enlarged view of the interface between a coplanar taper and the coaxial connector. Materials involved are normal metals (grey), HTS thin film (red), and $LaAlO_3$ substrate (navy).

6.1 Coplanar to Coaxial Matching

As illustrated in Figure 6.1 and Figure 6.2, to achieve a good match between the coplanar and the coaxial structure, the interconnections involved are not only between the coplanar signal line and coaxial pin, but also between the in-plane grounds and coaxial outer conductor, which is separated by w_g=0.8 mm in this configuration. In Figure 6.1, the sliding contact of the K-connector is represented by the small extrusion from the pin, and the widened tip is to simulate the possible overflow of the conducting epoxy, assumed to be 0.25 mm in the worst case.

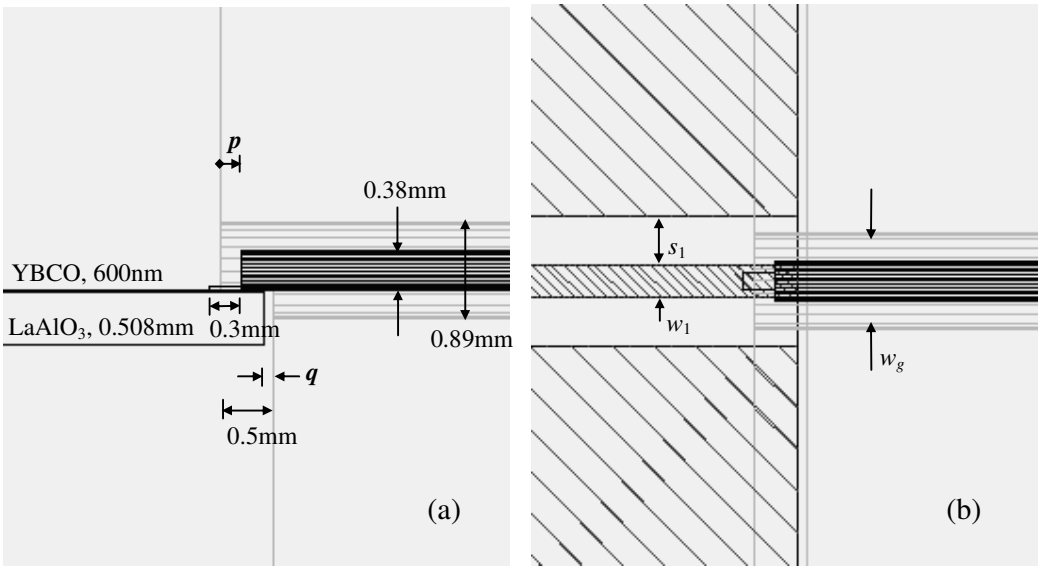

Figure 6.2 The side- and top-view of the matching configuration between the coplanar line and coaxial K-connector. The coaxial pin is 0.3 mm in diameter. The dimension of 0.38 mm takes the thickness of the sliding contact (0.04 mm) into account. The dimension of 0.5 mm is the width of the ledge around the feed-line area, which stretches 5 mm long centred at the signal line. The ledge beyond this is 1 mm wide.

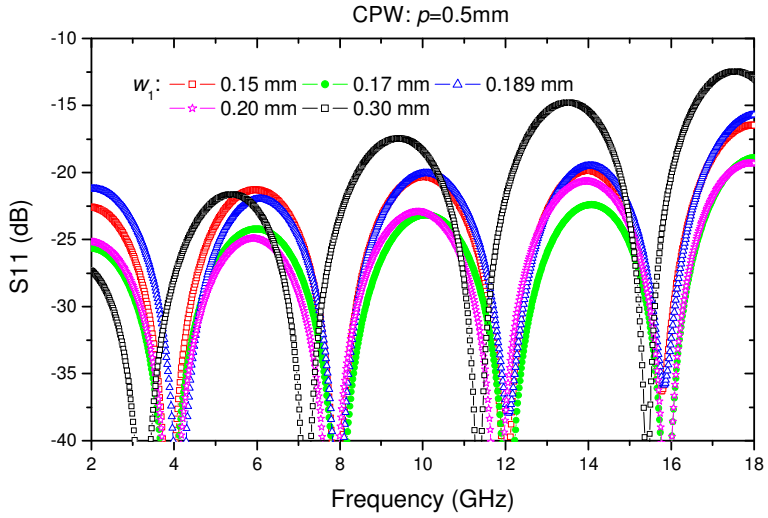

Figure 6.3 Simulated S_{11} responses of different matching configurations between the coplanar line and coaxial connector.

For the in-plane grounds of a 50Ω coplanar waveguide to match with the coaxial outer-conductor (ground), i.e. $w_g=w_1+2s_1$, the strip width w_1 needs to be 0.189 mm, slightly mismatching with either the coaxial pin or sliding contact. HFSS[10] simulations have been done to seek an optimal 50Ω configuration in the range of w_1 from 0.15 mm to 0.3 mm using the structure in Figure 6.2. The simulation results are shown in Figure 6.3. The best return loss is found for w_1=0.17 mm. However, this width is too narrow to be handled without the

conducting epoxy spreading onto the gaps between the central line and in-plane ground. So a slightly wider strip of 0.2 mm is finally adopted in this work, which defines the dimension of the wide end in the taper transitions. Simulation results in Figure 6.3 show that this does not compromise the return loss very much. The rest of the work aims to achieve 50 Ω transitions tapering from 0.2 mm to 0.02 mm for both the CPW and CBCPW lines.

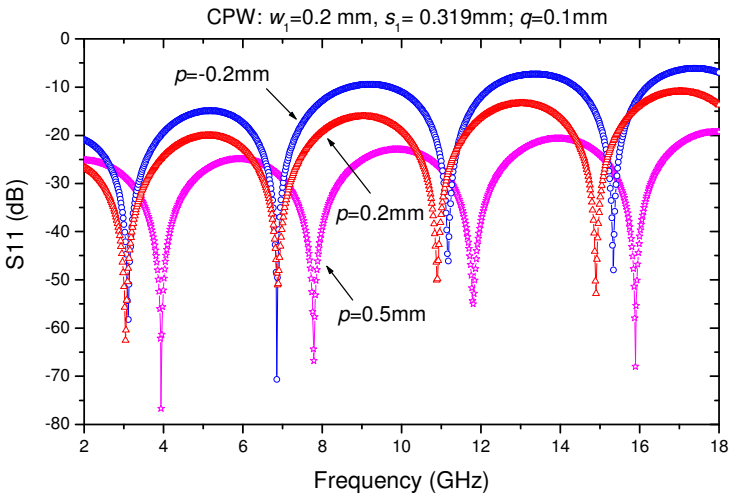

Figure 6.4 The variation of the return loss for difference extrusions *p* of the coaxial pin.

Simulations also identify two other factors affecting the return loss of the matching configuration: (1) the extrusion of the coaxial pin and (2) the clearance between the wafer and the box wall, which can be measured by the variables *p* and *q* in Figure 6.2(a). As shown in Figure 6.4, for a 0.2 mm wide 50Ω CPW line and an air clearance *q* of 0.1 mm, when *p* is 0.5 mm, a much lower return loss can be achieved than the other two cases. The shift of the transmission zeros (notches in S_{11}) indicates a change of reactance between *p*=0.5 mm and *p*=0.2, -0.2 mm. This is believed to be an inductive contribution due to the tab of the sliding contact bridging over the 0.1 mm air gap in the case of *p*=0.5 mm. As the discontinuity at the connecting point between the coplanar and coaxial is most likely to be capacitive because of the fringe fields, the inductive contribution would be favorable in terms of canceling the unwanted capacitance and improving the transmission efficiency. This compensation effect of an air gap was mentioned in [8]. In assembling the device, both dimensions (*p* and *q*) are difficult to control. The dimension *p* is kept as close to 0.5mm as possible by pushing the sliding contact into the coax until its tab is hardly seeable. The clearance *q* is kept minimal but still enough for the wafer to sit in the box. Normally, this requires a clearance of 0.1-0.2 mm.

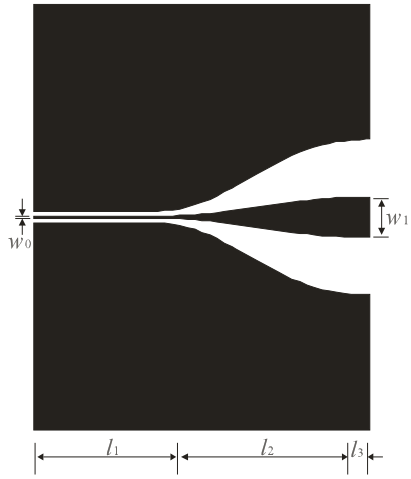

Figure 6.5 Layout of a coplanar line taper transition from w_1=0.2 mm to w_0=0.02 mm used in Sonnet simulations. l_1=0.8 mm, taper length l_2=1.2 mm and the pad length l_3=0.3mm.

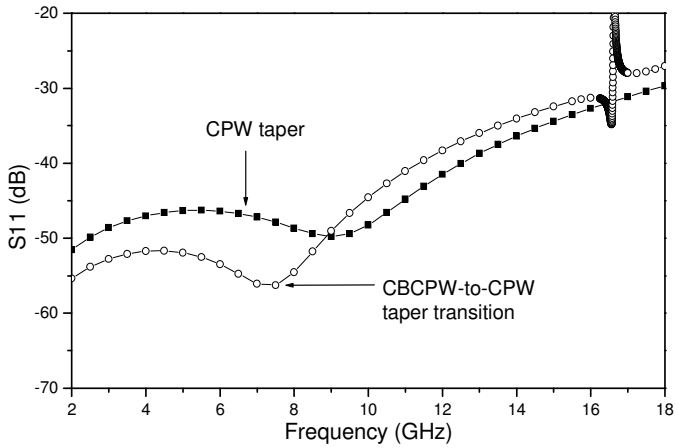

Figure 6.6 Simulated S_{11} responses of the CPW taper (shown in Figure 6.5) and the CBCPW-to-CPW taper transitions (shown later in Figure 6.13) using Sonnet.

6.2 CPW taper transition

For a conventional CPW, it is not difficult to form a constant-50 Ω taper by keeping appropriate strip-to-slot ratios. A smooth taper transition can be drawn according to the relation between the strip and slot for a 50Ω CPW, as given in Figure 4.3. The layout of such a taper is shown in Figure 6.5. The simulation result from Sonnet[11] is in Figure 6.6. The return loss is better than -25 dB from 2 to 18 GHz. A 3-dimentional packaged structure with the interface between the transition and a K-connector has also been examined using HFSS, as illustrated in Figure 6.7(a). (To reduce the computation effort, the taper in the simulation model is straight, not smoothed as in Figure 6.5.) The resultant return loss is better than –15 dB up to 14 GHz and -10 dB up to 18 GHz (Figure 6.8). It should be noted that any asymmetric configuration in this feeding structure could induce slot-line modes, so a good

alignment of the interconnection is needed.

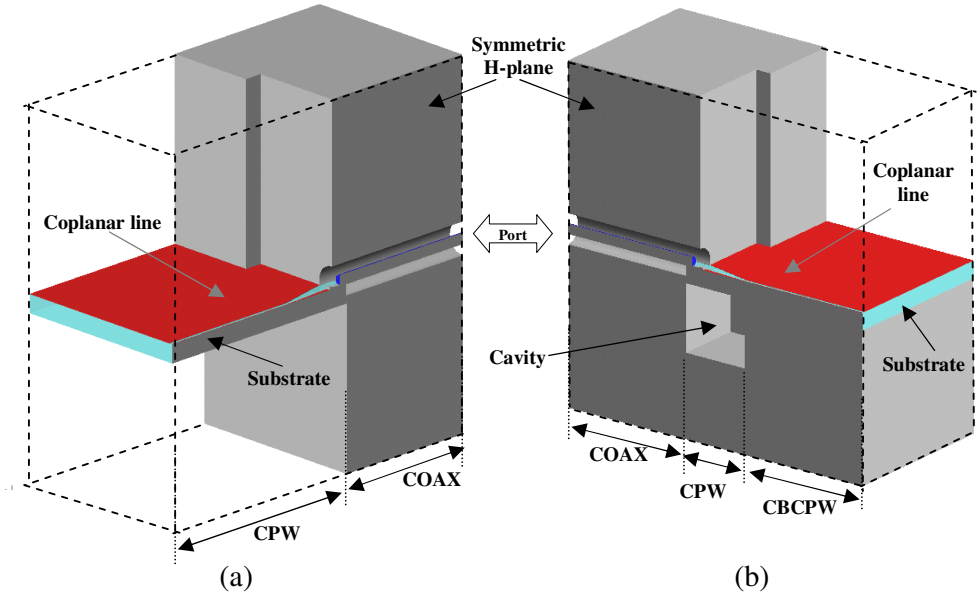

Figure 6.7 Configurations for (a) the CPW taper transition and (b) the CBCPW-to-CPW transition. Both are connected to the coaxial connectors. The actual HFSS model includes the coaxial input and output, and a 10 mm coplanar line in between. Only the input is shown. The symmetric magnetic plane (H-plane) is applied in simulation to save computation time. To further reduce the computation effort, the tapers in the models are straight, not smoothed as in Figure 6.5.

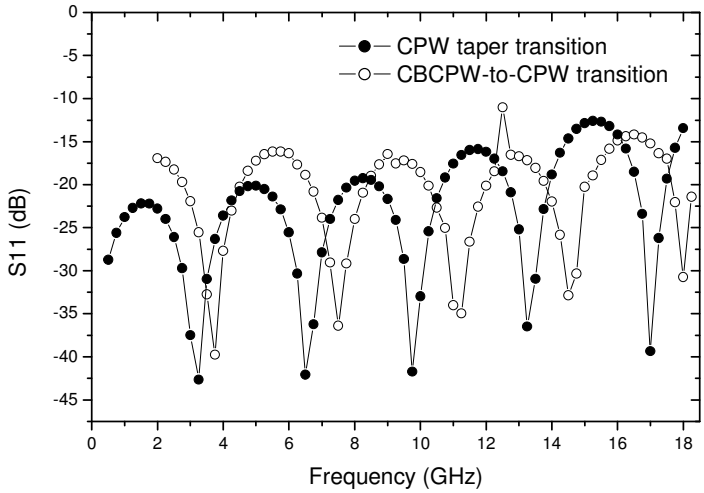

Figure 6.8 Simulated S_{11} responses of the CPW taper transition illustrated in Figure 6.7(a) and the CBCPW-to-CPW transition in Figure 6.7(b). The simulations are done by HFSS.

6.3 Transitions for CBCPW

For the CBCPW, a constant-50Ω tapering from 0.2 mm is difficult to achieve because of the parasitic microstrip-mode, which may become dominant when the slot (or strip) width of the

coplanar waveguide is comparable to the substrate thickness (0.508 mm in this case), as discussed in Section 4.2.4. According to the conformal-mapping calculations given in Figure 4.3, when the strip is wider than 0.17 mm, it is difficult to achieve 50Ω, however wide the slot is. This is because the transmission line effectively turns into a microstrip structure. To tackle the problem of this parasitic microstrip mode, two designs are considered: a CBCPW-to-microstrip transition (utilizing the coplanar-to-microstrip mode conversion) and a CBCPW-to-CPW transition (avoiding the mode conversion).

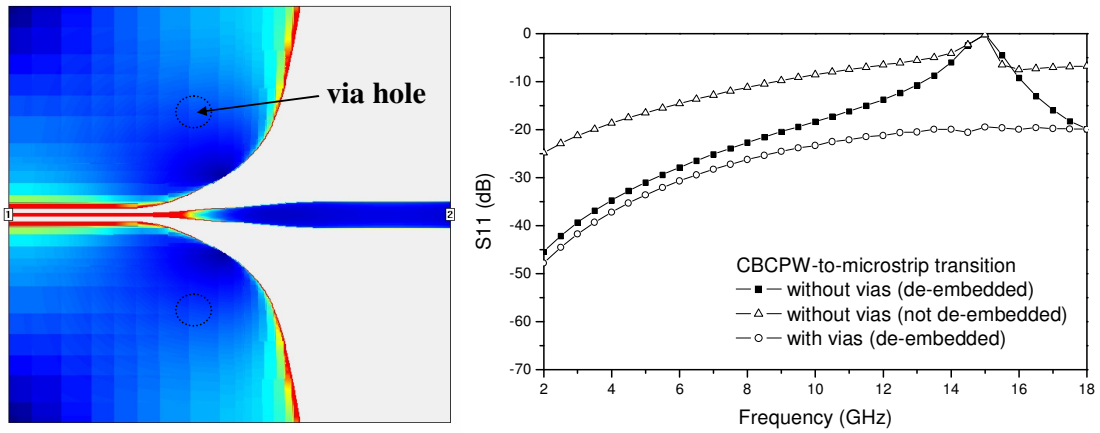

(a) (b)

Figure 6.9 (a) The simulated current density distribution at 15 GHz on the proposed CBCPW-to-microstrip transition without via holes. The positions of the possible vias are only marked. (b) Simulated S_{11} of the transitions with and without vias. A non-de-embedded response is also shown for the transition without vias.

6.3.1 CBCPW-to-microstrip transition

Taking advantage of the coplanar-to-microstrip mode conversion in a wide CBCPW, a CBCPW-to-microstrip transition structure can be constructed. Safwat *et al.*[2] demonstrated a step-like design of this kind. Here, the bandwidth of a smooth transition from CBCPW to microstrip is re-examined by Sonnet using the layout in Figure 6.9(a). It is found that this transition tends to block the signal at 15 GHz as shown in Figure 6.9(b). This may result from the discontinuous paths for the return currents of CBCPW and microstrip. Unlike microstrip, the return current of a CBCPW mainly flows along the edges of the upper ground planes (in-plane grounds) as illustrated in Figure 6.10(a). A transition from CBCPW to microstrip therefore requires vias to allow transfer of current from the in-plane grounds of CBCPW to the conductor backing of microstrip. The passband of the transition can be extended to cover 18 GHz with via holes put on the ground patches as shown in Figure 6.9.

However, this design is not adopted in the experimental device, considering the difficulties in making via holes on $LaAlO_3$ substrate.

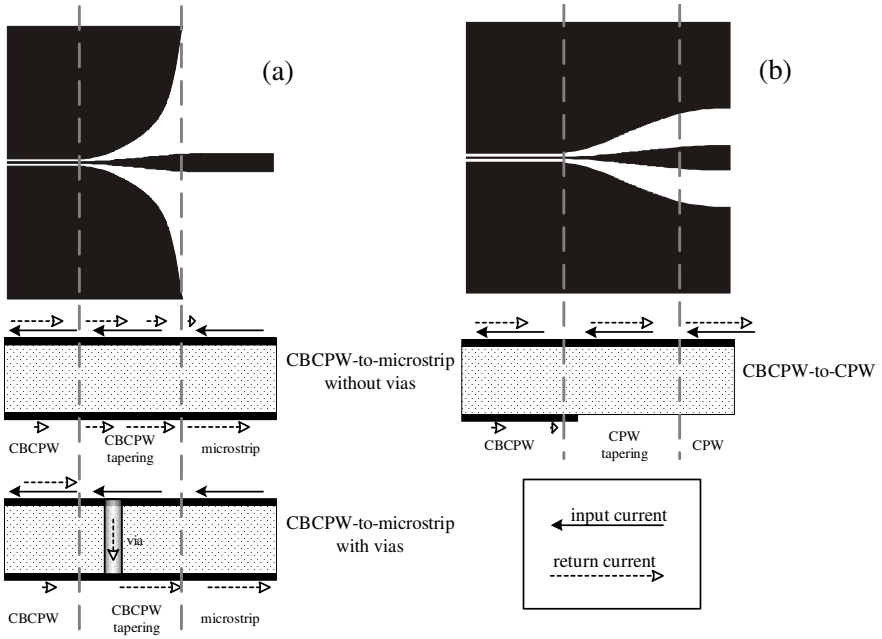

Figure 6.10 Paths of the return currents in the CBCPW-to-microstrip (without or with vias) and the CBCPW-to-CPW transition structures.

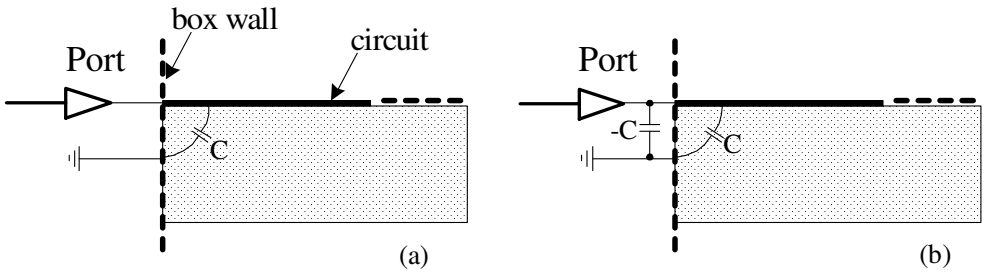

Figure 6.11 Effect of the box wall on Sonnet simulations: (a) without de-embedding and (b) with de-embedding.

As may be noticed, there is a big difference between the de-embedded and non-de-embedded S_{11} in Figure 6.9(b). This is because the effect of box-wall discontinuity is removed in a de-embedded simulation as illustrated in Figure 6.11. A shunt capacitance exists between the box wall and the transmission line attached to the port. The wider the line is, the larger the capacitance *C*. For a 0.3 mm wide line, *C* is 0.3pF. The de-embedding function of Sonnet removes this discontinuity by cascading a negative capacitance as shown in Figure 6.11(b). Practically, with a feeding connector bridging over, the air clearance between the box and substrate, as an inductive structure, may negate this capacitive discontinuity.

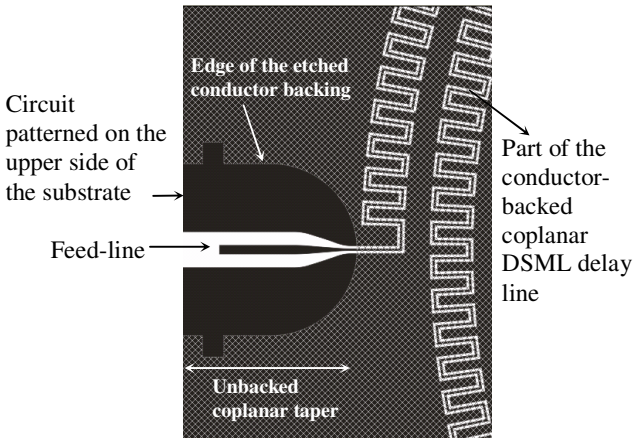

Figure 6.12 Layout of the feed-line area in the CBCPW delay line with the conductor-backing crosshatched, showing an unbacked coplanar taper transition to the conductor-backed coplanar DSML delay line.

6.3.2 CBCPW-to-CPW transition

To completely avoid the parasitic microstrip mode in the conductor-backed CBCPW taper, a CBCPW-to-CPW transition is proposed for the first time and implemented in the CBCPW delay line. The configuration of this transition is shown in Figure 6.7(b), which is also similar to the HFSS simulation model. The layout on the topside of the substrate is the same as for the CPW taper transition. On the reverse side, a small area of conductor backing beneath the tapering section is etched off as shown in Figure 6.12. A cavity is embedded into the box base so as to form an unbacked coplanar taper as in Figure 6.7(b). At the joint between this unbacked CPW taper and the CBCPW circuit, the slot is only 0.037 mm wide, much smaller than the substrate thickness. In this case, the presence of the conductor backing has little effect on the characteristic impedance and field distribution. The return current on the conductor backing is also small as illustrated in Figure 6.10(b). Therefore, the discontinuity is insignificant. This transition structure not only maintains a good electromagnetic match but also avoids the microstrip-mode likely to be induced in a wide CBCPW. HFSS simulation results in Figure 6.8 show that the return loss is below -15 dB over the frequency range from 2 to 18 GHz. The spike at 12.5 GHz is a mode from the simulation box. It disappears if a radiation boundary condition is applied. Such a CBCPW-to-CPW transition excluding the coaxial section can be simulated by Sonnet using a multi-layered structure in Figure 6.13. The circuit layout is the same as Figure 6.5. A conductor backing is placed only beneath the section of narrow coplanar line. As shown in Figure 6.6,

this gives a return loss better than -25 dB except the spike at 16.6 GHz, which is related to the finite length of the simulation structure.

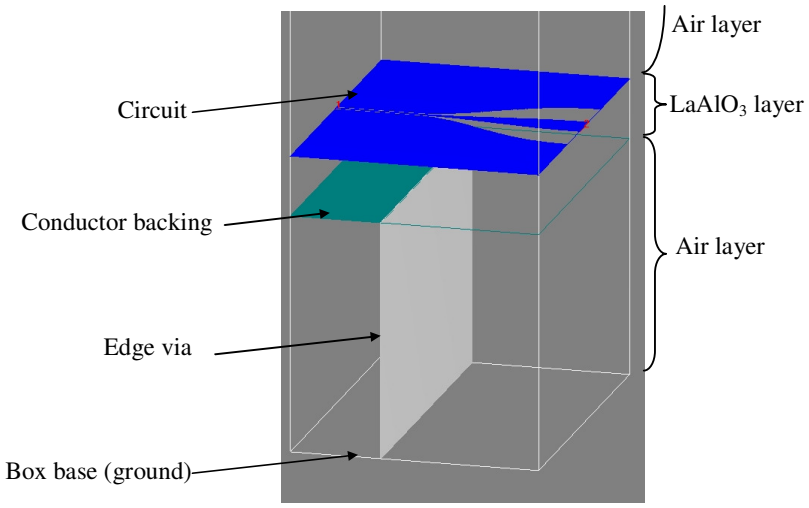

Figure 6.13 Multi-layered simulation model in Sonnet for a CBCPW-to-CPW taper transition.

[1] M. Riaziat, R. Majidi-Ahy, I. J. Feng, "Propagation Modes and Dispersion Characteristics of Coplanar Waveguides," *IEEE Trans. Microwave Theory Tech.*, vol. 38, pp. 245-251, Mar. 1990.
[2] A. M. E. Safwata, K. A. Zaki, W. Johnson, C. H. Lee, "Novel design for coplanar waveguide to microstrip transition", in *2001 IEEE MTT-S Int. Microwave Symp.*, vol. 2, pp. 607-610, 2001.
[3] G. P. Gauthier, L. P. Katehi, G. M. Rebeiz, "W-band finite ground coplanar waveguide (FGCPW) to microstrip line transition", in *1998 IEEE MTT-S Int. Microwave Symp*., pp. 107-109, 1998.
[4] J. P. Raskin, G. Gauthier, L. P. Katehi, G. M. Rebeiz, "Mode conversion at GCBCPW-to-microstrip-Line transitions", *IEEE Trans. Microwave Theory Tech*., vol. 48, no. 1, pp. 158-161, Jan. 2000.
[5] A. M. E. Safwata, K. A. Zaki, W. Johnson, C. H. Lee, "Novel transition between different configurations of planar transmission lines", *IEEE Microwave Wireless Components Letters*, vol. 12, no. 4, pp. 128-130, Apr. 2002.
[6] M. Houdart, C. Aury, "Various excitation of coplanar waveguide", in *1979 IEEE MTT-S Int. Microwave Symp*., pp. 116-118, Apr. 1979.
[7] R. N. Simons, *Coplanar Waveguide Circuits Components and System*, Wiley-IEEE Press, Apr. 2001.
[8] S. Cyrusian, G. Fotheringham, "Characterization of RF/microwave packaging structures", in *1995 SBMO/IEEE MTT-S International Microwave and Optoelectronics Conference*, pp. 335-339, 1995.
[9] K Connector is a registered trademark of Anritsu Company. 2002/2003 Edition of the Precision RF & Microwave Components Catalog.
[10] Agilent High Frequency Structure Simulator (HFSS) 5.5 simulation tools, Agilent Technologies.
[11] Sonnet simulation tools, Sonnet Software, Inc.